EVOLUTION OF PERTURBATIONS IN HIGH-SPEED WALL-BOUNDED FLOWS: FLOW-THERMODYNAMIC INTERACTIONS

A Dissertation

by

ANKITA MITTAL

Submitted to the Office of Graduate and Professional Studies of
Texas A&M University
in partial fulfillment of the requirements for the degree of

DOCTOR OF PHILOSOPHY

Chair of Committee,	Sharath S. Girimaji
Committee Members,	Diego Donzis
	Adonios Karpetis
	Jean-Luc Guermond
Head of Department,	Rodney Bowersox

May 2020

Major Subject: Aerospace Engineering

ABSTRACT

The emergence of flow-thermodynamic interactions and dilatational velocity field renders the evolution of perturbations in high Mach number flows significantly different from those in incompressible flows. These effects have been reasonably well investigated in the linear and fully turbulent regimes however, further research is required to understand the effect of kinetic-internal energy exchange on fundamental nonlinear process of spectral evolution. The primary motivation of this work is to investigate the evolution of perturbations in hypersonic wall bounded Poiseuille flow and establish the effect of compressibility. The work performed addresses three important aspects of computation and prediction of perturbation evolution in high-speed flows: (i) framework for internal energy dynamics, (ii) verification of computational methods based directly on gas kinetic theory and, (iii) physical mechanisms for nonlinear breakdown towards turbulence. Three studies, each addressing the above objectives, are performed which lead to valuable advances in our ability to simulate a wide range of hypersonic flows and improve our understanding of the physical phenomenon occurring in high speed flows. The findings are particularly valuable for the transition phenomenon in hypersonic boundary layers.

In the first study, critical mathematical framework to analyze and understand the nonlinear internal-kinetic energy interactions and subsequent spectral energy transfer is developed. The objective is to develop the framework and governing equations needed to analyze internal energy interactions and its spectral distribution in a manner similar to that of kinetic energy analysis. To emulate the role of velocity in kinetic energy analysis, a new variable ($\phi \sim \sqrt{p}$ where p is pressure) is introduced to enable the examination of internal energy dynamics. Evolution equations for the mean and fluctuating components of ϕ are derived. These equations enable precise examination of mean–turbulent flow internal energy interactions, internal–kinetic energy exchange and spectral distribution of internal energy.

The fundamental nature of flow instability changes with Mach number due to the underlying transformation in the nature of pressure. Therefore, a second study is performed with two-fold

objectives, (i) characterize the instability modes in high Mach number Poiseuille flows using linear stability analysis (LSA) and, (ii) perform direct numerical simulations (DNS) of the instability development using a gas-kinetic method (GKM) solver for the purpose of code validation by comparison against LSA results. The LSA and DNS are performed for the case of Poiseuille flow over a range of Mach numbers from moderately supersonic to hypersonic speeds. First, LSA is employed to establish the instability characteristics over the range of Mach numbers. It is exhibited the Mach number range can be divided into different regimes based on the dominant mode type such as first, second or higher modes. Two sets of GKM-DNS are performed to corroborate the LSA results over the Mach number range. In the first set of simulations, the background field in initially perturbed with the most unstable mode identified by LSA and the instability is allowed to evolve. It is shown that GKM-DNS accurately captures the changes in kinetic energy growth rate as a function of Mach number. The second set of GKM-DNS simulations is performed by superposing the background pressure field with random initial perturbations. After an initial transient period, the modes predicted by LSA dominate the DNS flow field evolution. The wave-vector and wall-normal profiles of all velocity components and pressure are well replicated by GKM-DNS at each Mach number. These insights in the linear regime and validation of GKM are important before analyzing the effect of compressibility on key nonlinear processes such as scale to scale cascade of energy.

In the final study we examine the perturbation growth and nonlinear breakdown to transition at various speeds. We characterize the nonlinear evolution of perturbations in high Mach number Poiseuille flow and contrast the behavior against equivalent incompressible flow. The focus is on the influence of pressure-dilatation on: (i) internal energy evolution; (ii) kinetic-internal energy exchange; and (iii) evolution of kinetic energy spectrum. We perform direct numerical simulations of plane Poiseuille flow at different Mach numbers subject to a variety of initial perturbations. In all high-speed cases considered, pressure dilatation leads to energy equipartition between wall-normal velocity fluctuations (dilatational kinetic energy) and pressure fluctuations (a measure of internal energy). However, the effect of pressure-dilatation on kinetic energy spectral growth can

be varied. In cases wherein pressure-dilatation is larger than turbulent kinetic energy production, spectral growth is considerably slow relative to an equivalent low Mach number case. When pressure-dilatation is smaller than production, the spectral growth is only marginally affected. As a consequence, in high-speed Poiseuille flow the spectral growth rate varies with wall-normal distance depending on the local pressure effects. These findings provide valuable insight into the nonlinear aspects of breakdown towards turbulence in high speed wall-bounded shear flows.

DEDICATION

To my mother, father and brother for their endless support throughout the course of this work.

ACKNOWLEDGMENTS

I would like to express my sincere gratitude towards my advisor, Dr. Sharath S. Girimaji for his continuous support and guidance throughout my Ph.D. He always patiently guided and motivated me throughout this research and writing of this thesis. I could not have imagined a better advisor and mentor for my doctoral research. I would also like to extend my gratitude towards my thesis committee members: Dr. Donzis Deigo, Dr. Adonios Karpetis and, Dr. Jean-Luc Guermond. Their encouragement and insightful comments have greatly improved this work.

I also thank my fellow lab-mates and friends at Texas A&M University: Divya, Rishita, Komal, Chetna, Akanksha, Sualeh, Pedram, Massey, Bajrang, Steven, Zach, Salar and Filipe for making the last six years fun. The endless discussions and sleepless nights of working together is greatly appreciated. A special thanks to Divya for always being there for me in these six years as a labmate, a best friend and also my roommate.

Last but not the least, I would like to thank my family: my parents - Hari Chand Mittal and Renu Mittal, my brother - Varun Mittal, sister-in-law - Suruchi Mittal and, my lovely nephew - Aarav Mittal, for the endless love and support as I worked towards my Ph.D. Your support has always kept me moving forward which helped me in achieving this milestone.

CONTRIBUTORS AND FUNDING SOURCES

Contributors

This work was supported by a dissertation committee chair, Prof. Sharath S. Girimaji and dissertation committee members consisting of Professors Diego Donzis and Adonios Karpetis of the Department of Aerospace Engineering and Professor Jean-Luc Guermond of the Department of Mathematics.

All work conducted for the dissertation was completed by the student independently.

Funding Sources

Graduate study was supported by the teaching assistantships and AERO Graduate Excellence Fellowship (FY2020) from Aerospace Engineering Department at Texas A&M University. Partial financial support was also provided by Air Force Office of Scientific Research (AFOSR) through the project "Nonlinear growth and breakdown toward turbulence in Hypersonic Boundary layers: Investigation of fundamental physical mechanisms," Grant No. FA9550-16-1-0360.

The numerical simulations performed in this research were conducted with the advanced computing resources provided by Texas A&M High Performance Research Computing and the Texas Advanced Computing Center at University of Texas at Austin.

TABLE OF CONTENTS

Page

LIST OF FIGURES

FIGURE Page

LIST OF TABLES

TABLE Page

1. INTRODUCTION

High speed laminar to turbulent boundary layer transition is vitally important in many aerospace engineering applications including space re-entry and hypersonic flight vehicles. The main challenge is the increased aerodynamic heating at high Mach numbers during the transition process (Haney Jr [1983]). Comprehensive understanding and accurate prediction of transition is critical for designing safe, reliable and cost effective hypersonic vehicles with enhanced payload capabilities (Bertin and Cummings [2003]). Assuming that the boundary layer is turbulent over the entire vehicle surface leads to excessive over design of the thermal protection system (TPS) causing increased vehicle weight and added expense to the mission costs (Hillberg [1967] and Berry and Horvath [2008]). Traditional (low speed) approaches such as e^N method, have also been used for estimating the laminar to turbulent transition for hypersonic boundary layers (Reed et al. [1997]). However, these methods do not account for the effect of compressibility leading to high degree of uncertainty in the predictions (Schneider [1999]).

Fundamental understanding of underlying nonlinear phenomena is essential for developing predictive tools for hypersonic transition (Stetson [1990]). Accurate computation of hypersonic flow can be challenging due to the presence of multiple instabilities, thin shock layers, low density, high-temperature effects and heat transfer (Anderson Jr [2006]). In boundary layer flows, the shock-boundary layer interactions further add to the complications (Cheng [1993]). Nonetheless, much progress has been made in recent years toward understanding, modeling and prediction of transition and turbulence processes in hypersonic boundary layers (Fedorov [2011]). However, two areas that require further efforts are: (i) understanding the nonlinear processes during breakdown toward turbulence and, (ii) development of numerical schemes and tools based on gas kinetic theory that are more appropriate for high-speed flows than Navier-Stokes equations. The work in this dissertation addresses these areas which are essential for simulating and understanding transition in high-speed boundary layer flows. The primary motivation is to investigate the nonlinear evolution of perturbations in hypersonic wall-bounded flow and establish the effect of compressibility.

1.1 Motivation and Background[1]

Compressibility profoundly affects each regime of perturbation development namely linear, nonlinear and fully developed turbulence. In incompressible or low speed flows, the evolution of kinetic energy is decoupled from internal energy due to a divergence free velocity field. On the contrary, the flow-thermodynamic interactions enabled by the dilatational field are significant at high Mach numbers. The pressure field performs work on the velocity field via the pressure-dilatation interaction leading to kinetic-internal energy exchange. Pressure-dilatation is, therefore, one of the key mechanisms for enforcing compressibility effects. Understanding the inter-scale energy interactions of kinetic and internal energies is extremely essential for study of turbulence onset in hypersonic flows.

Compressibility effects in the linear regime have been reasonably well investigated in literature. Compressible linear stability theory (LST) by Mack [1975], which identifies unstable modes using linear analysis of unsteady Navier-stokes equations, has been used extensively to investigate early stages of transition towards turbulence in compressible flows - Mack [1984], Reed et al. [1996] and Malik [1989]. Transition on flat plates is also studied using parabolized stability equations (PSE) developed by Bertolotti and Herbert [1991] and Herbert [1997] due to their ability to include nonparallel effects. The LST analysis exhibits multiple instability modes at high Mach numbers contrary to the incompressible LST which only exhibits one mode of instability. At moderately high Mach numbers the growth rate is dominated by the first mode, however, the second mode or the Mack mode dominates in the hypersonic regime. The second mode plays an important role in hypersonic transition process and its stabilization/destabilization is often studied as a means to understand and control transition - Fedorov [2011], Miró Miró and Pinna [2018], Bountin et al. [2018]. In Poiseuille flows, Butler and Farrell [1992] perform a modal analysis of linearized equations while a transient non-modal analysis is presented by Xie et al. [2017] highlighting the effect of compressibility in the linear regime. Compressibility effects on fully developed turbulence have

[1]Part of this section is reprinted with permission from "Nonlinear evolution of perturbations in high Mach number wall-bounded flow: Pressure-dilatation effects" by Ankita Mittal and Sharath S. Girimaji, 2020. Physics of Fluids, 32, 036101, Copyright [2020] by American Institute of Physics

also been studied in many works with the aim of modeling the fundamental mechanisms - Lele [1994], Sarkar [1995], Huang et al. [1995] and Gomez and Girimaji [2013, 2014].

While much effort has been expended on linear stability theories for compressible flows, a corresponding effort in understanding nonlinear effects is also required. Recent works have shown that nonlinear development of velocity perturbations is critically important for understanding and modeling breakdown toward turbulence in hypersonic boundary layers - Sivasubramanian and Fasel [2014, 2015] and Franko and Lele [2013]. The nonlinear spectral transfer of energy leading to the formation of a broad energy spectrum is a key aspect of breakdown toward turbulence. Various mechanisms of breakdown to turbulence of hypersonic boundary layers over flared cones have been investigated recently such as fundamental breakdown (Hader and Fasel [2019]) and transition with random inflow conditions (Hader and Fasel [2018]). Jahanbakhshi and Zaki [2019] recently evaluated nonlinearly most susceptible inflow disturbance leading to the earliest laminar to turbulence transition. They highlight the importance of nonlinear effects in accurate prediction of the transition location.

Despite recent progress, the effect of kinetic-internal energy exchange on the fundamental nonlinear processes of spectral evolution in wall-bounded flows is not well established. One key factor that renders nonlinear effects different in compressible flows is the emergence of dilatational field and internal energy fluctuations. The dilatational fluctuations are known to exhibit vastly different spectral transfer characteristics than solenoidal velocity field (Wang et al. [2013] and Praturi and Girimaji [2019]). Therefore, the goal of this work is to examine the nonlinear spectral evolution of perturbations in high-speed wall-bounded flows. The flow evolution is contrasted with equivalent low speed flow to establish the effect of change in the action of pressure.

As mentioned before, another area which requires additional effort is validation of computational tools based on gas kinetic theory for accurate computation of hypersonic transitioning flows. Numerical computational studies are essential in developing understanding of the underlying physics of complex problems such as developing an efficient predictive model for hypersonic flows. The presence of multiple instabilities and other flow phenomenon that make computation of

hypersonic flows challenging (Anderson Jr [2006]). At the current stage, most of the hypersonic flow computations are still being performed with compressible Navier-Stokes solvers with modifications to account for various high-speed and high-enthalpy effects. While such solvers are adequate, at hypersonic flow conditions, there are tremendous advantages to using numerical schemes based on the more fundamental Boltzmann equation. Employing the distribution function, instead of continuum variables provides a good basis for addressing non-equilibrium and non-continuum effects in future works (Venugopal et al. [2019]). Methods based on gas kinetic theory such as gas kinetic method (GKM) have been shown to be effective in all flow regimes, both low and high speed flows (Li et al. [2005], Xu and Mao [2006], May et al. [2007], Liao et al. [2009]), and efficiently captures shocks (Xu [2001]). The GKM solver has also been validated for compressible decaying and homogeneous shear turbulence flows Kumar et al. [2014, 2013] and mixing layers with Kelvin-Helmholtz instability Karimi and Girimaji [2017, 2016]. Despite these rigorous validations, these methods require further validation specifically for hypersonic wall-bounded transitioning flows.

1.2 Research Objectives

The dissertation consists of three studies each suited towards fulfilling the following objectives:

1. Develop a mathematical framework for analysis of internal energy dynamics and investigate the key energy interactions occurring in general compressible flows.

2. Validate gas-kinetic method (GKM) for transitioning hypersonic wall bounded flows using linear stability analysis.

3. Understand the effect of kinetic-internal energy interactions on nonlinear spectral growth in hypersonic boundary layers.

Toward the above objectives, three studies are undertaken and the specific tasks of each study are listed below.

1.2.1 Study 1: Mathematical framework for internal energy dynamics

This study develops the fundamental framework and governing equations needed to analyze kinetic-internal energy interactions and the spectral distribution of internal energy. In the nonlinear regime, the density fluctuations are large, therefore, density-weighted statistics must be used to describe the physics of energy exchange. A thermodynamic state variable, proportional to density-weighted speed of sound, is identified for internal energy. Similar to kinetic energy analysis, the total internal energy ($\overline{e}$) can now be partitioned into two parts corresponding to the content of mean field (e_m) and fluctuating field (e_t). The objective of this study is to characterize turbulent internal energy for a general compressible flow that enables study of spectral transport of turbulent internal energy. The specific tasks of this study include:

(i) Establish mean and fluctuating field components of total internal energy in terms of a positive definite quantity defined using the formulation of Miura and Kida [1995].

(ii) Derive governing equations for mean and turbulent field internal energies.

(iii) Identify energy interactions among all components of total kinetic ($\overline{K}$) and internal ($\overline{e}$) energies.

1.2.2 Study 2: Linear stability analysis and gas kinetic scheme (GKS) simulations of instabilities at high speeds

The flow-thermodynamic interactions lead to fundamentally different instabilities in high speed flows. Therefore, in this study we first characterize the dominant instabilities as a function of Mach number using linear stability analysis for benchmark wall-bounded flow. The study also serves as a validation of the GKM computational approach for high speed transitioning flows. We undertake the following tasks in this study:

(i) Perform an eigenvalue analysis of the linearized perturbation equations for Poiseuille flow and compute the most unstable modes along with its shape and growth rate.

(ii) Establish different Mach number regimes corresponding to various types of instability modes.

(iii) Perform single mode DNS using GKM for validation against LST.

(iv) Perform broadband random initial perturbation simulations for analysis of dominant modes.

The validation is performed using two sets of initial conditions, single mode and random inflow conditions. The single mode simulations validate the effectiveness of GKM to accurately retain the mode shape and growth rate of the initialized most unstable mode. On the other hand, the random inflow simulations provide validation of GKM by removing any bias of the most unstable mode from the initialized field.

1.2.3 Study 3: Simulations of compressibility effects on nonlinear spectral energy transfer

In this study, we characterize the effect of compressibility on nonlinear evolution of perturbations in high Mach number Poiseuille flow by contrasting the behavior against a corresponding incompressible flow. Specifically we seek to investigate the (i) effects of kinetic-internal energy exchange and, (ii) spectral transfer and spectral distribution of turbulent kinetic energy. The focus is on identifying modifications in the nonlinear processes due to change in the character of pressure from low to high Mach numbers. In incompressible transition, perturbation kinetic energy grows and cascades to smaller scales leading to 'de-correlation' of the flow field and turbulence. However, at high speeds, perturbation kinetic energy can be converted into internal energy. The canonical incompressible nonlinear spectral transfer is profoundly modified at hypersonic speeds. Therefore, we investigate the underlying physics behind the critical change in the character of nonlinear process through the following tasks:

(i) Perform numerical simulations of perturbation evolution (linear and early nonlinear stages) in Poiseuille flows for incompressible and compressible Mach numbers for several initial conditions.

(ii) Investigate the nature of internal-kinetic energy exchange during the nonlinear evolution of perturbations.

(iii) Examine the effect of compressibility (internal-kinetic energy exchange) on spectral energy transfer and energy distribution across the scales of motion.

1.3 Dissertation Outline

The following is the outline for this dissertation. Chapter 2 performs theoretical analysis of the full governing equations to develop a mathematical framework for internal energy dynamics. Mean and turbulent component of internal energy are identified along with various interactions among the internal and kinetic energy components. This work is published in Physical Review Fluids, 2019 (Mittal and Girimaji [2019]). Chapter 3 provides a complete ccharaterization of MAch number regimes based on linear instabilities and an in-depth validation of the promising gas kinetic method (GKM) against linear stability theory (LST) for high speed wall-bounded transition flows. Chapter 4 contrasts the nonlinear perturbation development of incompressible and compressible flows providing insight into the important mechanisms and parameters relevant for accurate modeling of hypersonic flows. This work is published in Physics of Fluids, 2020 (Mittal and Girimaji [2020]). The parameterization of nonlinear compressibility effects, based on the findings of the three studies, is further analyzed in Chapter 5. The important parameters identified can prove useful for developing future models for hypersonic flows. Finally the main conclusions from all the studies are summarized in Chapter 6.

2. MATHEMATICAL FRAMEWORK FOR INTERNAL ENERGY ANALYSIS[1]

Kinetic energy dynamics such as inter-scale transfer and spectral distribution are key features of turbulence and have been the subject of several investigations over many decades (Kolmogorov [1941]). In incompressible flows, wherein density is constant and uniform, the velocity (u_i) evolution equation, Navier-Stokes or the momentum conservation equation, forms the basis of kinetic energy analysis. For example, scale-to-scale energy transfer characteristics are dictated by the triadic interactions incumbent in the advective term of the spectral Navier-Stokes equation (Kraichnan [1964] and Yeung et al. [1995]). The kinetic energy spectrum is computed from Fourier-transforming the auto-covariance function of the velocity field (Pope [2000]).

The advent of compressibility renders the kinetic energy dynamics more complicated due to two factors: (i) spatio-temporal variations in density; and (ii) interactions with internal energy. Some of the complexities in kinetic energy dynamics due to density variations can be adequately addressed by considering density-weighted velocity field – ρu_i leading to Favre-averaging (Favre [1983]). But investigation of scale-to-scale transfer and spectral distribution require additional considerations. A new variable $\sqrt{\rho}u_i$, first proposed by Kida and Orszag [1992], has been utilized in many works for computing kinetic energy spectrum in compressible turbulence - Kida and Orszag [1992], Cook and Zhou [2002], Wang et al. [2013] and Grete et al. [2017].

The focus of this chapter is on the investigation of internal energy dynamics and its interaction with kinetic energy. It is desirable to investigate and characterize internal energy interactions in turbulence in a manner similar to that of kinetic energy analysis. Many studies perform insightful investigations of turbulent fluctuations of pressure - Sarkar et al. [1991], Vreman et al. [1996], Hamba [1999] and Ghosh et al. [2010]. However, such studies do not address internal energy spectral distribution or transfer in a manner similar to that of kinetic energy. For example, the scale-to-scale transfer of internal energy cannot be computed from the advection term in the spectral

[1]Reprinted with permission from "Mathematical framework for analysis of internal energy dynamics and spectral distribution in compressible turbulent flows" by Ankita Mittal and Sharath S. Girimaji, 2019. Physical Review Fluids, 4, 042601, Copyright [2019] by American Physical Society

pressure equation. Further, the turbulent internal energy spectrum is not the same as the turbulent pressure spectrum. To overcome these limitations, Miura and Kida [1995] propose a new internal energy variable ($\phi \sim \sqrt{p}$) corresponding to velocity for investigating the internal energy spectrum.

The objective is to extend the proposal of Miura and Kida [1995] and develop the mathematical framework and evolution equations required for performing a comprehensive and rigorous analysis of turbulent internal energy dynamics based on ϕ. Similar to kinetic energy analysis, we aim at partitioning the internal energy into two parts corresponding to contribution of the mean field and the fluctuating field. The equations based on ϕ will enable rigorous investigations of (i) internal–kinetic energy interactions at each scale; (ii) mean–turbulent internal energy exchange; and (iii) spectral distribution of internal and total energies in a turbulent flow field. The proposed framework is very important for a comprehensive understanding of total energy dynamics and spectral energy distribution in high-speed, compressible transition and turbulent flows.

The chapter is organized as follows. We begin with the full governing equations in §2.1. The kinetic energy analysis is presented in §2.2 and internal energy framework is developed in §2.3. The energy interactions among the various components of energy are discussed in §2.4 with final conclusions in §2.5.

2.1 Governing equations

The compressible Navier-Stokes equations for a calorically perfect ideal gas form the basis of this analysis:

$$\frac{\partial \rho}{\partial t} + \frac{\partial}{\partial x_j}(\rho u_j) = 0, \tag{2.1a}$$

$$\frac{\partial (\rho u_i)}{\partial t} + \frac{\partial (\rho u_i u_j)}{\partial x_j} = -\frac{\partial p}{\partial x_i} + \frac{\partial \tau_{ij}}{\partial x_j}, \tag{2.1b}$$

$$\frac{\partial}{\partial t}\left(\frac{p}{\gamma - 1}\right) + \frac{\partial}{\partial x_j}\left(\frac{p u_j}{\gamma - 1}\right) = \frac{\partial}{\partial x_j}\left(\kappa \frac{\partial T}{\partial x_j}\right) - p\frac{\partial u_k}{\partial x_k} + \tau_{ij}\frac{\partial u_i}{\partial x_j}, \tag{2.1c}$$

$$p = \rho R T, \tag{2.1d}$$

where ρ is the fluid density, u_i is velocity component, τ_{ij} is the viscous stress tensor, p is the gas pressure, γ is ratio of specific heats at constant pressure and volume, κ is the coefficient of thermal conductivity, T is the temperature, x_i is the spatial coordinate and t is time. The viscous stress tensor is given by:

$$\tau_{ij} = \mu\left(\frac{\partial u_i}{\partial x_j} + \frac{\partial u_j}{\partial x_i}\right) + \lambda\frac{\partial u_k}{\partial x_k}\delta_{ij}, \tag{2.2}$$

where μ is the coefficient of dynamic viscosity, λ is the coefficient of second viscosity and δ_{ij} is the Kronecker delta.

We will first present the kinetic (K), internal (e) and total (E) energy equations to identify the key interactions. The energy equations can be derived using eqs. (4.1b) and (4.1c):

$$\frac{\partial K}{\partial t} + \frac{\partial (K u_k)}{\partial x_k} + \frac{\partial}{\partial x_k}\Big[p u_k - \tau_{ik} u_i\Big] = p\frac{\partial u_k}{\partial x_k} - \tau_{ij}\frac{\partial u_i}{\partial x_j}, \tag{2.3a}$$

$$\frac{\partial e}{\partial t} + \frac{\partial (e u_k)}{\partial x_k} + \frac{\partial q_k}{\partial x_k} = -p\frac{\partial u_k}{\partial x_k} + \tau_{ij}\frac{\partial u_i}{\partial x_j}, \tag{2.3b}$$

$$\frac{\partial E}{\partial t} + \frac{\partial (E u_k)}{\partial x_k} + \frac{\partial}{\partial x_k}\Big[p u_k - \tau_{ik} u_i + q_k\Big] = 0, \tag{2.3c}$$

where,

$$K = \frac{1}{2}\rho u_i u_i, \quad e = \frac{p}{\gamma - 1}, \quad q_k = -\kappa\frac{\partial T}{\partial x_k} \quad \text{and} \quad E = K + e. \tag{2.4}$$

Equations (2.3a) and (2.3b) indicate interactions between kinetic and internal energy via pressure-dilatation and viscous action. Pressure-dilatation permits a two-way exchange while viscous action can only lead to a one-way transfer from kinetic to internal energy.

2.2 Kinetic energy analysis

The velocity field is decomposed into a Favre average and a corresponding fluctuation field (Favre [1983]):

$$u_i = \tilde{U}_i + u_i'', \tag{2.5}$$

while other variables (ψ) are decomposed using Reynolds averaging:

$$\psi = \overline{\psi} + \psi'. \tag{2.6}$$

For some interactions Reynolds averaging of the velocity field is also considered. Throughout the paper ($\tilde{\cdot}$) corresponds to Favre averaging and ($\bar{\cdot}$) to Reynolds averaging. The evolution of the mean kinetic ($\overline{K}$) and internal ($\overline{e}$) energies is given by,

$$\frac{\partial \overline{K}}{\partial t} + \frac{\partial (\tilde{U}_k \overline{K})}{\partial x_k} + \frac{\partial}{\partial x_k}\left[\overline{K u_k''} - \overline{\tau_{ik} u_i} + \overline{p u_k}\right] = \overline{p}\frac{\partial \overline{U}_k}{\partial x_k} + \overline{p' \frac{\partial u_k'}{\partial x_k}} - \overline{\tau_{ij}}\frac{\partial \overline{U}_i}{\partial x_j} - \overline{\tau_{ij}' \frac{\partial u_i'}{\partial x_j}}, \tag{2.7a}$$

$$\frac{\partial \overline{e}}{\partial t} + \frac{\partial (\tilde{U}_k \overline{e})}{\partial x_k} + \frac{\partial}{\partial x_k}\left[\overline{e u_k''} + \overline{q_k}\right] = -\overline{p}\frac{\partial \overline{U}_k}{\partial x_k} - \overline{p' \frac{\partial u_k'}{\partial x_k}} + \overline{\tau_{ij}}\frac{\partial \overline{U}_i}{\partial x_j} + \overline{\tau_{ij}' \frac{\partial u_i'}{\partial x_j}}. \tag{2.7b}$$

It is important to recognize that the mean kinetic energy of the flow has two contributions: the kinetic energy associated with the mean flow field and that associated with the fluctuations.

$$\overline{K} = K_m + k \quad \text{where,} \quad K_m = \frac{1}{2}\overline{\rho}\tilde{U}_i\tilde{U}_i \quad \text{and} \quad k = \frac{1}{2}\overline{\rho u_i'' u_i''}. \tag{2.8}$$

The mean field ($\tilde{U}_i$) kinetic energy is K_m and turbulent field (u_i'') kinetic energy is k in eq. (4.14).

Governing equation for K_m can be derived using the Favre averaged Navier-Stokes equation (Gatski and Bonnet [2013]):

$$\overline{\rho}\frac{\partial \tilde{U}_i}{\partial t} + \overline{\rho}\tilde{U}_j\frac{\partial \tilde{U}_i}{\partial x_j} + \frac{\partial \overline{\rho u_i'' u_j''}}{\partial x_j} = -\frac{\partial \overline{p}}{\partial x_i} + \frac{\partial \overline{\tau_{ij}}}{\partial x_j} \tag{2.9}$$

The equation for the mean-flow kinetic energy (K_m) can be obtained by multiplying eq. (2.9) with $\tilde{U}_i$:

$$\begin{aligned}\frac{\partial K_m}{\partial t} + \frac{\partial (K_m \tilde{U}_j)}{\partial x_j} + \frac{\partial}{\partial x_j}\left[\overline{\rho u_i'' u_j''}\tilde{U}_i + \overline{p}\,\overline{U}_j - \overline{\tau_{ij}}\,\overline{U}_i\right] &= \overline{\rho u_i'' u_j''}\frac{\partial \tilde{U}_i}{\partial x_j} + \overline{p}\frac{\partial \overline{U}_k}{\partial x_k} - \overline{\tau_{ij}}\frac{\partial \overline{U}_i}{\partial x_j} \\ &\quad + \overline{u_k''}\frac{\partial \overline{p}}{\partial x_k} - \overline{u_k''}\frac{\partial \overline{\tau_{kj}}}{\partial x_j}.\end{aligned} \tag{2.10}$$

Here we have used the relation $\overline{U}_k = \tilde{U}_k + \overline{u_k''}$ to simplify some terms. The evolution of turbulent kinetic energy (k) in compressible flows follows from (Huang et al. [1995] and Chassaing et al. [2002]):

$$\frac{\partial k}{\partial t} + \frac{\partial (k\tilde{U}_j)}{\partial x_j} + \frac{\partial}{\partial x_j}\left[\frac{1}{2}\overline{\rho u_i'' u_i'' u_j''} + \overline{p' u_j''} - \overline{\tau_{ij}' u_i''}\right] = -\overline{\rho u_i'' u_j''}\frac{\partial \tilde{U}_i}{\partial x_j} + \overline{p'\frac{\partial u_k''}{\partial x_k}} - \overline{\tau_{ij}'\frac{\partial u_i''}{\partial x_j}} - \overline{u_k''}\frac{\partial \overline{p}}{\partial x_k} + \overline{u_k''}\frac{\partial \overline{\tau_{kj}}}{\partial x_j}. \tag{2.11}$$

Utilizing $u_k'' = \overline{U}_k - \tilde{U}_k + u_k'$ and $\overline{\psi'} = 0$, we can establish that:

$$\overline{\psi'\frac{\partial u_k''}{\partial x_k}} = \overline{\psi'\frac{\partial u_k'}{\partial x_k}}. \tag{2.12}$$

Therefore, equation for turbulent kinetic energy (k) can be re-written as,

$$\frac{\partial k}{\partial t} + \frac{\partial (k\tilde{U}_j)}{\partial x_j} + \frac{\partial}{\partial x_j}\left[\frac{1}{2}\overline{\rho u_i'' u_i'' u_j''} + \overline{p' u_j'} - \overline{\tau_{ij}' u_i'}\right] = -\overline{\rho u_i'' u_j''}\frac{\partial \tilde{U}_i}{\partial x_j} + \overline{p'\frac{\partial u_k'}{\partial x_k}} - \overline{\tau_{ij}'\frac{\partial u_i'}{\partial x_j}} - \overline{u_k''}\frac{\partial \overline{p}}{\partial x_k} + \overline{u_k''}\frac{\partial \overline{\tau_{kj}}}{\partial x_j}. \tag{2.13}$$

The various terms in these equations and the incumbent physics will be discussed further below. In incompressible flows, the spectral transfer and distribution of kinetic energy across different scales of motion can be examined by performing Fourier transform of u_i'. As proposed by Kida and Orszag [1992], similar spectral energy analysis of compressible flows requires a new variable,

$$w_i = \sqrt{\rho} u_i'', \tag{2.14}$$

to account for spatio-temporal variations in density. The Fourier transform of the auto-correlation function of w_i yields the kinetic energy spectrum. The quartic interactions for turbulent kinetic energy cascade are also reduced to triadic interactions as:

$$\frac{\partial}{\partial x_j}\left[\frac{1}{2}\rho u_i'' u_i'' u_j''\right] = \frac{\partial}{\partial x_j}\left[\frac{1}{2} w_i w_i u_j''\right]. \tag{2.15}$$

2.3 Internal energy analysis

Unlike kinetic energy, it is more complicated to clearly identify the internal energy associated with the mean (or background field) and the turbulent internal energy. In the linear regime, when the density fluctuations are small, Sarkar et al. [1991] identified that the potential energy incumbent in pressure fluctuations can be approximated as $\overline{p'p'}/(2\gamma\overline{p})$. However, this representation is inadequate when the density fluctuations are large. Miura and Kida [1995] propose a more general approach which is valid for strongly compressible flows. They propose a new variable,

$$\phi \equiv \sqrt{e} = \sqrt{\frac{p}{\gamma - 1}}, \tag{2.16}$$

for examining the internal energy spectrum in simple isotropic flows. The justification is that ϕ^2 corresponds to internal energy.

In this study we develop the framework of equations based on ϕ to investigate flows with strong mean fields and more importantly to examine internal–kinetic energy interactions. First the choice of ϕ as the internal energy equivalent of velocity is further justified on the following physics-based argument. Using the relation $\gamma p = \rho a^2$, where a is the speed of sound, ϕ can be written as:

$$\phi = \frac{1}{\sqrt{\gamma(\gamma - 1)}}\sqrt{\rho}a. \tag{2.17}$$

Eq. (2.17) shows that ϕ includes density-weighted acoustic speed information which relates to the internal energy of the system. The state variable ϕ for internal energy is thus analogous to w_i for turbulent kinetic energy. ϕ can now be decomposed using Reynolds averaging:

$$\phi = \overline{\phi} + \phi' \text{ where, } \overline{\phi} = \overline{\sqrt{\frac{p}{\gamma - 1}}} \text{ and } \phi' = \sqrt{\frac{p}{\gamma - 1}} - \overline{\sqrt{\frac{p}{\gamma - 1}}}. \tag{2.18}$$

With this formulation, it is possible to clearly separate the mean internal energy of the flow into a

mean field and a fluctuating field contribution,

$$\overline{e} = \overline{\phi^2} = \overline{\phi}\,\overline{\phi} + \overline{\phi'\phi'} \quad \text{therefore,} \quad e_m = \overline{\phi}\,\overline{\phi} \quad \text{and} \quad e_t = \overline{\phi'\phi'}. \tag{2.19}$$

The strong similarity of internal energy decomposition in eq. (2.19) and kinetic energy partitioning in eq. (4.14) is clearly evident. The spectral transfer and spectral distribution of turbulent internal energy can be characterized from the behavior ϕ' much in the same manner as the turbulent kinetic energy transfer/distribution can be analyzed using $w_i = \sqrt{\rho}u_i''$. The Fourier transform of the auto-correlation of ϕ' yields the turbulent internal energy spectrum. Thus, $\phi' - w_i$ interactions hold the key to examining internal–kinetic energy exchange.

In the linear limit, as indicated by small turbulent Mach number - $M_t \equiv u'/a \ll 1$ (Sarkar et al. [1991]), the pressure fluctuations can be considered small relative to mean pressure. Therefore, higher order moments are negligible $\left(\frac{\overline{p'p'}}{\overline{p}^2} \approx 0,\ \frac{\overline{p'p'p'}}{\overline{p}^3} \approx 0,\ ...\right)$ and can be ignored. $\overline{\phi}$ and ϕ' can now be approximated as:

$$\overline{\phi} = \sqrt{\frac{\overline{p}}{\gamma-1}}\overline{\left[1+\frac{p'}{\overline{p}}\right]^{1/2}} \approx \sqrt{\frac{\overline{p}}{\gamma-1}} \quad \text{and} \quad \phi' \approx \frac{p'}{2\sqrt{\overline{p}(\gamma-1)}} + O\left(\frac{p'p'}{\overline{p}^{3/2}}\right). \tag{2.20}$$

Then the turbulent internal energy in the linear limit can be shown to be:

$$e_t = \overline{\phi'\phi'} \approx \frac{1}{4(\gamma-1)}\left[\frac{\overline{p'p'}}{\overline{p}}\right]. \tag{2.21}$$

The above expression is similar to the linear limit potential energy of pressure fluctuations as identified in literature (Sarkar et al. [1991] and Xie et al. [2017]).

2.3.1 Pressure field components

The mean and the fluctuation pressure field can be written in terms of the internal energy velocity variable ϕ as:

$$\overline{p} = (\gamma-1)\left[\overline{\phi}\,\overline{\phi} + \overline{\phi'\phi'}\right] \quad \text{and} \quad p' = (\gamma-1)\left[\phi'\phi' + 2\overline{\phi}\phi' - \overline{\phi'\phi'}\right]. \tag{2.22}$$

We can clearly see that mean and fluctuating pressure have a linear and nonlinear component:

$$\overline{p} = \overline{p}_m + \overline{p}_t \quad \text{and} \quad p' = p'_m + p'_t \tag{2.23}$$

where,

$$\begin{aligned} \overline{p}_m &= (\gamma - 1)\overline{\phi}\,\overline{\phi} \quad \text{and} \quad \overline{p}_t = (\gamma - 1)\overline{\phi'\phi'}, \\ p'_m &= 2(\gamma - 1)\overline{\phi}\phi' \quad \text{and} \quad p'_t = (\gamma - 1)\Big[\phi'\phi' - \overline{\phi'\phi'}\Big]. \end{aligned} \tag{2.24}$$

Here, $\overline{p}_m$ and $\overline{p}_t$ are the components of mean pressure associated with the mean field and the perturbation field respectively. Similarly, p'_m and p'_t are the components of fluctuating pressure associated with the mean field and the perturbation field. $\overline{p}_m$ and p'_m can also be understood as linear (or rapid) components while $\overline{p}_t$ and p'_t as nonlinear (or slow) components.

2.3.2 Internal energy framework

We can now derive the evolution equations for $e_m = \overline{\phi}\,\overline{\phi}$ and $e_t = \overline{\phi'\phi'}$. We start with the internal energy equation, eq. (2.3b) and use definitions $e = \phi^2$ and $p = (\gamma - 1)\phi^2$ to obtain an equation for ϕ:

$$\frac{\partial \phi}{\partial t} + u_k \frac{\partial \phi}{\partial x_k} = -\frac{\gamma}{2}\phi \frac{\partial u_k}{\partial x_k} + \frac{f}{2\phi} \quad \text{where,} \quad f = \left[-\frac{\partial q_k}{\partial x_k} + \tau_{ij}\frac{\partial u_i}{\partial x_j} \right]. \tag{2.25}$$

The Reynolds average of the thermal flux and viscous terms (f) can be written as:

$$\overline{f} = \left[-\frac{\partial \overline{q_k}}{\partial x_k} + \overline{\tau_{ij}}\frac{\partial \overline{U}_i}{\partial x_j} + \overline{\tau'_{ij}\frac{\partial u'_i}{\partial x_j}} \right]. \tag{2.26}$$

The last term in eq. (2.25) can be simplified as:

$$\frac{f}{2\phi} = \frac{f}{2\overline{\phi}} - \frac{f\phi'}{2\overline{\phi}\phi} \text{ which gives, } \overline{\left(\frac{f}{2\phi}\right)} = \frac{\overline{f}}{2\overline{\phi}} - \frac{1}{2\overline{\phi}}\overline{\left(\frac{f\phi'}{\phi}\right)}. \tag{2.27}$$

Reynolds-averaging eq. (2.25) gives an equation for $\overline{\phi}$ as:

$$\frac{\partial\overline{\phi}}{\partial t}+\tilde{U}_k\frac{\partial\overline{\phi}}{\partial x_k}+\overline{u_k''}\frac{\partial\overline{\phi}}{\partial x_k}+\overline{u_k''\frac{\partial\phi'}{\partial x_k}}=-\frac{\gamma}{2}\left[\overline{\phi}\frac{\partial\tilde{U}_k}{\partial x_k}+\overline{\phi}\frac{\partial\overline{u_k''}}{\partial x_k}+\overline{\phi'\frac{\partial u_k''}{\partial x_k}}\right]+\frac{\overline{f}}{2\overline{\phi}}-\frac{1}{2\overline{\phi}}\overline{\left(\frac{f\phi'}{\phi}\right)}. \quad (2.28)$$

Multiplying eq. (2.28) by $2\overline{\phi}$ yields the governing equation for the mean field contribution of mean internal energy (e_m). Using $\overline{U}_k=\tilde{U}_k+\overline{u_k''}$ and eq. (2.26), the simplified equation for e_m becomes:

$$\begin{aligned}\frac{\partial e_m}{\partial t}+\frac{\partial(e_m\tilde{U}_k)}{\partial x_k}+\frac{\partial}{\partial x_k}\left[\overline{\phi}\,\overline{\phi}\,\overline{u_k''}+2\overline{\phi}\,\overline{\phi'u_k''}+\overline{q_k}\right]=\ &\overline{\tau_{ij}}\frac{\partial\overline{U}_i}{\partial x_j}+\overline{\tau_{ij}'\frac{\partial u_i'}{\partial x_j}}\\ -(\gamma-1)\overline{\phi}\,\overline{\phi}\,\frac{\partial\overline{U}_k}{\partial x_k}+2\overline{u_k''\phi'}\frac{\partial\overline{\phi}}{\partial x_k}&+(2-\gamma)\overline{\phi}\overline{\phi'\frac{\partial u_k''}{\partial x_k}}-\overline{\left(\frac{f\phi'}{\phi}\right)}.\end{aligned} \quad (2.29)$$

The above equation is further simplified using the expression in eq. (2.12) and the definitions in eq. (2.24):

$$\begin{aligned}\frac{\partial e_m}{\partial t}+\frac{\partial(e_m\tilde{U}_k)}{\partial x_k}+\frac{\partial}{\partial x_k}\left[\overline{\phi}\,\overline{\phi}\,\overline{u_k''}+2\overline{\phi}\,\overline{\phi'u_k''}+\overline{q_k}\right]=\ &\overline{\tau_{ij}}\frac{\partial\overline{U}_i}{\partial x_j}+\overline{\tau_{ij}'\frac{\partial u_i'}{\partial x_j}}-\overline{p}_m\frac{\partial\overline{U}_k}{\partial x_k}\\ &+2\overline{u_k''\phi'}\frac{\partial\overline{\phi}}{\partial x_k}+\frac{(2-\gamma)}{2(\gamma-1)}\overline{p_m'\frac{\partial u_k'}{\partial x_k}}-\overline{\left(\frac{f\phi'}{\phi}\right)}.\end{aligned} \quad (2.30)$$

We can now determine the ϕ' equation by subtracting eq. (2.28) from eq. (2.25):

$$\begin{aligned}&\frac{\partial\phi'}{\partial t}+\tilde{U}_k\frac{\partial\phi'}{\partial x_k}+u_k''\frac{\partial\overline{\phi}}{\partial x_k}+u_k''\frac{\partial\phi'}{\partial x_k}-\overline{u_k''}\frac{\partial\overline{\phi}}{\partial x_k}-\overline{u_k''\frac{\partial\phi'}{\partial x_k}}\\ =-\frac{\gamma}{2}&\left[\phi'\frac{\partial\tilde{U}_k}{\partial x_k}+\overline{\phi}\frac{\partial u_k''}{\partial x_k}+\phi'\frac{\partial u_k''}{\partial x_k}-\overline{\phi}\frac{\partial\overline{u_k''}}{\partial x_k}-\overline{\phi'\frac{\partial u_k''}{\partial x_k}}\right]+\left(\frac{f}{2\phi}\right)'.\end{aligned} \quad (2.31)$$

To obtain the governing equation for turbulent internal energy (e_t) we multiply eq. (2.31) with $2\phi'$ and take average:

$$\frac{\partial e_t}{\partial t}+\tilde{U}_k\frac{\partial e_t}{\partial x_k}+2\overline{\phi'u_k''}\frac{\partial\overline{\phi}}{\partial x_k}+\overline{u_k''\frac{\partial\phi'\phi'}{\partial x_k}}=-\gamma\left[\overline{\phi'\phi'}\frac{\partial\tilde{U}_k}{\partial x_k}+\overline{\phi}\,\overline{\phi'\frac{\partial u_k''}{\partial x_k}}+\overline{\phi'\phi'\frac{\partial u_k''}{\partial x_k}}\right]+\overline{\left(\frac{f}{\phi}\right)'\phi'}. \quad (2.32)$$

The last term in eq. (2.32) can be simplified as:

$$\overline{\left(\frac{f}{\phi}\right)'\phi'} = \overline{\left[\overline{\left(\frac{f}{\phi}\right)}\,\phi' + \left(\frac{f}{\phi}\right)'\phi'\right]} = \overline{\left(\frac{f\phi'}{\phi}\right)}. \tag{2.33}$$

Simplifying eq. (2.32) and using the relation, $\tilde{U}_k = \overline{U}_k - \overline{u_k''}$ we get,

$$\begin{aligned}\frac{\partial e_t}{\partial t} + \frac{\partial (e_t \tilde{U}_k)}{\partial x_k} + \frac{\partial}{\partial x_k}[\overline{\phi'\phi' u_k''}] = &-(\gamma-1)\overline{\phi'\phi'}\frac{\partial \overline{U}_k}{\partial x_k} - (\gamma-1)\overline{(\phi'\phi' + 2\overline{\phi}\phi' - \overline{\phi'\phi'})\frac{\partial u_k''}{\partial x_k}} \\ &- 2\overline{u_k''\phi'}\frac{\partial \overline{\phi}}{\partial x_k} - (2-\gamma)\overline{\phi}\overline{\phi'\frac{\partial u_k''}{\partial x_k}} + \overline{\left(\frac{f\phi'}{\phi}\right)}.\end{aligned} \tag{2.34}$$

Now we can use the relations in eqs. (2.12), (2.22) and (2.24) to obtain the simplified form of the above equation:

$$\begin{aligned}\frac{\partial e_t}{\partial t} + \frac{\partial (e_t \tilde{U}_k)}{\partial x_k} + \frac{\partial}{\partial x_k}[\overline{\phi'\phi' u_k''}] = &-\overline{p}_t\frac{\partial \overline{U}_k}{\partial x_k} - \overline{p'\frac{\partial u_k'}{\partial x_k}} - 2\overline{u_k''\phi'}\frac{\partial \overline{\phi}}{\partial x_k} \\ &- \frac{(2-\gamma)}{2(\gamma-1)}\overline{p_m'\frac{\partial u_k'}{\partial x_k}} + \overline{\left(\frac{f\phi'}{\phi}\right)}.\end{aligned} \tag{2.35}$$

The triadic interactions of turbulent internal energy cascade can now be analyzed similar to turbulent kinetic energy via $\frac{\partial}{\partial x_k}(\phi'\phi' u_k'')$. The equations for $\overline{\phi}$, e_m, ϕ' and e_t in eqs. (2.28), (2.30), (2.31) and (2.35) constitute the framework required to describe internal energy interactions.

The mean total energy ($\overline{E} = K_m + k + e_m + e_t$) obtained through this framework can be written as:

$$\frac{\partial \overline{E}}{\partial t} + \frac{\partial}{\partial x_k}\left[\overline{E}\tilde{U}_k + \overline{\rho u_i'' u_k''}\tilde{U}_i + \frac{1}{2}\overline{\rho u_i'' u_i'' u_k''} + \overline{p u_k} - \overline{\tau_{ik} u_k} + \overline{q_k} + \frac{\overline{p u_k''}}{\gamma - 1}\right] = 0. \tag{2.36}$$

The mean total energy ($\overline{E}$) of a system changes only due to energy flux from the outside. Therefore, $\overline{E}$ for an isolated system remains constant. This is an important property of the chosen variables.

2.4 Energy interactions

We now discuss important aspects of kinetic–internal energy interactions and summarize the exchanges amongst $K_m,\ k,\ e_m$ and e_t (figure 2.1).

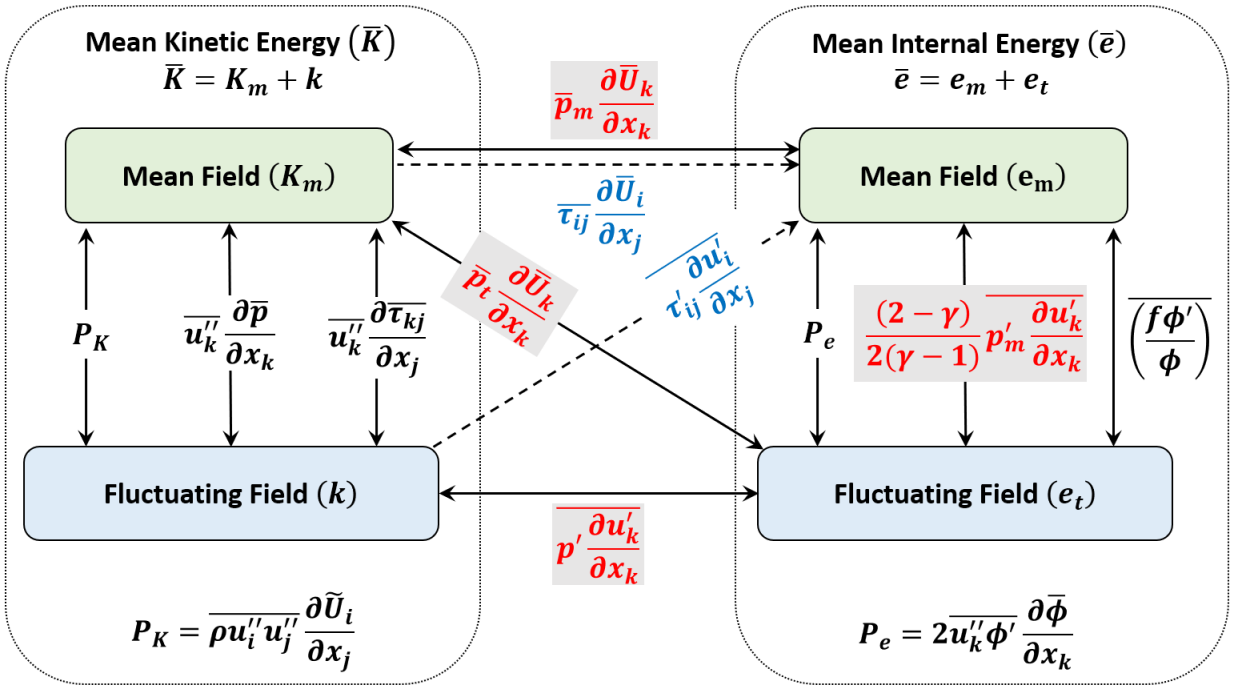

Figure 2.1: Interactions between kinetic and internal energies in the nonlinear regime using eqs. (2.10,2.13,2.30,2.35)

2.4.1 $(K_m - k)$ interactions

The most important interaction between mean–turbulent kinetic energy is production of turbulent kinetic energy (k) via $\overline{\rho u''_i u''_j} \frac{\partial \tilde{U}_i}{\partial x_j}$ as seen in eqs. (2.10) and (2.13). Production draws energy from the mean flow and deposits it into the fluctuating field. Other interactions appear as a consequence of compressibility and Favre-averaging. Both pressure work $(\overline{u''_k} \frac{\partial \bar{p}}{\partial x_k})$ and viscous action $(\overline{u''_k} \frac{\partial \overline{\tau_{kj}}}{\partial x_j})$ can lead to two-way exchange between the mean and fluctuating fields. For an incompressible flow, only production remains active among all $(K_m - k)$ interactions.

2.4.2 $(e_m - e_t)$ interactions

The terms $2\overline{u_k''\phi'}\frac{\partial\overline{\phi}}{\partial x_k}$, $\frac{(2-\gamma)}{2(\gamma-1)}\overline{p'_m\frac{\partial u'_k}{\partial x_k}}$ and $\overline{(\frac{f\phi'}{\phi})}$ in eqs. (2.30) and (2.35) lead to exchange between the mean field internal energy (e_m) and the turbulent internal energy (e_t). The first term is analogous to production in the kinetic energy equations. The second term causes exchange due to the linear or rapid component of fluctuating field pressure-dilatation mechanism while the last term is exchange due to viscous and thermal flux action.

2.4.3 $(K_m - e_m)$ interactions

The mean field kinetic–internal energy interact via the linear or rapid component of mean field pressure-dilatation ($\overline{p}_m\frac{\partial\overline{U}_k}{\partial x_k}$) and viscous action ($\overline{\tau_{ij}}\frac{\partial\overline{U}_i}{\partial x_j}$) as evident in eqs. (2.10) and (2.30). The pressure-dilatation action causes a two-way exchange and is represented with a double solid arrow in figure 2.1. On the other hand, viscous action dissipates mean field kinetic energy to mean field internal energy and is shown with a dashed one-way arrow. As mentioned by Huang et al. [1995], the Reynolds-averaged velocity field ($\overline{U}_i$) contributes towards the internal–kinetic exchange and not the Favre-averaged mean field ($\tilde{U}_i$).

2.4.4 $(K_m - e_t)$ interactions

The mean field kinetic energy and turbulent internal energy only interact via the nonlinear or slow component of mean field pressure-dilatation ($\overline{p}_t\frac{\partial\overline{U}_k}{\partial x_k}$). This exchange is identified using eqs. (2.10) and (2.35).

2.4.5 $(k - e_m)$ interactions

The turbulent kinetic energy dissipates energy into the mean field internal energy via the fluctuating field viscous action ($\overline{\tau'_{ij}\frac{\partial u'_i}{\partial x_j}}$) as seen from eqs. (2.13) and (2.30).

2.4.6 $(k - e_t)$ interactions

The exchange between turbulent kinetic and turbulent internal energy is caused via the fluctuating field pressure-dilatation mechanism ($\overline{p'\frac{\partial u'_k}{\partial x_k}}$) as evident in eqs. (2.13) and (2.35). This exchange includes contribution of both linear (or rapid) and nonlinear (or slow) pressure fluctuations. It is

also synchronous with $(e_m - e_t)$ exchange via the linear or rapid component of fluctuating field pressure-dilatation.

2.5 Conclusions

In this chapter, we have established a framework for examining internal energy of any fluid flow governed by the compressible Navier-Stokes equations. Analogous to fluid velocity, a suitable thermodynamic state variable for internal energy is identified ($\phi \sim \sqrt{p}$). It is shown that ϕ is proportional to density-weighted acoustic speed which relates to the internal energy of the system. Defining internal energy in terms of ϕ also allows partitioning of the mean internal energy of the flow into the mean field and perturbation field contributions, similar to mean kinetic energy. It is also established that spectral behavior of turbulent internal energy can be rigorously examined using ϕ'. Governing equations for e_m and e_t are derived to identify key internal–kinetic energy interactions. It is anticipated that this framework will be important for analysis and modeling of energy dynamics in high-speed compressible transition and turbulent flows.

3. LINEAR STABILITY ANALYSIS AND GAS KINETIC SCHEME (GKS) SIMULATIONS OF INSTABILITIES IN HIGH SPEED POISEUILLE FLOW[1]

Linear instabilities also referred to as primary instabilities play an important role in the laminar to turbulent transition process in boundary layers at different Mach numbers (Zhang et al. [2015], Zhu et al. [2018] and Zhu et al. [2020]). For a given flow configuration, the type and intensity of primary instabilities can change with Mach number due to the fundamental transformation in the nature of pressure. Mack [1975] performed an analysis of the type of dominant instabilities as a function of Mach number in boundary layer flows. At low Mach numbers, wherein pressure is governed by the Poisson equation, linear stability analysis or theory (LSA or LST) predicts a single so-called first mode instability. On the contrary, in high Mach number flows, wherein pressure is governed by state and energy equations, multiple instability modes can exist. It was observed that while first mode instability is most unstable in the supersonic regime, the second mode or Mack mode instability begins to dominate in the hypersonic regime for insulated plates. For cooled flat plate boundary layers, the shift from first mode to Mack mode instability can even occur at lower Mach numbers. It is therefore of inherent interest to examine the changes in linear stability as a function of Mach number. It is also important that the LSA results are verified with appropriate high-fidelity simulations.

Current computational methods almost exclusively use compressible Navier-Stokes solvers for performing high speed flow simulations. In many cases, the accuracy of the solution requires careful alignment of the grid with the bow shock (Sivasubramanian and Fasel [2014, 2015]) or wavenumber filtering to control numerical instabilities (Franko and Lele [2013]). Various modifications are required to account for high-speed and high-enthalpy effects. While such solvers have been shown to be adequate at hypersonic flow conditions, using numerical schemes based on the more fundamental Boltzmann equation can be more advantageous. Gas-kinetic simulations are

[1]Part of the data reported in this chapter is reprinted with permission from "Nonlinear evolution of perturbations in high Mach number wall-bounded flow: Pressure-dilatation effects" by Ankita Mittal and Sharath S. Girimaji, 2020. Physics of Fluids, 32, 036101, Copyright [2020] by American Institute of Physics

inherently better suited for simulating non-equilibrium and non-continuum effects as shown in the work by Venugopal et al. [2019].

A computationally viable gas-kinetics based scheme was developed by Xu (Xu [2001]) specifically for high speed flows to efficiently capture shocks. Since then the gas-kinetic method (GKM) has been shown to be effective in all flow regimes, both low and high speed flows (Li et al. [2005], Xu and Mao [2006], May et al. [2007] and Liao et al. [2009]). The GKM solver has also been validated for compressible decaying and homogeneous shear turbulence flows (Kumar et al. [2014, 2013]) and mixing layers with Kelvin-Helmholtz instability (Karimi and Girimaji [2017, 2016]). The GKM solver has already been validated in detail in past works of wall-bounded flows at low Mach numbers (Xie et al. [2017], Xie and Girimaji [2014]). At the present time direct numerical simulations based on gas kinetic method (GKM-DNS) is emerging as a viable tool for investigating some high-speed flow phenomena. As a next step in the development of GKM-DNS as a general computational tool, further validation studies are needed, especially in hypersonic transitioning flows. Accurate computation of unstable modes and growth rates is an essential first step towards establishing gas kinetic method (GKM) as a viable method for study of high-speed boundary layer transition.

The focus of this work is on establishing dominant Poiseuille flow instabilities as a function of Mach number using LSA and corroborating the findings using GKM-DNS. Thus the study also serves to validate the GKM computational approach. A wide range of incompressible laminar to turbulent transition studies have employed Poiseuille flow (Rempfer [2003]) to understand fundamental physical mechanisms. Thus, Poiseuille flow serves as a good canonical problem for the current validation study for hypersonic transitioning flows. Toward that end we undertake the following tasks:

(i) Perform an eigenvalue analysis of the linearized perturbation equations for Poiseuille flow and compute the most unstable modes along with its shape and growth rate.

(ii) Establish different Mach number regimes corresponding to various types of instability modes.

(iii) Perform single mode DNS using GKM for validation against LST.

(iv) Perform broadband random initial perturbation simulations for analysis of dominant modes.

The paper is organized as follows. A brief overview of compressible LST is presented in §3.1. Description of GKM numerical scheme used to perform DNS is in §3.2. The problem setup along with initial conditions used are described in §3.3. Linear analysis and GKM simulation results are presented in §3.4 along with a detailed discussion of the findings. The paper concludes with a concise summary of the important observations and inferences in §3.5.

3.1 Compressible linear stability analysis

The full set of compressible Navier-Stokes equations can be expressed as:

$$\frac{\partial \rho}{\partial t} + \frac{\partial}{\partial x_j}(\rho u_j) = 0, \tag{3.1a}$$

$$\frac{\partial (\rho u_i)}{\partial t} + \frac{\partial (\rho u_i u_j)}{\partial x_j} = -\frac{\partial p}{\partial x_i} + \frac{\partial \tau_{ij}}{\partial x_j}, \tag{3.1b}$$

$$\frac{\partial}{\partial t}\left(\frac{p}{\gamma - 1}\right) + \frac{\partial}{\partial x_j}\left(\frac{p u_j}{\gamma - 1}\right) = \frac{\partial}{\partial x_j}\left(\kappa \frac{\partial T}{\partial x_j}\right) - p\frac{\partial u_k}{\partial x_k} + \tau_{ij}\frac{\partial u_i}{\partial x_j}, \tag{3.1c}$$

$$p = \rho R T, \tag{3.1d}$$

where ρ is the fluid density, u_i is the velocity component, p is the gas pressure, τ_{ij} is the viscous stress tensor, γ is the specific heat ratio, κ is the coefficient of thermal conductivity, T is the temperature, x_i is the spatial coordinate and t is time. The viscous stress tensor is given by:

$$\tau_{ij} = \mu\left(\frac{\partial u_i}{\partial x_j} + \frac{\partial u_j}{\partial x_i}\right) - \frac{2}{3}\mu\frac{\partial u_k}{\partial x_k}\delta_{ij}, \tag{3.2}$$

where μ is the coefficient of dynamic viscosity and δ_{ij} is the Kronecker delta. The linear analysis follows the approach presented by Malik [1990] and Ramachandran et al. [2016]. The flow

variables are non-dimensionalized as follows,

$$\begin{gathered} x_i^* = \frac{x_i}{L},\ \ t^* = \frac{U_0}{L}t,\ \ \mu^* = \frac{\mu}{\mu_0},\ \ \kappa^* = \frac{\kappa}{\kappa_0} \\ u_i^* = \frac{u_i}{U_0},\ \ p^* = \frac{p}{p_0},\ \ T^* = \frac{T}{T_0},\ \ \rho^* = \frac{\rho}{\rho_0},\ \ f_b^* = \frac{L}{U_0^2} f_b, \end{gathered} \tag{3.3}$$

where L is the channel half width, μ_0 is the initial dynamic viscosity, κ_0 is the initial thermal conductivity, U_0 is the initial centerline velocity, p_0 is the initial uniform pressure, T_0 is the initial uniform temperature, ρ_0 is the initial uniform density and f_b is a constant body force applied to drive the flow. For the linear analysis, we express the flow variables as a sum of a background field and small perturbations,

$$A^* = \overline{A}^* + A^{*'}, \tag{3.4}$$

where A is the velocity components, density and temperature. A body force driven Poiseuille flow is considered to allow for a uniform background pressure field. The base flow for the stability analysis can be expressed as,

$$\overline{u_i^*} = (1 - y^{*2}, 0, 0),\ \ \overline{p^*} = 1,\ \ \overline{T^*} = 1,\ \ \overline{\rho^*} = 1,\ \ f_b^* = \frac{2}{Re}. \tag{3.5}$$

The base temperature and density are assumed to be uniform for the linear stability analysis as DNS simulations are initialized in a similar manner. Subject to these assumptions the coefficient of dynamic viscosity (μ) and thermal conductivity (κ) can also be considered constants for the analysis. Therefore,

$$\mu^* = 1 \quad \text{and} \quad \kappa^* = 1. \tag{3.6}$$

The linearized perturbation equations for this flow can now be expressed as,

$$\frac{\partial \rho^{*'}}{\partial t} + \frac{\partial u_j^{*'}}{\partial x_j} + (1 - y^{*2})\frac{\partial \rho^{*'}}{\partial x_1} = 0, \tag{3.7a}$$

$$\frac{\partial u_i^{*'}}{\partial t} + (1 - y^{*2})\frac{\partial u_i^{*'}}{\partial x_1} - 2y^* u_2^{*'}\delta_{i1} = -\frac{1}{\gamma M^2}\frac{\partial p^{*'}}{\partial x_i} + \frac{2}{Re}\rho^{*'}\delta_{i1} + \frac{1}{Re}\left[\frac{\partial^2 u_i^{*'}}{\partial x_j \partial x_j} + \frac{1}{3}\frac{\partial^2 u_j^{*'}}{\partial x_i \partial x_j}\right], \tag{3.7b}$$

$$\frac{\partial p^{*'}}{\partial t} + (1 - y^{*2})\frac{\partial p^{*'}}{\partial x_1} + \gamma\frac{\partial u_j^{*'}}{\partial x_j} = \frac{\gamma}{Re\,Pr}\frac{\partial^2 T^{*'}}{\partial x_j \partial x_j} - \frac{4\gamma(\gamma - 1)M^2 y^*}{Re}\left[\frac{\partial u_1^{*'}}{\partial x_2} + \frac{\partial u_2^{*'}}{\partial x_1}\right], \tag{3.7c}$$

$$p^{*'} = \rho^{*'} + T^{*'}, \tag{3.7d}$$

where $(.)^{*'}$ represents the fluctuations in the flow variables. The dimensionless parameters, Mach number (M), Reynolds number (Re) and Prandtl number (Pr) are defined as,

$$Re = \frac{\rho_0 U_0 L}{\mu_0}, \quad Pr = \frac{\mu_0 c_p}{\kappa_0}, \quad M = \frac{U_0}{\sqrt{\gamma R T_0}}, \tag{3.8}$$

where c_p is the specific heat at constant pressure and R is the gas constant. Normal mode analysis is now performed by representing the flow variables as follows,

$$A^{*'} = A(y)e^{\iota(\alpha x + \beta z - \omega t)}, \tag{3.9}$$

where A represents velocity components, temperature, density or pressure. Isothermal temperature boundary condition is applied for temperature on both walls and no slip for the velocity components. The boundary condition for density is derived from the y-direction momentum equation. The system of equations is reduced to an eigenvalue problem,

$$B\Phi = \omega I \Phi, \tag{3.10}$$

where ω is the growth rate for each streamwise-spanwise wavenumber pair, (α, β) and $\Phi = [\hat{u}_1, \hat{u}_2, \hat{u}_3, \hat{\rho}, \hat{T}]^T$ is the mode shape. The general form of eigenvalue problem of the linearized

perturbation equations can be referred to from Ramachandran et al. [2016]. The above eigenvalue problem is solved using second order central finite difference numerical scheme with 800 uniformly distributed grid points in the wall-normal direction. The linear analysis code has been verified to reproduce the OS mode and its shape at low Mach numbers.

3.2 Gas kinetic method (GKM)

The direct numerical simulations (DNS) in this study are performed using a finite volume gas kinetic method (GKM) solver. The details of the method can be referred to from Xu [2001] however, a brief overview of the numerical method is provided here. Similar to other kinetic theory based solvers such as Lattice Boltzmann method (LBM), this approach solves the Boltzmann equation,

$$\frac{\partial f}{\partial t} + \vec{c} \cdot \nabla f + \vec{a} \cdot \nabla_c f = \left(\frac{\partial f}{\partial t} \right)_{collisions}, \tag{3.11}$$

describing the evolution of single particle probability density function, $f(\vec{x}, \vec{c}, t)$ defined as a function of physical space, velocity space and time [Xu, 2001]. Here, $\vec{a}$ is the particle acceleration. Employing the distribution function instead of continuum variables allows applicability over a wider range of flow conditions and forms a good basis for addressing non-equilibrium and non-continuum effects. In this work, the BGK (Bhatnagar-Gross-Krook) collision operator is used to simplify the collision term given by,

$$\left(\frac{\partial f}{\partial t} \right)_{collisions} = \frac{g - f}{\tau}, \tag{3.12}$$

where, g is the equilibrium (i.e. Maxwellian) particle distribution function and τ is the characteristic relaxation time.

The macroscopic variables, $U = [\rho, \rho u_i, E]^T$, are obtained from the distribution function, f, using,

$$U = \int_{-\infty}^{\infty} \psi f d\Xi. \tag{3.13}$$

Here ρ is fluid density, u_i is macroscopic velocity, E is the sum of kinetic and thermal energy

densities, $\psi = [1, c_i, \frac{1}{2}(c_i^2 + \xi^2)]^T$, ξ is an internal energy variable with N degrees of freedom and $d\Xi = dc_i d\xi$ is a volume element in phase space. GKM being a finite volume based solver is governed by,

$$\frac{\partial}{\partial t}\int_{\Omega} U dx + \oint_{A} \vec{F}.d\vec{A} = 0, \tag{3.14}$$

where Ω is the control volume, A is the surface of control volume and $\vec{F}$ is the flux. In a discretized domain the eq. 3.14 can be expressed as,

$$U(t + \Delta t) - U(t) = \frac{\Delta t}{\Delta x_i}\Bigg[F_i(x_{j+1/2}, t) - F_i(x_{j-1/2}, t)\Bigg], \tag{3.15}$$

where i represents the three dimensions and j represents the discretized cell location. The fluxes at the cell interfaces are calculated using,

$$F_i = [F_\rho, F_{\rho u_i}, F_E]^T = \int_{-\infty}^{\infty} c_i \psi f(x_i, c_i, t, \xi) d\Xi. \tag{3.16}$$

In the finite volume formulation, values of conserved variables are only known at the cell centers. Flux values at the cell interfaces are obtained using a weighted essentially non oscillatory (WENO) nonlinear interpolation scheme. This interpolation is especially suitable for problems with strong discontinuities such as shocks in highly compressible flows. In GKM explicit calculation of the probability density function at cell interface is not performed but the fluxes are directly calculated by integrating the Boltzmann equation in phase space.

3.3 Problem setup

In the current study, a benchmark problem of a body force driven Poiseuille flow is considered. The problem setup, shown in figure 3.1, is the same as utilized by Xie et al. [2017] and Mittal and Girimaji [2020]. The base flow considered is the same as utilized to perform the LST analysis in 3.1 and is given by,

$$U(y, t = 0) = U_0\left(1 - \frac{y^2}{L^2}\right), \tag{3.17}$$

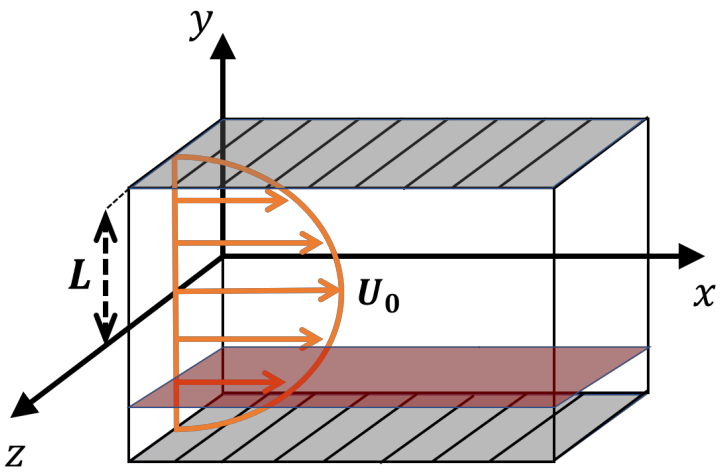

Figure 3.1: Problem Setup

where U_0 is the initial centerline velocity and L is the channel half width. Initial base density and temperature are assumed to be uniform throughout the channel similar to the LST analysis.

3.3.1 Boundary conditions

Periodic boundary conditions are applied in the streamwise (x) and spanwise (z) directions while no-slip and no-penetration conditions are enforced in the wall normal direction (y). The walls are isothermal with the enforced wall temperature same as the initial ambient temperature. Temporal simulations are performed and the evolution is considered in dimensionless shear time defined as:

$$St = x^* = \frac{U_0}{L}t. \tag{3.18}$$

Energy in different wavenumbers are computed on the different planes in the $y-$direction as shown in figure 3.1. Three planes namely near-wall ($y/L = -0.86$), intermediate ($y/L = -0.73$) and far-wall ($y/L = -0.5$) are considered in increasing order of distance from the wall.

3.3.2 Initial conditions

The flow is initialized with a set of small perturbations superposed on the base flow. Two types of initial perturbations are considered namely single mode and broadband random perturbations.

(i) In the single mode perturbations, each case is initialized with low turbulence intensity of the corresponding most unstable mode as computed using LST code. Turbulence intensity (I_0) is defined as,

$$I_0 = \frac{\sqrt{2k_0/\rho_0}}{U_0}, \tag{3.19}$$

where k_0 is the initial turbulent kinetic energy, ρ_0 is the initial density and U_0 is the initial centerline base flow velocity. Here, all flow variables such as density, temperature and velocity components are initialized. This initial condition enables a direct validation of GKM against LST. These are two-dimensional simulations performed at a grid size of $220 \times 490 \times 4$ for all Mach numbers.

(ii) For the broadband random initial perturbations, only the pressure field is randomly perturbed where pressure fluctuations are given by,

$$\frac{p'}{\overline{p}} = A(2r - 1) \qquad \text{with} \qquad A = 0.25. \tag{3.20}$$

Here, r is a random number uniformly distributed in $[-1, 1]$. No perturbations are added to other flow variables. This initial condition is inspired by the work of Hader and Fasel [2018] where random pressure perturbations are shown to simulate natural transition in a boundary layer. The broadband random initialization removes any bias in the initial conditions providing an efficient validation. These are three-dimensional simulations performed at a grid size of $200 \times 450 \times 200$ for all Mach numbers.

3.4 Results

We now present the LST analysis and GKM validation results. First a Mach number parameter sweep using the LST code is performed for a range of Mach numbers to characterize types of instabilities in different Mach number regimes. Appropriate Mach numbers are also identified for the further validation study. Low intensity single mode simulations are then performed using GKM and compared against LST results for validation. GKM is further validated using broadband

random inflow fluctuations .

3.4.1 Mach number parameter sweep using LST

LST has been used extensively to investigate early stages of transition towards turbulence in compressible flows. Mack [1984] showed that boundary layers at high Mach regime incur multiple higher order unstable modes as opposed to single first mode instability in the incompressible regime. Even though the first mode remains the most unstable mode in the supersonic regime, a shift to the second mode or Mack mode is observed as we reach the hypersonic regime. For cooled flat plate boundary layers, the shift from first mode to Mack mode can happen in the supersonic regime as well. Therefore, accurately identifying the correct instability at all Mach numbers is an important aspect of the numerical scheme utilized to study transition. A Mach number parameter sweep is performed using the LST analysis to identify relevant Mach numbers used for validation of GKM. Only integer wavenumbers are considered in the streamwise and spanwise directions for the LST analysis as the later DNS study imposes periodic boundary conditions which enforces integer wavenumber in these directions.

Mach numbers in the range $[2.5, 9.5]$ at 0.1 interval are considered and the most unstable mode and its growth rate are calculated. For all the Mach numbers considered, a two-dimensional mode is observed to be the most unstable. The variation of the streamwise wavenumber, growth rate and the type of mode with Mach number is shown in figure 3.2. Since only integer wavenumbers are allowed in the streamwise direction, the growth rate follows a bell curve for the range of Mach numbers with similar most unstable streamwise wavenumber shown as the red curve in figure 3.2. Initially the first mode is most unstable and the growth rate gradually increases with increase in Mach number and the streamwise wavenumber reduces. For a small range in $[5.8, 6.3]$, the Mack mode or the second mode dominates with the streamwise wavenumber of 4. Beyond Mach number of 8.8, higher order modes are most unstable with higher streamwise wavenumber. Five important Mach numbers, $M_c = 3.0,\ 4.5,\ 5.5,\ 6.0,\ 7.0$, are chosen for GKM validation to cover a range of growth rates and the shift of the most dominant mode from first to Mack mode.

Before proceeding to DNS simulations, we analyze the streamwise-spanwise wavenumber in-

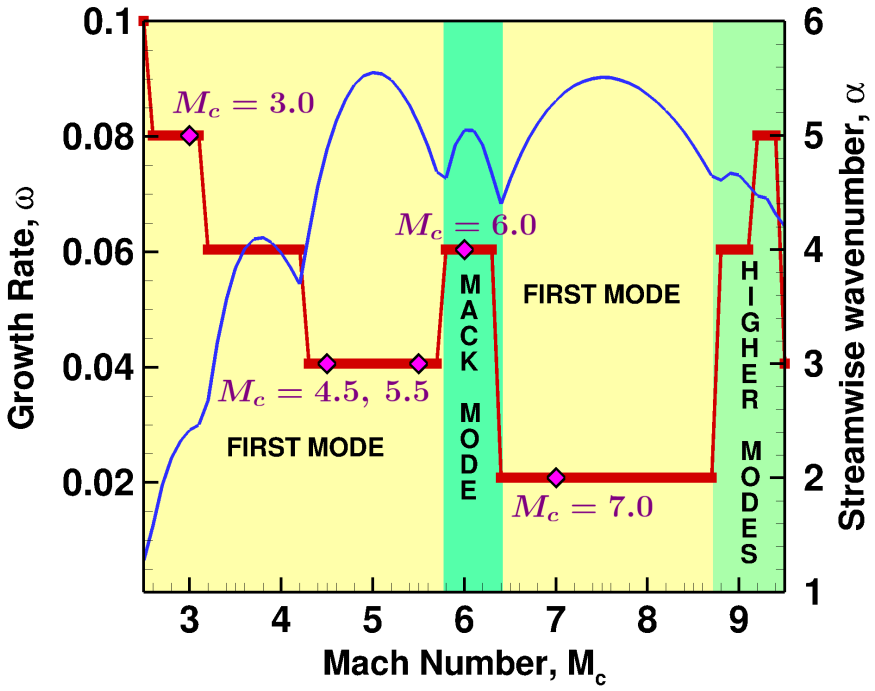

Figure 3.2: Mach number parameter sweep results from LST analysis.

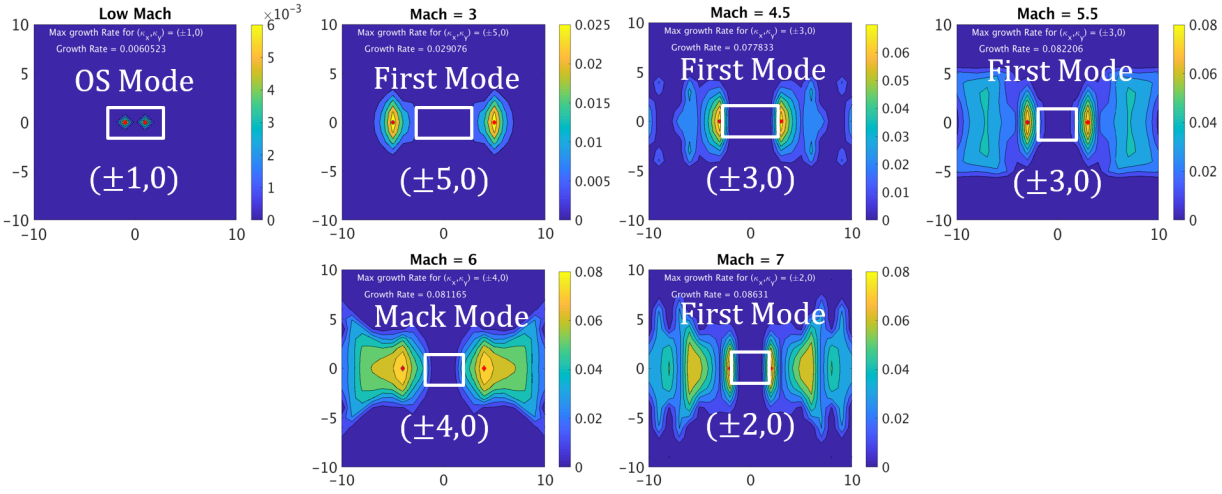

Figure 3.3: Streamwise-spanwise wavenumber instability contours at different Mach numbers.

Mach Number	$\boldsymbol{T}$ $\boldsymbol{(K)}$	$\boldsymbol{\rho_0}$ $\boldsymbol{(kg\ m^{-3})}$	$\boldsymbol{U_0}$ $\boldsymbol{(m\ s^{-1})}$
3.0	60	0.04	465.80
4.5	60	0.02667	698.70
5.5	60	0.02182	853.97
6.0	60	0.02	931.61
7.0	60	0.01717	1086.87

Table 3.1: Initial base flow conditions at different Mach numbers for GKM validation.

stability contours for low and high Mach numbers in figure 3.3. The contours are presented only for the Mach numbers selected for the later validation study. As the Mach number increases, the stability contours are observed to increasingly spread to higher wavenumbers. Although in all high Mach cases the lowest wavenumbers (highlighted within the white box) are seen to be stabilized irrespective of the most unstable mode type. On the contrary, the low Mach number flow is only unstable at the lowest wavenumbers with the OS mode instability. It can be concluded that as the Mach number increases, the lowest wavenumbers are stabilized due to the velocity-pressure interactions at high Mach numbers which are absent at low Mach number. This is consistent with the findings by Sarkar [1995], who shows that the suppression effect of compressibility is governed by the gradient Mach number, M_g, which is inversely proportional to the wavenumber. The lowest wavenumbers experience the highest M_g leading to high suppression due to compressibility for these waves. We now proceed to single mode perturbations for the above listed Mach numbers to validate GKM.

3.4.2 Single mode initial perturbations

Validation of GKM is performed by comparing the mode shapes and growth rates from LST analysis of the selected Mach numbers. DNS simulations are initialized with low intensity single mode perturbations of the corresponding most unstable modes ($I_0 = 0.007\%$). The base conditions for each Mach number considered are listed in table 3.1. The perturbations are initialized at low intensity to achieve a longer linear regime. This enables an effective comparison with LST results and directly validates GKM. For each Mach number the evolution of turbulent kinetic energy and

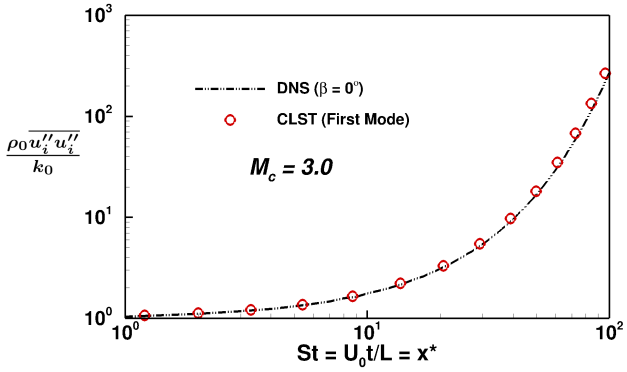

Figure 3.4: Energy growth comparison between LST and single mode GKM simulation at $M_c = 3$.

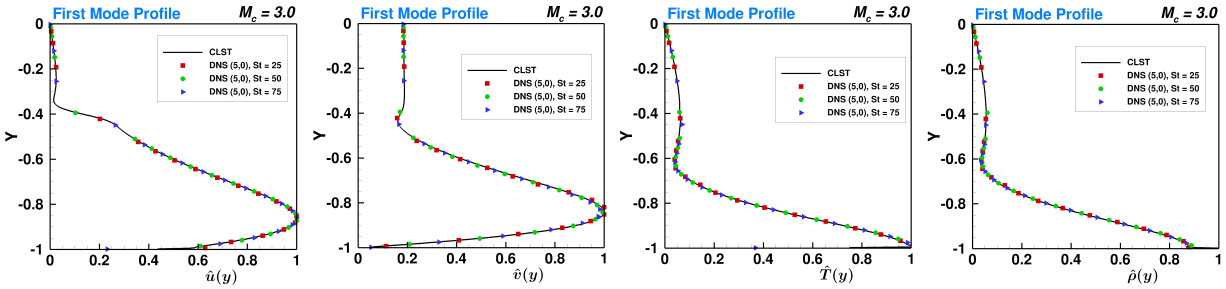

Figure 3.5: Mode shape comparison between single mode GKM simulation and LST at $M_c = 3$.

the mode shapes of all flow variables at different times are compared against LST.

In figure 3.4, the evolution of turbulent kinetic energy is compared for LST and GKM at $M_c = 3$. Excellent agreement for the perturbation energy evolution can be observed from the figure. Further, the initialized first mode shape at $M_c = 3$ is retained until $St = 75$ as evident in figure 3.5 where mode shape at shear times of 25, 50 and 75 are presented. Similar comparisons for evolution of turbulent kinetic energy at Mach numbers 4.5, 5.5, 6, and 7 are presented in figures 3.6, 3.8, 3.10 and 3.12 respectively. The corresponding mode shape comparisons are shown in figures 3.7, 3.9, 3.11 and 3.13. The mode shape through GKM is established using 18 wall-normal planes in the flow and by determining the turbulent kinetic energy amplitude of the most unstable wavenumber at each plane. The mode shapes of all cases considered show excellent agreement with the linear analysis predictions. For Mach numbers greater than 5.5, slight distortion of the mode shape at $St = 75$ can be observed. Also, the perturbation energy begins to depart the LST

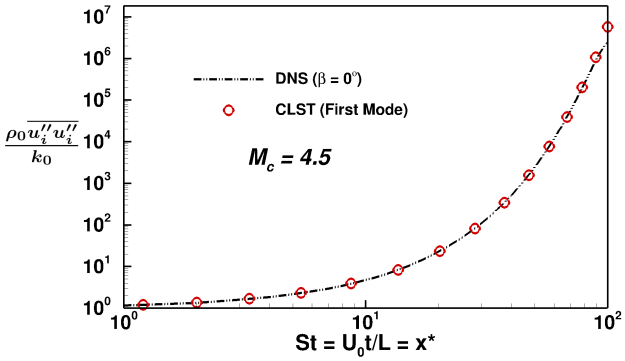

Figure 3.6: Energy growth comparison between LST and single mode GKM simulation at $M_c = 4.5$.

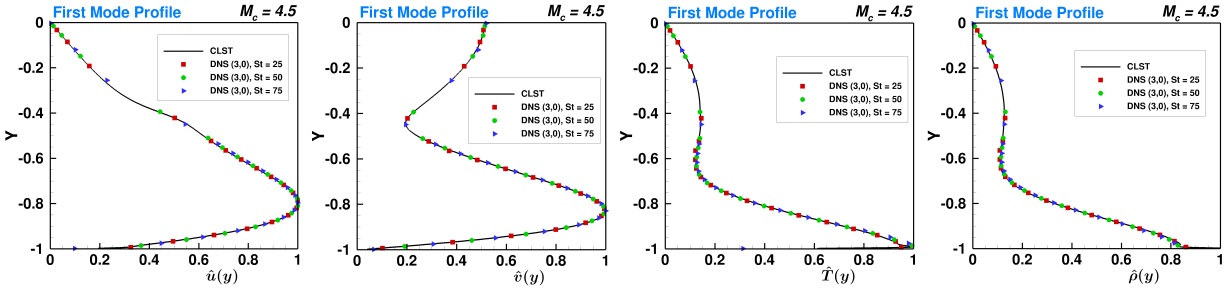

Figure 3.7: Mode shape comparison between single mode GKM simulation and LST at $M_c = 4.5$.

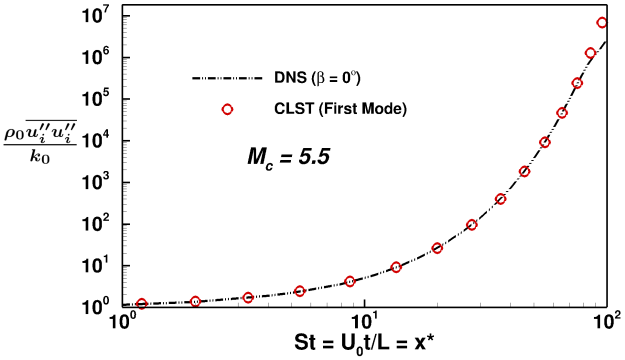

Figure 3.8: Energy growth comparison between LST and single mode GKM simulation at $M_c = 5.5$.

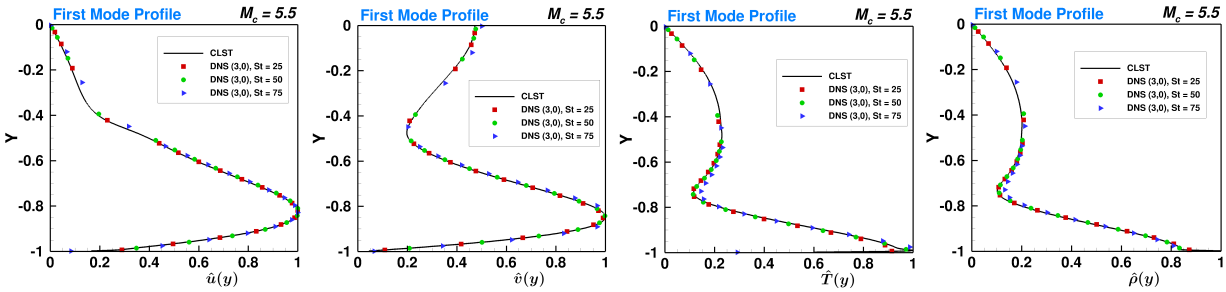

Figure 3.9: Mode shape comparison between single mode GKM simulation and LST at $M_c = 5.5$.

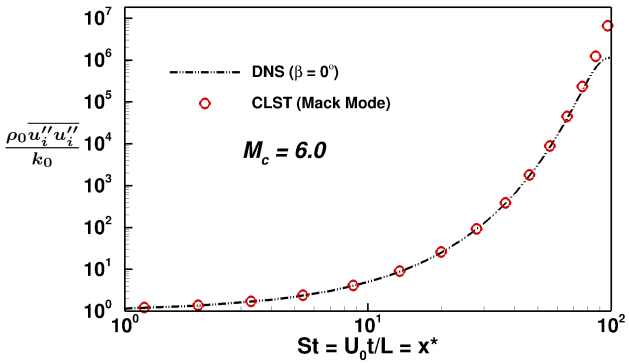

Figure 3.10: Energy growth comparison between LST and single mode GKM simulation at $M_c = 6$.

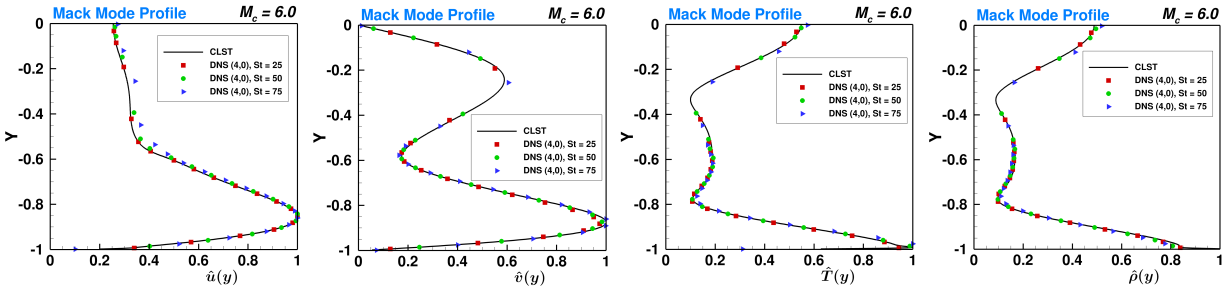

Figure 3.11: Mode shape comparison between single mode GKM simulation and LST at $M_c = 6$.

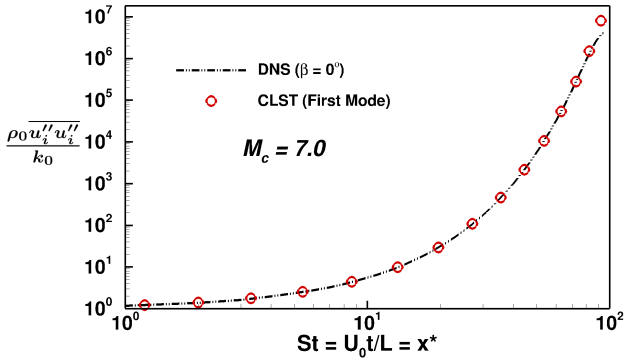

Figure 3.12: Energy growth comparison between LST and single mode GKM simulation at $M_c = 7$.

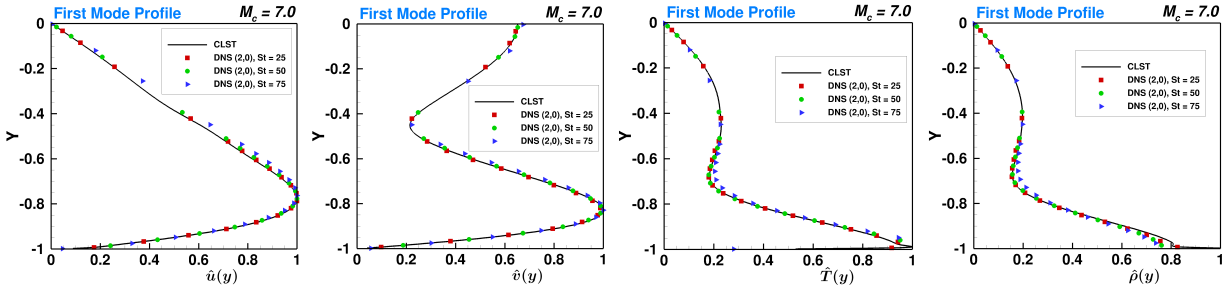

Figure 3.13: Mode shape comparison between single mode GKM simulation and LST at $M_c = 7$.

Mach Number	Most Unstable Wavenumber (LST)	Dominant Wavenumber (GKM)
3.0	$(5, 0)$	$(5, 0)$
4.5	$(3, -1)$	$(3, 0)$
6.0	$(4, 0)$	$(4, 0)$
7.0	$(2, 0)$	$(2, 0)$

Table 3.2: Comparison of dominant wavenumbers in LST and random inflow GKM simulations.

evolution for these cases around $St \sim 75$. This behavior can be attributed to significant nonlinear effects within the flow field at this instant. The excellent comparisons presented here validate GKM to capture the correct energy growth rate as predicted using linear analysis and retain the initialized perturbation shape. We now proceed to validate GKM using broadband random initial perturbations.

3.4.3 Broadband random initial perturbations

GKM is shown to capture the growth rate and retain the mode shape when the corresponding most unstable mode is initialized until nonlinear effects start to dominate. However, perturbations in reality are randomly distributed which lead to the formation of instabilities. Therefore, simulations of randomly perturbed pressure field are performed for the five Mach numbers considered previously with base flow properties listed in table 3.1. Hader and Fasel [2019] have shown similar breakdown mechanism occurs in randomly perturbed boundary layers as that in controlled transition initialized with most unstable modes computed by LST. Therefore, randomly perturbed acoustic field simulations are performed for validation of GKM. These simulations provide two fold benefits over the single mode simulations. First, random perturbations remove any bias in the initial flow field and second, initialising the pressure field emphasizes the pressure-velocity interactions via pressure-dilatation for high speed flows. After passage of initial transience, the wavenumber of the most unstable mode is calculated at near-wall, intermediate and far-wall locations and compared with LST. Finally, similar to the single mode simulations, the mode shapes and asymptotic growth rates are also compared at later times.

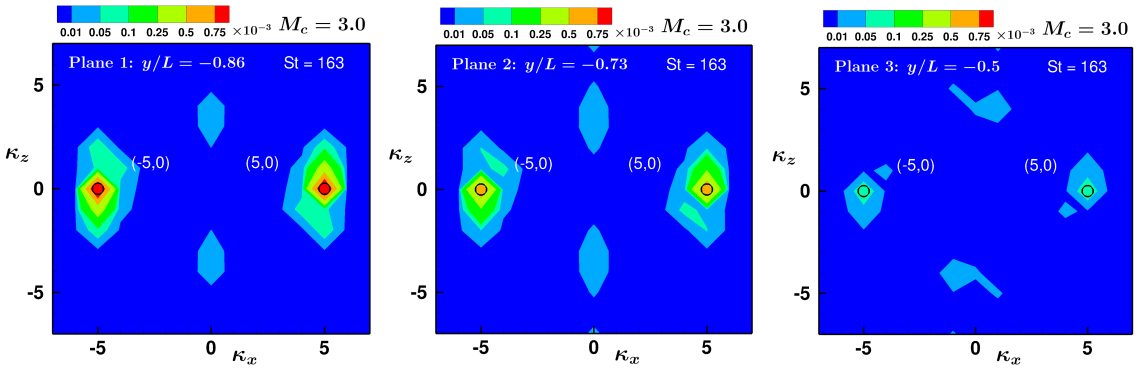

Figure 3.14: Dominant wavenumber comparison between GKM and LST at three planes for $M_c = 3$.

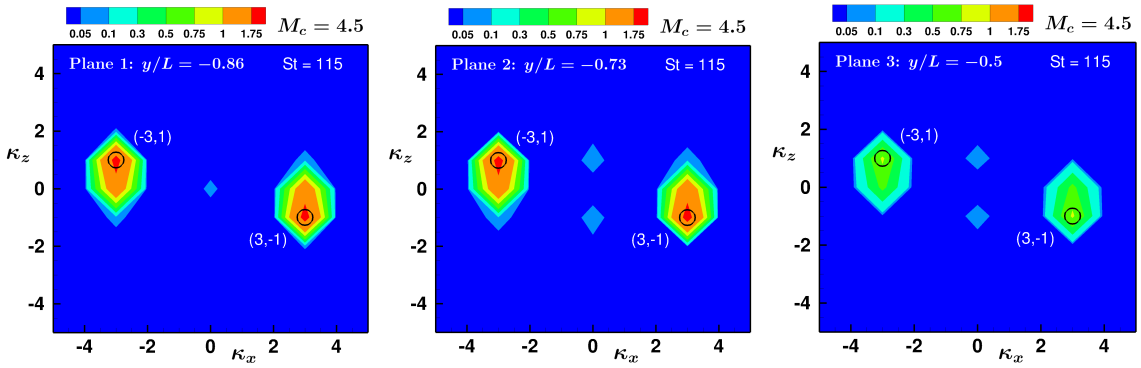

Figure 3.15: Dominant wavenumber comparison between GKM and LST at three planes for $M_c = 4.5$.

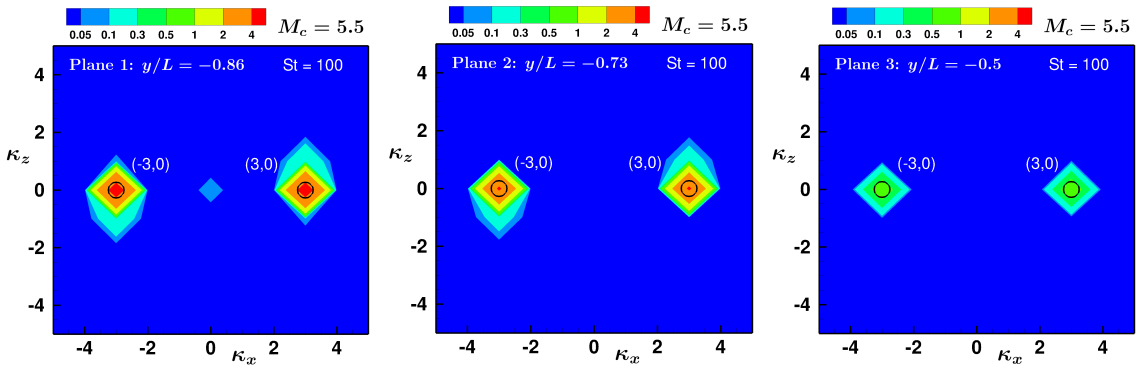

Figure 3.16: Dominant wavenumber comparison between GKM and LST at three planes for $M_c = 5.5$.

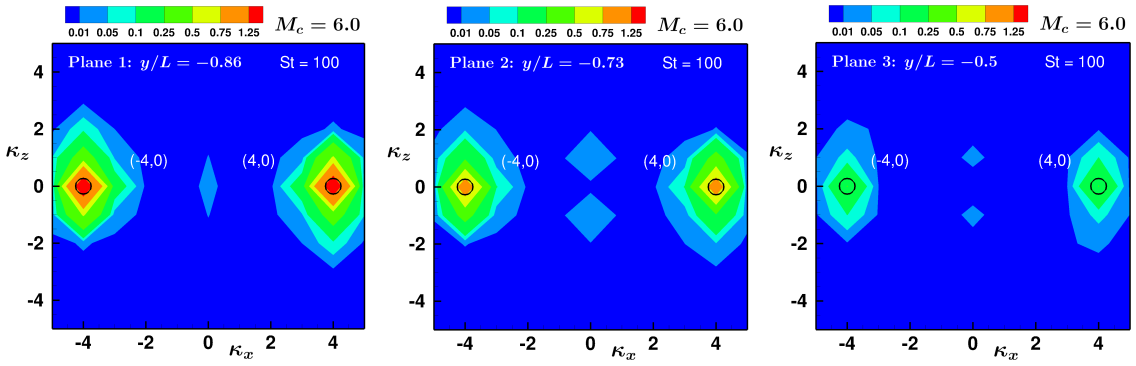

Figure 3.17: Dominant wavenumber comparison between GKM and LST at three planes for $M_c = 6$.

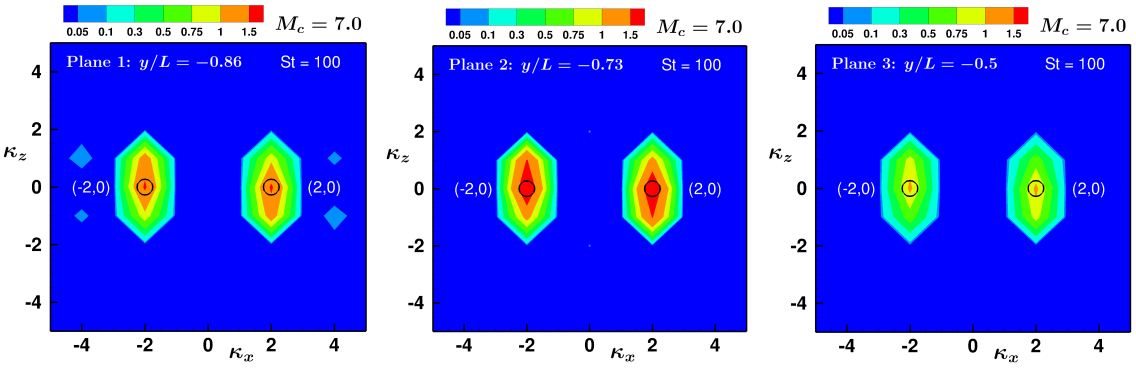

Figure 3.18: Dominant wavenumber comparison between GKM and LST at three planes for $M_c = 7$.

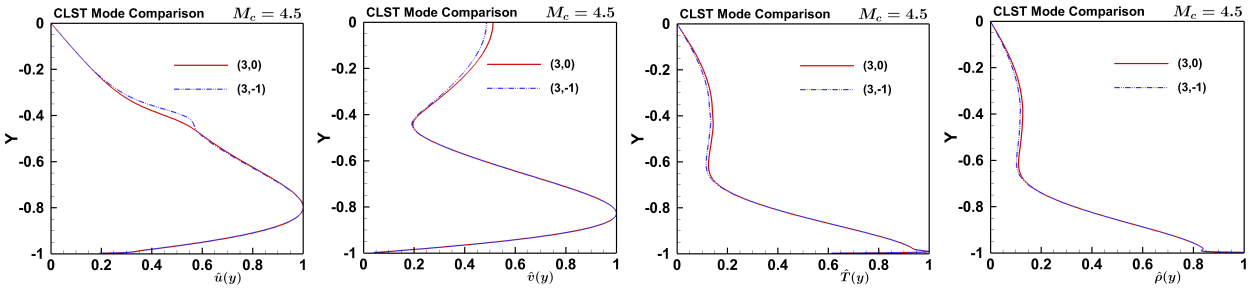

Figure 3.19: Mode shape comparison between unstable modes $(3, 0)$ and $(3, -1)$ for $M_c = 4.5$.

We first verify the dominant wavenumbers after lapse of initial transience for each Mach number. Figures 3.14, 3.15, 3.16, 3.17 and 3.18 show the two-dimensional spectral spread for Mach numbers 3, 4.5, 5.5, 6, and 7 respectively. The most energetic wavenumbers are identified on the figures which can be compared against LST results in figure 3.3 (most unstable wavenumbers identified on the figure). The comparison of dominant wavenumbers is also summarized in table 3.2. With the exception of $M_c = 4.5$, all simulations show a streamwise mode or two-dimensional mode to be the most dominant similar to LST predictions. Furthermore, the streamwise wavenumber matches exactly with the one predicted by linear analysis for all cases. For $M_c = 4.5$, the most energetic wavenumber is slightly oblique or three-dimensional, $(3, -1)$, compared to the two-dimensional wavenumber, $(3, 0)$, estimated by LST. Linear analysis predicts $(3, \pm 1)$ as the second most unstable wavenumber with only slightly smaller growth rate. Xie et al. [2017] have shown that compressibility suppresses streamwise modes and the suppression effect of compressibility reduces as the obliqueness of the mode increases. They establish that effective gradient Mach number, defined as

$$M_g^e = \frac{S}{\kappa a}\cos\beta \quad \text{where} \quad S = \frac{\partial \overline{U}}{\partial y}, \tag{3.21}$$

is the relevant parameter in identifying the suppression effect of compressibility. Here, β is the angle between the wave-vector and the streamwise direction and is defined as,

$$\beta = \tan^{-1}\left(\frac{\kappa_z}{\kappa_x}\right). \tag{3.22}$$

The parameter M_g^e reduces with increasing obliqueness diminishing the effect of compressibility. Also, the mode shapes for $(3, 0)$ and $(3, -1)$ as calculated from LST are very similar as evident from figure 3.19. Competing growth rates, similar mode shapes and the suppression of streamwise modes due to compressibility can cause oblique modes to dominate in the flow field. Also, various spanwise modes ($\kappa_x = 0$) appear in the kinetic energy spectrum which are predicted as stable by LST. The nonlinear interactions lead to the formation of spanwise modes which are unaffected by compressibility preserving the lift-up mechanism (Ellingsen and Palm [1975]).

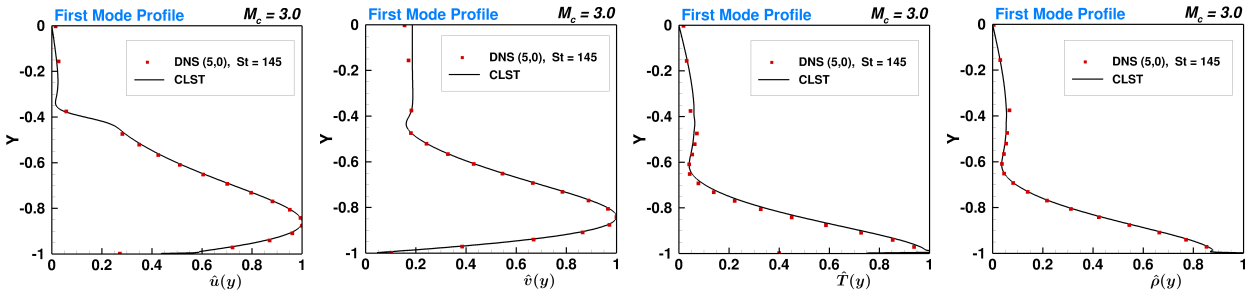

Figure 3.20: Mode shape comparison between broadband GKM simulations and LST results for $M_c = 3$.

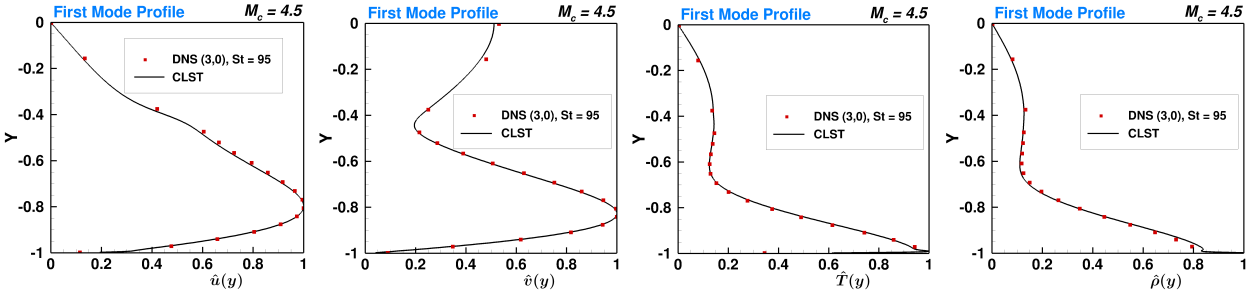

Figure 3.21: Mode shape comparison between broadband GKM simulations and LST results for $M_c = 4.5$.

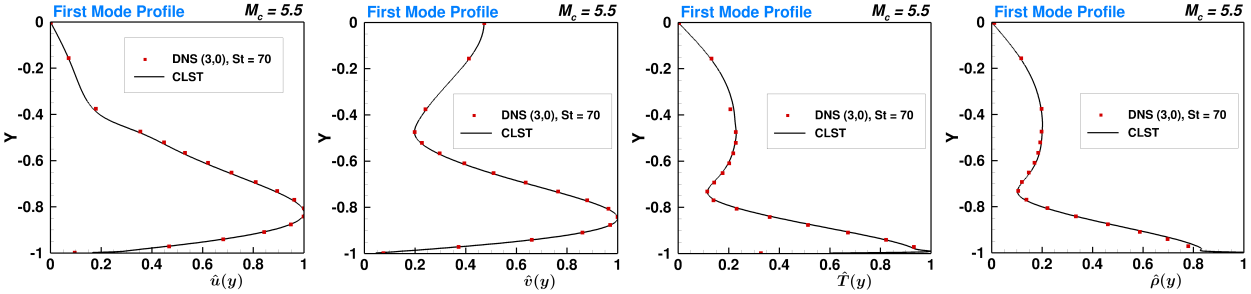

Figure 3.22: Mode shape comparison between broadband GKM simulations and LST results for $M_c = 5.5$.

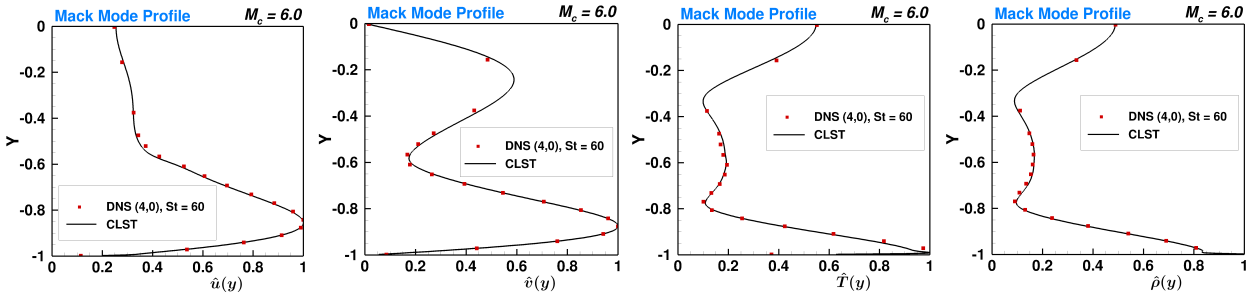

Figure 3.23: Mode shape comparison between broadband GKM simulations and LST results for $M_c = 6$.

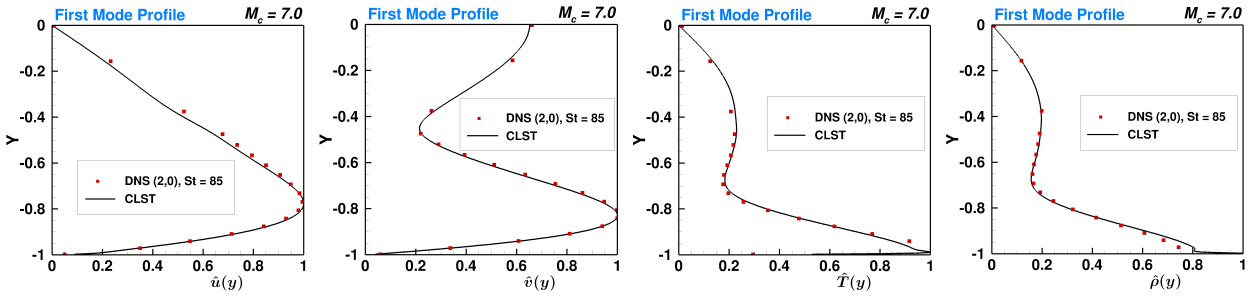

Figure 3.24: Mode shape comparison between broadband GKM simulations and LST results for $M_c = 7$.

We now compare the mode shape of the most unstable mode for all the flow variables between GKM and LST. Since a two-dimensional mode is the most unstable, mode shapes of only streamwise and wall-normal velocity components are compared along with density and temperature. Figures 3.20, 3.21, 3.22, 3.23 and 3.24 show excellent comparison between LST and GKM for the mode shape of the most unstable mode at Mach numbers $3,\ 4.5,\ 5.5,\ 6,$ and 7 respectively. This establishes that GKM effectively forms the instabilities predicted through linear theory with no prior bias in the initial conditions. The randomly initialized pressure field leads to accurate capture of instabilities in the velocity field establishing the ability of GKM to correctly capture the velocity-pressure interactions at high Mach numbers.

We have previously established that GKM captures the growth rate of the most unstable mode using single mode initialization for all considered Mach numbers. We calculate the growth rate of turbulent kinetic energy, ω, for randomly initialized cases as,

$$\omega = \frac{1}{k}\frac{dk}{dt}, \tag{3.23}$$

where $k = \overline{\rho u_i'' u_i''}/2$ is the volume averaged turbulent kinetic energy. Figure 3.25 compares the overall kinetic energy growth rate from GKM simulation against the most unstable growth rate through LST for all Mach numbers. The growth rate varies very rapidly in the initial stages due to the random inflow condition. However, in all cases turbulent kinetic energy growth rate plateaus for a duration of 20-30 shear times (highlighted area). The plateau appears around the time when

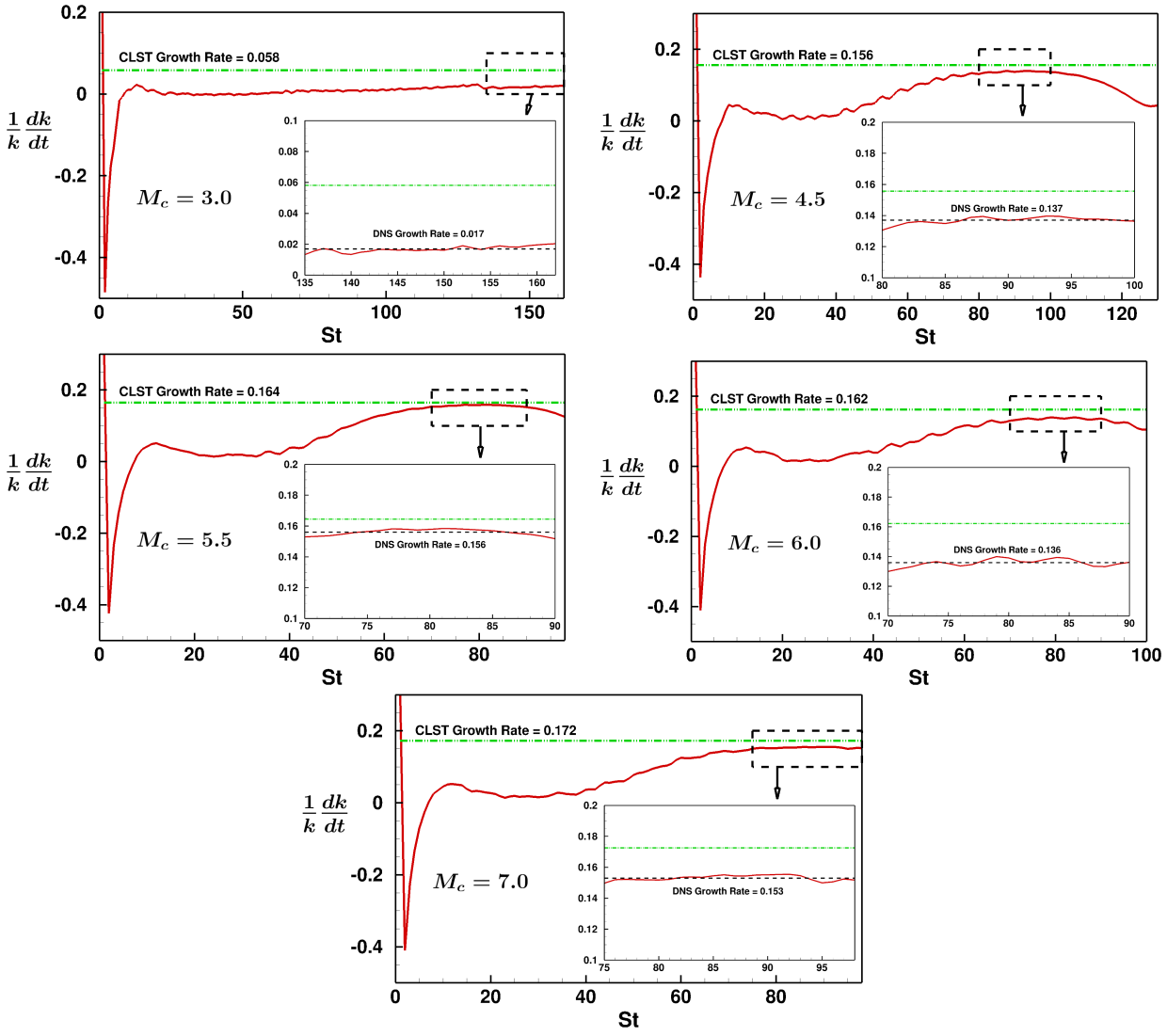

Figure 3.25: Overall turbulent kinetic energy growth rate for broadband random initialization compared against growth rate of most unstable mode.

initial transience has passed and the most unstable mode is begins to dominate. An average asymptotic growth rate from the DNS data is calculated in this region and compared against the growth rate of the most unstable mode in LST. In all high speed cases considered here, the asymptotic growth rate of overall turbulent kinetic energy is observed to be relative lower compared to the most unstable growth rate predicted through linear theory. As established before, high speed flows exhibit multiple instabilities spread across a range of wavenumbers. Broadband random flow initialization causes unstable modes at all wavenumbers to form after passage of initial transience. These modes grow at a lower rate compared to the most unstable mode causing the overall kinetic energy growth rate to drop relative to the most unstable mode. Some nonlinear interactions can also be expected in the flow causing energy to move from the most unstable wavenumber to other wavenumbers reducing the overall growth rate.

3.5 Conclusions

The change in the fundamental nature of pressure as a function of Mach number causes the nature of instabilities to change significantly in high-speed flows. In this study, we perform linear stability analysis to characterize dominant instabilities over a range of Mach numbers in benchmark Poiseuille flow. The stability analysis of the linearized perturbation equations as outlined by Mack [1975] is carried to compute unstable modes, its type (first, Mack or higher order mode) and the corresponding growth rate. We analyze the dominant modes as a function of Mach number in the range $[2.5, 9.5]$ and establish different Mach regimes based on the type of dominant instability. Similar to boundary layers, the dominant instability shifts from first to Mack mode at high Mach numbers ($M_c > 5.8$). It is observed that the first mode again becomes dominant after $M_c > 6.3$ and finally higher modes dominate at $M_c > 8.8$. The stabilization of low wavenumber perturbations due to the effects of compressibility is also reaffirmed.

The findings of the linear stability analysis are further investigated using numerical simulations of gas-kinetic method (GKM-DNS). The comparison of linear analysis findings with the GKM-DNS results also serves to validate the GKM approach and the numerical code. The computational study is performed using two sets of simulations, low intensity single mode and broadband random

inflow initialization. The single mode simulations establish the ability of GKM to effectively capture the energy growth rate as predicted by LST. The initialized mode shape of the most unstable mode is also shown to be retained for a long duration for each Mach number considered. These simulations provide a direct comparison of GKM against LST. However, the flow perturbations in practical applications are random in nature. Therefore, broadband random inflow simulations are performed to remove any bias in the initial perturbation field. It is established that even with random inflow the most unstable wavenumbers predicted using linear theory dominate after passage of initial transience in GKM simulations. The mode shape in these wavenumbers is also shown to compare well with linear theory predictions establishing the ability of GKM to effective capture the linear theory instabilities. These insights in the linear regime and the validation of GKM are important before analyzing the effect of compressibility on key nonlinear processes such as spectral cascade of energy and breakdown toward turbulence.

4. NONLINEAR EVOLUTION OF PERTURBATIONS IN HIGH MACH NUMBER WALL-BOUNDED FLOW: PRESSURE-DILATATION EFFECTS[1]

Pressure undergoes a transformative change as the Mach number increases from incompressible to compressible regime. In incompressible flows, pressure is a Lagrange multiplier governed by the Poisson equation and its sole purpose is to maintain a divergence-free velocity field. At high Mach numbers pressure is a thermodynamic state variable and its evolution is governed by energy conservation and state equations. Emergence of wave-like character in the pressure field engenders a dilatational velocity component at high Mach numbers. Flow-thermodynamic interactions enabled by the dilatational field become significant and profoundly affect the flow field. The pressure field performs work on the velocity field via the pressure-dilatation interaction leading to kinetic-internal energy exchange.

Compressibility effects in the linear stability regime and fully developed turbulence have been reasonably well investigated in literature. Compressible Linear stability theory (CLST) by Mack [1975] identifies compressible unstable modes using linear analysis of unsteady Navier-stokes equations for parallel-streamline boundary layer flows. LST has been used extensively to investigate early stages of transition towards turbulence in compressible flows - Mack [1984], Reed et al. [1996] and Malik [1989]. The parabolized stability equations (PSE) developed by Bertolotti and Herbert [1991] and Herbert [1997] include nonparallel effects and have been utilized to study transition on flat plates. Contrary to the incompressible LST, which shows only first mode instability as determined using the Orr-Sommerfeld (OS) equation, the CLST analysis shows multiple higher order unstable modes at high Mach numbers. At moderately high Mach numbers the growth rate is dominated by the first mode, however, the second mode or the Mack mode is most unstable in the hypersonic regime. The second mode plays an important role in hypersonic laminar turbulent transition process leading to extensive aerodynamic heating as shown by the experimental studies

[1]Reprinted with permission from "Nonlinear evolution of perturbations in high Mach number wall-bounded flow: Pressure-dilatation effects" by Ankita Mittal and Sharath S. Girimaji, 2020. Physics of Fluids, 32, 036101, Copyright [2020] by American Institute of Physics

of Zhang et al. [2015], Zhu et al. [2018] and Zhu et al. [2020]. The stabilization/destabilization effect on the second mode due to different wall conditions such as uneven wall blowing Miró Miró and Pinna [2018], local heating/cooling Bountin et al. [2018] etc. is often studied as a means to understand and control the transition process. Fedorov [2011] summarizes the state-of-the-art of LST and PSE investigations of stability and scenarios of transition in high speed boundary layer flows. Similar stability analyses have been performed for mixing layers by Lessen et al. [1965], Blumen [1970] and Jackson and Grosch [1989]. An initial value analysis using rapid distortion theory (RDT) for compressible homogeneous shear flows was carried out by Simone et al. [1997], Livescu and Madnia [2004], Bertsch et al. [2012] and Kumar et al. [2014]. In Poiseuille flows, Butler and Farrell [1992] perform a modal analysis of linearized equations while a transient non-modal analysis is presented by Xie et al. [2017] highlighting the effect of compressibility in the linear regime. Shock-turbulence interactions have also been reasonably well examined - Andreopoulos et al. [2000], Larsson et al. [2013] and Clemens and Narayanaswamy [2014]. Miura and Kida [1995] and Lee et al. [2016] examine the effect of pressure-dilatation in isotropic turbulence and on the nonlinear process of return to isotropy of unforced periodic-box turbulence respectively. Compressibility effects on fully developed turbulence have also been studied in many works with the aim of modeling the fundamental mechanisms - Lele [1994], Sarkar [1995], Huang et al. [1995] and Gomez and Girimaji [2013, 2014].

The effect of compressibility on transient nonlinear flow processes is much less investigated in literature. Study of nonlinear development of velocity perturbations is critically important for understanding and modeling breakdown toward turbulence in hypersonic boundary layers Sivasubramanian and Fasel [2014, 2015] and Franko and Lele [2013]. Specifically, the nonlinear spectral growth from initial perturbations to a broad energy spectrum is a key aspect of breakdown toward turbulence. In a series of recent works Fasel and co-workers have investigated various aspects of breakdown toward turbulence of hypersonic boundary layers over flared cones. Fundamental breakdown [Hader and Fasel, 2019] and effect of random inflow conditions [Hader and Fasel, 2018] in flows over flared cones have been examined. The breakdown process in flows over straight

and flared cones are compared in Meersman et al. [2018]. Some of the recent efforts toward understanding hypersonic breakdown is summarized in Chynoweth et al. [2019]. Jahanbakhshi and Zaki [2019] recently evaluated nonlinearly most susceptible inflow disturbance leading to the earliest laminar-to-turbulence transition. They highlight the importance of including nonlinear effects so as to accurately predict the transition location.

Despite recent progress, many important fundamental aspects of nonlinear processes - specifically those due to the change in the action of pressure - are not well understood. It is well known that dilatational fluctuations exhibit vastly different spectral transfer characteristics than solenoidal velocity field [Wang et al., 2013, Praturi and Girimaji, 2019]. Further, the effect of energy exchange between kinetic and internal forms on spectral evolution is not established in wall-bounded flows. Recall that in incompressible turbulence, kinetic energy is conserved in the nonlinear spectral transfer process. It is therefore reasonable to expect transient spectral evolution in incompressible and compressible flows to be different. Thus motivated, the goal of this work is to examine the nonlinear spectral evolution in high-speed wall-bounded flows with a focus on pressure effects. Due to its simple geometry and intrinsic scientific value, Poiseuille flow has long been used to study wall effects on turbulence and other nonlinear fluid phenomena. Indeed, incompressible turbulent Poiseuille or channel flow is one of the most widely investigated flows in literature. Therefore, it is reasonable to investigate compressible Poiseuille flow to understand fundamental nonlinear processes in wall-bounded flows before proceeding to other flow configurations. Further, to isolate the influence of pressure fluctuations from other high enthalpy flow effects, we uniformly initialize the background temperature and density. Once the fundamental pressure effects are clearly understood, the influence of initial spatial variations in background density and temperature can be examined with greater clarity.

The objective of this study is to characterize the compressibility effects on the nonlinear development of perturbations in canonical high speed wall-bounded shear flow. The study methodology includes contrasting the perturbation development in equivalent high and low speed flows. The contrast is performed in two parts, first where both flow regimes (high and low Mach flow) are

initialized with similar perturbation field and second where each flow regime is initialized with its corresponding most unstable mode as determined using linear stability analysis. The first contrast enables a direct comparison of perturbation development highlighting the effect of compressibility and relevant important parameters. On the other hand, the second provides a more realistic qualitative contrast where the previously identified important parameters can be tested. Toward this end, we undertake the following tasks:

1. Analyse the governing equations to establish the key role of pressure-dilatation on the nonlinear evolution of perturbations.

2. Perform direct numerical simulations of perturbation evolution (linear and early nonlinear stages) in Poiseuille flows at incompressible and compressible Mach numbers.

3. Examine the effect of pressure-dilatation on internal energy evolution and kinetic energy spectral growth at different Mach numbers.

4. Examine the spectral growth in different wall-normal regions of high Mach number Poiseuille flow as a function of local pressure-dilatation level.

The chapter is organized as follows. The governing equations along with a brief analysis of kinetic-internal energy interactions are presented in §4.1. Description of the numerical scheme used to perform DNS and problem setup are given in §4.2. DNS results are presented in §4.3 along with a detailed discussion of the findings. The chapter concludes with a concise summary of the important observations and inferences in §4.4.

4.1 Governing equations

The ideal gas law and compressible Navier-Stokes equations govern the flow evolution considered here:

$$\frac{\partial \rho}{\partial t} + \frac{\partial}{\partial x_j}(\rho u_j) = 0, \tag{4.1a}$$

$$\frac{\partial (\rho u_i)}{\partial t} + \frac{\partial (\rho u_i u_j)}{\partial x_j} = -\frac{\partial p}{\partial x_i} + \frac{\partial \tau_{ij}}{\partial x_j}, \tag{4.1b}$$

$$\frac{\partial}{\partial t}\left(\frac{p}{\gamma - 1}\right) + \frac{\partial}{\partial x_j}\left(\frac{p u_j}{\gamma - 1}\right) = \frac{\partial}{\partial x_j}\left(\kappa \frac{\partial T}{\partial x_j}\right) - p\frac{\partial u_k}{\partial x_k} + \tau_{ij}\frac{\partial u_i}{\partial x_j}, \tag{4.1c}$$

$$p = \rho R T, \tag{4.1d}$$

where ρ is the fluid density, u_i is the velocity component, p is the gas pressure, τ_{ij} is the viscous stress tensor, γ is the specific heat ratio, κ is the coefficient of thermal conductivity, T is the temperature, x_i is the spatial coordinate and t is time. The viscous stress tensor is given by:

$$\tau_{ij} = \mu\left(\frac{\partial u_i}{\partial x_j} + \frac{\partial u_j}{\partial x_i}\right) - \frac{2}{3}\mu\frac{\partial u_k}{\partial x_k}\delta_{ij}, \tag{4.2}$$

where μ is the coefficient of dynamic viscosity and δ_{ij} is the Kronecker delta. A calorically perfect gas is considered and the Prandtl number (Pr) is set to 0.7. The specific heat ratio (γ) is 1.4 and the dynamic viscosity is assumed to follow Sutherland's law [Heiser and Pratt, 1994]:

$$\mu = \mu_0\left(\frac{T}{T_0}\right)^{3/2}\frac{T_0 + C}{T + C}, \tag{4.3}$$

where $T_0 = 273.15\ K$ is the reference temperature, $\mu_0 = 1.716 \times 10^{-5}\ kg\,m\,s^{-1}$ is the viscosity at the reference temperature and $C = 110.4\ K$ is the Sutherland temperature. These equations are used to perform the direct numerical simulations (DNS).

The objective of this study is to examine the development of perturbations in planar wall-bounded shear flow as shown in figure 3.1. We consider a base flow with parallel streamlines given

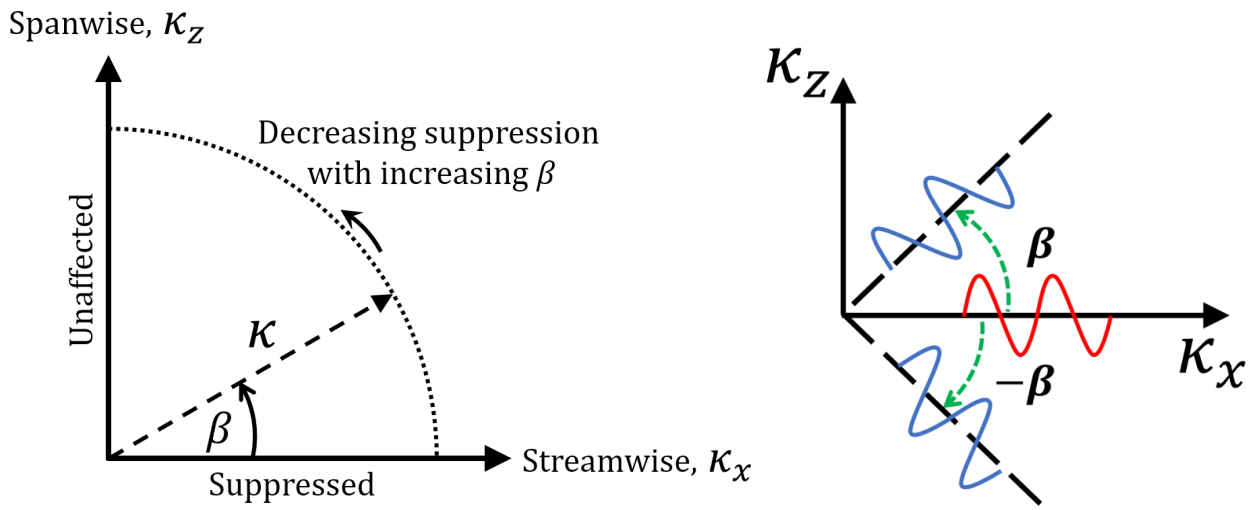

Figure 4.1: Effect of compressibility suppression based on obliqueness of wave-vector and initial triad of perturbations.

by:

$$\overline{U}_i = [\overline{U}(y,t), 0, 0]. \tag{4.4}$$

Here, x is the streamwise direction, y is the wall-normal direction, z is the spanwise direction and t is time. Perturbations that are periodic in x and z directions with the amplitude varying with the wall-normal distance and time are considered:

$$u_i' = \hat{u}_i(y,t)e^{\iota(\kappa_x x + \kappa_z z)}, \tag{4.5}$$

where κ_x and κ_z are the initial perturbation wavenumbers in the streamwise and spanwise directions and $\iota = \sqrt{-1}$ is the unit imaginary number. Xie et al. [2017] studied the linear development of these perturbations as a function of perturbation obliqueness angle, β, which is defined as:

$$\beta = \cos^{-1}\left(\frac{\kappa_x}{\kappa}\right), \tag{4.6}$$

where $\kappa = \sqrt{\kappa_x^2 + \kappa_z^2}$ is the wavenumber magnitude in the $x - z$ plane. The focus of this study is on the nonlinear development of an initial triad of perturbations (as shown in figure 4.1) for various

combinations of wave-vector obliqueness and amplitude ($\hat{u}_i$) profiles.

4.1.1 Linear regime inferences

In the linear regime, modal and initial value problem analyses have been carried out by Butler and Farrell [1992] and Xie et al. [2017]. Before proceeding to the analysis in the nonlinear regime, we present a brief summary of inferences from linear regime analysis preformed by Xie et al. [2017].

1. An effective gradient Mach number, M_g^e is introduced based on the obliqueness angle, β as shown in figure 4.1. This M_g^e governs the effect of compressibility and is given by,

$$M_g^e = \frac{S}{\kappa \overline{c}} \cos \beta, \tag{4.7}$$

   where S is the local mean shear, κ is the wavenumber and $\overline{c}$ is the average speed of sound.

2. M_g^e is highest for streamwise ($\beta = 0$ or $\kappa_z = 0$) modes and therefore, these modes experience significant compressibility effects in high speed flows. The effective gradient Mach number for these modes is given by,

$$M^e_{g,\,\beta=0} = \frac{S}{\kappa \overline{c}}, \tag{4.8}$$

   which is the gradient Mach number (M_g).

3. Modes with $\beta \in [0^\circ, 90^\circ]$ experience intermediate compressibility effects which decrease with increasing β.

4. M_g^e is zero for spanwise ($\beta = 90^\circ$ or $\kappa_x = 0$) modes and therefore, these modes are nearly unaffected by compressibility. This is called the lift-up mode and is discussed in detail by Ellingsen and Palm [1975], Landahl [1980] and Hanifi and Henningson [1998].

5. The dilatational field is nearly exclusively incumbent in the wall-normal velocity fluctuations.

6. Pressure fluctuations (p') and turbulent kinetic energy in wall-normal (dilatational) fluctuations (u_2') exhibit equipartition:

$$\overline{\rho}\left[\overline{u_2'u_2'}\right] \overset{\text{equipartition}}{\longleftrightarrow} \frac{\overline{p'p'}}{\gamma\overline{p}}. \tag{4.9}$$

The effect of obliqueness angle, β is summarized in figure 4.1 and we will later demonstrate that these features determine the dominant flow physics in the nonlinear regime as well.

4.1.2 Nonlinear analysis

We now present a brief discussion on flow-thermodynamic interactions in the nonlinear stage of perturbation evolution and discuss the implications. We first present the kinetic energy (K) and internal energy (e) equations [Miura and Kida, 1995, Franko and Lele, 2013],

$$\textbf{Kinetic energy:} \quad \frac{\partial K}{\partial t} + \frac{\partial (Ku_k)}{\partial x_k} + \frac{\partial}{\partial x_k}\Big[pu_k - \tau_{ik}u_i\Big] = p\frac{\partial u_k}{\partial x_k} - \tau_{ij}\frac{\partial u_i}{\partial x_j}, \tag{4.10a}$$

$$\textbf{Internal energy:} \quad \frac{\partial e}{\partial t} + \frac{\partial (eu_k)}{\partial x_k} + \frac{\partial q_k}{\partial x_k} = -p\frac{\partial u_k}{\partial x_k} + \tau_{ij}\frac{\partial u_i}{\partial x_j}, \tag{4.10b}$$

where,

$$K = \frac{1}{2}\rho u_i u_i, \quad q_k = -\kappa\frac{\partial T}{\partial x_k}, \quad e = \frac{p}{\gamma - 1}. \tag{4.11}$$

Equations (4.10a) and (4.10b) indicate interactions between kinetic and internal energy via pressure-dilatation and viscous action. Pressure-dilatation permits a reversible two-way exchange while viscous action can only lead to an irreversible transfer from kinetic to internal energy. As mentioned in the introduction, the purpose of this study is to investigate the effect of Mach number on kinetic energy growth and spectral transfer in the early nonlinear regime. For the ease of analysis, the viscous and thermal flux terms are suppressed in the analysis.

In the nonlinear regime, the density fluctuations are large, therefore, density-weighted statistics are used to describe the flow. Following Favre [1983], the velocity field is decomposed into a Favre

average and a corresponding fluctuation field:

$$u_i = \tilde{U}_i + u_i'' \quad \text{where,} \quad \tilde{U}_i = \frac{\overline{\rho u_i}}{\overline{\rho}}. \tag{4.12}$$

While $\tilde{(.)}$ is used to indicate Favre averaging, $\overline{(.)}$ represents Reynolds average. The inviscid evolution of the mean kinetic ($\overline{K}$) and internal ($\overline{e}$) energies is given by,

$$\frac{\partial \overline{K}}{\partial t} + \frac{\partial (\tilde{U}_k \overline{K})}{\partial x_k} + \frac{\partial}{\partial x_k}\left[\overline{K u_k''} + \overline{p u_k}\right] = \overline{p}\frac{\partial \tilde{U}_k}{\partial x_k} + \overline{p' \frac{\partial u_k''}{\partial x_k}}, \tag{4.13a}$$

$$\frac{\partial \overline{e}}{\partial t} + \frac{\partial (\tilde{U}_k \overline{e})}{\partial x_k} + \frac{\partial}{\partial x_k}\left[\overline{e u_k''}\right] = -\overline{p}\frac{\partial \tilde{U}_k}{\partial x_k} - \overline{p' \frac{\partial u_k''}{\partial x_k}}. \tag{4.13b}$$

The mean kinetic energy of the total flow has two contributions: the kinetic energy of the mean flow field and the turbulent kinetic energy which is the kinetic energy of the fluctuating field. The mean-flow kinetic energy (K_m) and turbulent kinetic energy (k) are identified as,

$$K_m \equiv \frac{1}{2}\overline{\rho}\tilde{U}_i\tilde{U}_i \quad \text{and} \quad k \equiv \frac{1}{2}\overline{\rho u_i'' u_i''} \quad \text{thus,} \quad \overline{K} = K_m + k. \tag{4.14}$$

The inviscid evolution of turbulent kinetic energy (k) in compressible flows [Chassaing et al., 2002] is given by,

$$\frac{\partial k}{\partial t} + \frac{\partial (k\tilde{U}_j)}{\partial x_j} + \frac{\partial}{\partial x_j}\left[\frac{1}{2}\overline{\rho u_j'' u_i'' u_i''} + \overline{p' u_j''}\right] = -\overline{\rho u_i'' u_j''}\frac{\partial \tilde{U}_i}{\partial x_j} + \overline{p' \frac{\partial u_k''}{\partial x_k}} - \overline{u_k''}\frac{\partial \overline{p}}{\partial x_k}. \tag{4.15}$$

4.1.2.1 Kinetic-internal energy interactions

Turbulent kinetic energy has two components, energy in solenoidal fluctuations and that in dilatational fluctuations. Only the dilatational component of turbulent kinetic energy interacts with internal energy. Previous studies of compressible shear flows have shown dilatational field to be dominated by the wall-normal component of velocity perturbations [Livescu and Madnia, 2004, Xie et al., 2017]. The inviscid evolution of the wall normal component of turbulent kinetic energy

($k_{(2)} = \overline{\rho u_2'' u_2''}/2$), which is approximately the dilatational kinetic energy, is given by:

$$\frac{\partial k_{(2)}}{\partial t} + \frac{\partial (k_{(2)} \tilde{U}_j)}{\partial x_j} + \frac{\partial}{\partial x_j}\left[\frac{1}{2}\overline{\rho u_j'' u_2'' u_2''} + \overline{p' u_2''}\delta_{j2}\right] = -\overline{\rho u_2'' u_j''}\frac{\partial \tilde{U}_2}{\partial x_j} + \overline{p'\frac{\partial u_2''}{\partial x_2}} - \overline{u_2''}\frac{\partial \overline{p}}{\partial x_2}. \quad (4.16)$$

The normalized pressure-variance is the potential energy incumbent in the pressure fluctuations [Sarkar et al., 1991, Xie et al., 2017] and is also proportional to the turbulent internal energy as shown by Mittal and Girimaji [2019]. Thus, to clearly identify the kinetic-internal energy interactions in the nonlinear stage, we consider the inviscid evolution of normalized pressure-variance [$\overline{p'p'}/(2\gamma\overline{p})$]:

$$\begin{aligned}\frac{1}{2\gamma\overline{p}}\left[\frac{\partial(\overline{p'p'})}{\partial t} + \frac{\partial(\overline{p'p'}\tilde{U}_k)}{\partial x_k} + \frac{\partial}{\partial x_k}\left(\overline{p'p'u_k''}\right)\right] &= -\frac{\overline{p'u_k''}}{\gamma\overline{p}}\frac{\partial \overline{p}}{\partial x_k} - \overline{p'\frac{\partial u_k''}{\partial x_k}} \\ &\quad -\left(1 - \frac{1}{2\gamma}\right)\frac{1}{\overline{p}}\left[\overline{p'p'}\frac{\partial \tilde{U}_k}{\partial x_k} + \overline{p'p'\frac{\partial u_k''}{\partial x_k}}\right].\end{aligned} \quad (4.17)$$

As mentioned earlier, the velocity gradients in the wall-normal component in planar shear flows are dominant leading to the following approximation [Livescu and Madnia, 2004, Xie et al., 2017]:

$$\overline{p'\frac{\partial u_k''}{\partial x_k}} \sim \overline{p'\frac{\partial u_2''}{\partial x_2}}. \quad (4.18)$$

It is evident that pressure-dilatation leads to a harmonic exchange between normalized pressure-variance and the wall-normal component of turbulent kinetic energy $k_{(2)}$. Due to the harmonic nature of this interaction, equipartition of energy between these two energy forms can be expected. The levels of energy in wall-normal velocity fluctuations and pressure fluctuations will be examined using DNS data later in the chapter.

4.1.2.2 Kinetic energy evolution and spectral transfer rate

The three major inviscid mechanisms that influence the evolution of k can be identified from eq. (4.15) as: production $\left(P_k = -\overline{\rho u_i'' u_j''}\frac{\partial \tilde{U}_i}{\partial x_j}\right)$, pressure-dilatation mechanism $\left(\overline{p'd''} = \overline{p'\frac{\partial u_k''}{\partial x_k}}\right)$ and pressure work on mean of Favre fluctuations $\left(\overline{u_k''}\frac{\partial \overline{p}}{\partial x_k}\right)$. In the early nonlinear regime, the

last term is likely to be small compared to production and pressure-dilatation. Therefore, P_k and $\overline{p'd''}$ remain as the two important inviscid mechanisms affecting the evolution of turbulent kinetic energy and spectral transfer. We propose that the pressure-dilatation to production ratio is the important non-dimensional parameter that governs the degree of compressibility effect on kinetic energy evolution. Thus,

$$\begin{aligned} |\overline{p'd''}| \; > \; |P_k| \quad &=> \quad \text{Large compressibility effects,} \\ |\overline{p'd''}| \; < \; |P_k| \quad &=> \quad \text{Small compressibility effects.} \end{aligned} \tag{4.19}$$

A key objective of this study is to examine the effect of compressibility on the spectral transfer of energy and the rate of formation of secondary scales of motion. In incompressible flows, the spectral transfer of turbulent kinetic energy across different scales of motion is governed by triadic interactions in the advective term. The spectral energy distribution is examined by performing Fourier transform of the perturbation velocity field (u_i'). In compressible flows, the physics of the spectral transfer of turbulent kinetic energy is incumbent in the quartic advection term $\left(\frac{1}{2}\rho u_j'' u_i'' u_i''\right)$. Spectral transfer rate of turbulent kinetic energy for these flows can be studied using the Fourier transform of a new variable w_i, first proposed by Kida and Orszag [1992]:

$$w_i = \sqrt{\rho} u_i''. \tag{4.20}$$

The above definition yields a positive definite spectra of the turbulent kinetic energy. Furthermore, the use of w_i as the relevant variable also reduces the spectral transfer term from quartic to triadic interactions [Praturi and Girimaji, 2019]. The spectral behavior of pressure-variance is studied using Fourier transform of p'.

We now perform DNS of Poiseuille flows at incompressible and compressible Mach numbers to (i) examine the partition of energy between wall-normal velocity and pressure fluctuations; and (ii) contrast the total turbulent kinetic energy evolution and cascade at the two Mach numbers.

	High Mach Number $M_c = 6.0$	**Low Mach Number** $M_c = 0.12$
$T\ (K)$	60	353
$\rho_0\ (kg\ m^{-3})$	0.02	1.0
$L\ (m)$	0.020032	0.020032
$U(y;t=0)\ (m\ s^{-1})$	$931.6\big(1-\frac{y^2}{L^2}\big)$	$45.2\big(1-\frac{y^2}{L^2}\big)$

Table 4.1: Initial base flow conditions.

Case	**Initial Profile**	**Initial Spectra**	**Perturbation amp. (% of U_0)**	**Initial Turbulence Intensity (I_0)**
1	OS	$\beta = (-60°, 0°, 60°)$	$(1.33, 1.33, 1.33)$	0.9%
2	OS	$\beta = (-60°, 0°, 60°)$	$(0.83, 0.83, 0.83)$	0.56%
3	OS	$\beta = (-60°, 0°, 60°)$	$(0.33, 0.33, 0.33)$	0.22%
4	OS	$\beta = (-60°, 0°, 60°)$	$(0.1, 3.8, 0.1)$	1.48%
5	OS	$\beta = (-60°, 0°, 60°)$	$(0.1, 1.0, 0.1)$	0.39%
6	OS	$\beta = (-45°, 0°, 45°)$	$(1.33, 1.33, 1.33)$	0.9%
7	Arbitrary	$\beta = (-60°, 0°, 60°)$	$(0.95, 0.95, 0.95)$	0.9%
8	Arbitrary	$\beta = (-60°, 0°, 60°)$	$(0.33, 0.33, 0.33)$	0.31%
9	Combined	$\beta = (-60°, 0°, 60°)$	$(0.6, 0.6, 0.6)$	0.7%
10	Combined	$\beta = (-60°, 0°, 60°)$	$(0.15, 0.15, 0.15)$	0.18%
11	Mack Mode	$\beta = (-60°, 0°, 60°)$	$(1.12, 1.12, 1.12)$	0.9%
12	Mack Mode	$\beta = (-60°, 0°, 60°)$	$(0.16, 0.16, 0.16)$	0.12%

Table 4.2: Simulations performed.

4.2 Numerical simulations

Direct numerical simulations are performed using a finite volume gas kinetic method (GKM) solver. Rather than the Navier-Stokes equation, this approach solves the linearized Boltzmann equation for improved applicability over a wider range of flow conditions. The BGK (Bhatnagar-Gross-Krook) collision operator is used to simplify the Boltzmann equation for describing the evolution of single particle probability density function, f [Xu, 2001]. Employing the distribution function, f, instead of continuum variables provides a good basis for addressing non-equilibrium and non-continuum effects in future works. Unlike the lattice Boltzmann method (LBM), GKM

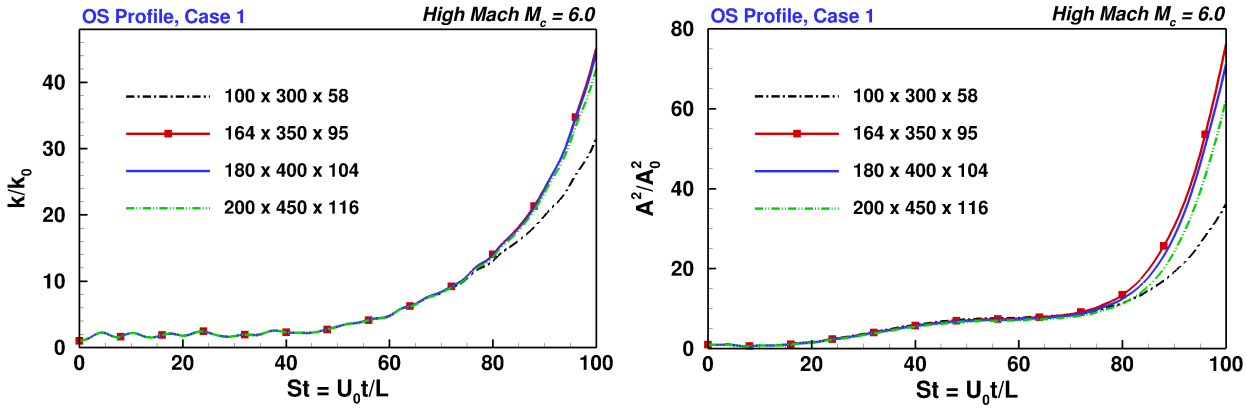

(a) (b)

Figure 4.2: Grid convergence for volume averaged (a) turbulent kinetic energy and, (b) velocity-gradient magnitude square for OS initial profile at high Mach number ($M_c = 6.0$).

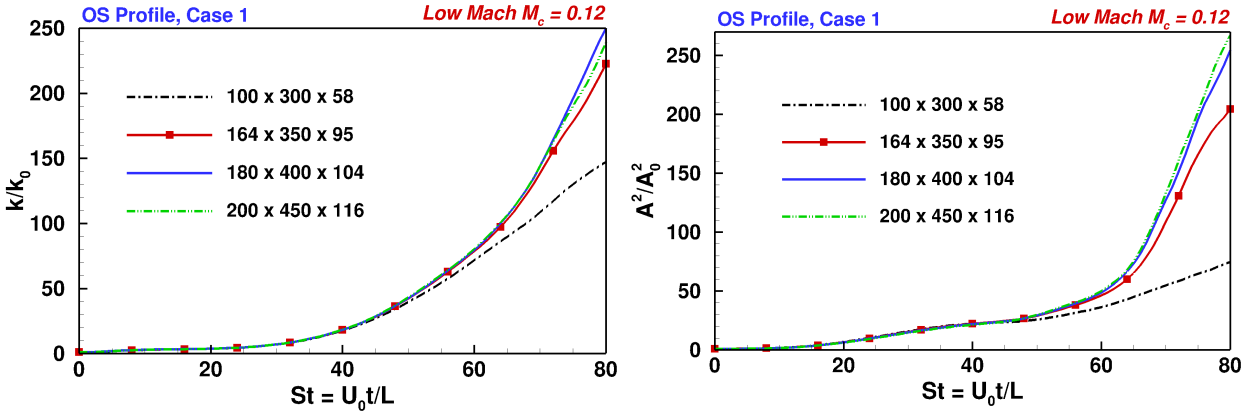

(a) (b)

Figure 4.3: Grid convergence for volume averaged (a) turbulent kinetic energy and, (b) velocity-gradient magnitude square for OS initial profile at low Mach number ($M_c = 0.12$).

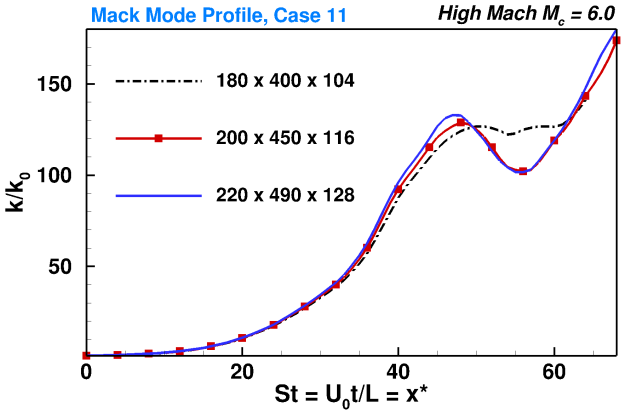

Figure 4.4: Grid convergence for volume averaged turbulent kinetic energy for Mack mode profile at high Mach number ($M_c = 6.0$).

has been shown to be well suited for both low and high speed flows [Li et al., 2005, Xu and Mao, 2006, May et al., 2007, Liao et al., 2009]. The current solver has been validated in detail in many past works of compressible wall-bounded flows [Xie et al., 2017, Xie and Girimaji, 2014]. It has also been validated for compressible decaying and homogeneous shear turbulence flows [Kumar et al., 2014, 2013] and mixing layers with Kelvin-Helmholtz instability [Karimi and Girimaji, 2017, 2016]. Further validation of the GKM code is performed against the LST results in the linear regime for wall bounded flows at the two Mach numbers considered in this study. The validation at low Mach number, $M_c = 0.12$ has been shown by Xie et al. [2017], whereas growth rate and mode shape comparisons between LST and GKM at high Mach number, $M_c = 6.0$ are presented in chapter 3 along with the details of the compressible linear stability code.

4.2.1 Problem setup

This study can be considered an extension of Xie et al. [2017] which examines the linear mechanisms. Thus, we use the same flow configuration and parameter range of investigation. The computational domain is a rectangular box of dimension $8L \times 2L \times 4.64L$. Grid cells are uniformly distributed along streamwise (x) and spanwise (z) directions. Along the wall-normal direction (y) the grid is symmetric about the channel centerline and is distributed in a geometric progression with progression coefficient of 1.0035. A Poiseuille base flow is sustained using a body force similar to the work of Xie and Girimaji [2014] and Xie et al. [2017]. The body force is chosen such that the initial pressure, density and temperature fields are spatially uniform. The Reynolds number is kept constant at $Re = \rho U_0 L/\mu = 93900$ for all simulations where, U_0 is the centerline velocity of the initial base flow. Other parameter details of the initial base flow are given in table 4.1 where T is temperature, ρ_0 is density, L is the channel half width and $U(y, t = 0)$ is the initial base flow velocity profile. The Mach number ($M_c = U_0/c$) is based on the initial centerline base velocity and speed of sound (c). The background thermodynamic state is consistent with the experiments of Semper and Bowersox [2017] and numerical simulations of Xie and Girimaji [2014], Sivasubramanian and Fasel [2015] and Xie et al. [2017].

Periodic boundary conditions are applied in the x and z directions. In the y-direction, no-slip

and no-penetration wall conditions are applied. All simulations in table 4.2 are performed using isothermal boundary condition and detailed results are presented for Cases 1, 7 and 11. Temporal simulations are performed and the evolution is considered in dimensionless shear time defined as:

$$St = x^* = \frac{U_0}{L}t. \tag{4.21}$$

4.2.2 Perturbations

The base flow is perturbed with a triad of disturbances of as shown in figure 4.1 following the studies of Sivasubramanian and Fasel [2015]. Each perturbation triad consists of one streamwise mode and a symmetric pair of oblique modes. The degree of obliqueness is characterized by β as shown in figure 4.1. The obliqueness angles are chosen to optimize the perturbation growth based on the findings of Xie et al. [2017]. Perturbations of different wall-normal shapes and amplitudes are considered. We consider the following initial perturbation profiles:

1. The incompressible Orr-Sommerfeld (OS) perturbation profile which generates Tollmien-Schlichting (TS) waves leading to first mode instability. This perturbation allows clear demarcation between well-known behavior in incompressible flows and novel effects in compressible flows. This profile will be referred to as OS initial profile in the rest of the chapter.

2. A dilatation-free arbitrary perturbation profile given by [Xie et al., 2017],

$$\begin{aligned} u_1' &= U_0 \sin\left(\pi\frac{y}{L}\right)\sin\left(2\pi\frac{x + z\tan\beta}{L_x}\right), \\ u_2' &= U_0\left(\frac{2L}{L_x}\right)\left[\cos\left(\pi\frac{y}{L}\right) + 1\right]\cos\left(2\pi\frac{x + z\tan\beta}{L_x}\right), \\ u_3' &= 0, \end{aligned} \tag{4.22}$$

   where L_x is the domain length in the streamwise direction and L is the half channel width. We will refer to this profile as the arbitrary initial profile.

3. A hybrid profile which is a linear superposition of OS and the arbitrary profiles. This profile

will be referred to as hybrid initial profile.

4. The most energetic Mack mode (at $M_c = 6.0$) determined using the eigenvalue analysis of the full set of linearized governing equations (details provided in chapter 3). This profile will be referred to as Mack mode profile.

The first three initial profiles are identical to the ones used by Xie et al. [2017]. Simulations are performed over a range of initial amplitudes. As we are interested in examining the nonlinear regime, a relatively high initial perturbation amplitude is chosen for examination along the lines of Sivasubramanian and Fasel [2015]. Lower amplitude simulations are used to identify the onset of nonlinearity.

4.2.3 Grid convergence

We perform a grid convergence study by comparing the evolution of normalized volume averaged turbulent kinetic energy and velocity-gradient magnitude square for different grid resolutions using Case 1 in table 4.2. The volume averaged turbulent kinetic energy, k and velocity-gradient magnitude square, A^2 are defined as,

$$k = \frac{1}{2}\overline{\rho u_i'' u_i''} \quad \text{and} \quad A^2 = \overline{\frac{\partial u_i'}{\partial x_j}\frac{\partial u_i'}{\partial x_j}}. \tag{4.23}$$

These are normalized with their respective initial quantities, k_0 and A_0^2. Figures 4.2 and 4.3 compare the evolution of k/k_0 and A^2/A_0^2 for high ($M_c = 6.0$) and low ($M_c = 0.12$) Mach number simulations at various grid resolutions. The figures indicate convergence in the early nonlinear regime for high Mach simulations at $164 \times 350 \times 95$ resolution and for low Mach simulations at $180 \times 400 \times 104$ for the OS Profile. Although not shown, the arbitrary profile also attains convergence at these grid resolutions. The case with Mack mode initial profile (Case 11) also exhibits convergence beyond $200 \times 450 \times 116$ as seen in figure 4.4. These grid resolutions are used to perform all simulations in table 4.2 for each Mach number. Detailed results of both Mach numbers of Case 1 are presented using a finer grid resolution of $200 \times 450 \times 116$, Case 7 using $180 \times 400 \times 104$ and that of Case 11 using $220 \times 490 \times 128$. The initial turbulence intensity is

maintained at $I_0 = 0.9\%$ for the three profiles considered for detailed discussion in this chapter – Cases 1, 7 and 11. We define the initial turbulence intensity (I_0) as,

$$I_0 = \frac{\sqrt{2k_0/\rho_0}}{U_0} \tag{4.24}$$

where, k_0 is the initial turbulent kinetic energy, ρ_0 is the initial density and U_0 is the initial centerline base flow velocity.

4.3 Results

The results are divided into four subsections. First, we examine turbulent kinetic energy (k) evolution and delineate linear and nonlinear regimes. Influence of initial perturbation energy distribution, obliqueness of perturbations and temperature boundary condition on evolution of k and the demarcation between linear and nonlinear stages is also examined. In the second subsection, the kinetic-internal energy interactions in the nonlinear stage are examined along with pressure-dilatation to production ratio. In the third subsection, an in-depth analysis of compressibility effects on spectral transfer of turbulent kinetic energy is presented. The final subsection compares the nonlinear spectral evolution trends of low and high Mach number Poiseuille flows. At each Mach number, the corresponding most unstable initial perturbation determined from linear analysis is used. For low Mach number case the OS profile is employed and for the high Mach number flow the $M_c = 6.0$ Mack mode is employed.

The results are presented for OS and arbitrary initial profiles (Cases 1–8) and Mack mode initial profile (Cases 11–12). The hybrid initial profile (Cases 9–10) is also considered and analyzed, however the results for this case are not presented as the evolution characteristics can be inferred from the findings of OS and arbitrary initial profiles.

4.3.1 Turbulent kinetic energy growth and onset of nonlinearity

Xie et al. [2017] have conducted a detailed examination of compressibility effect on flow stability and kinetic energy growth in the linear regime. The focus of the current study is on the nonlinear evolution. At the outset it is important to demarcate the boundary between linear and

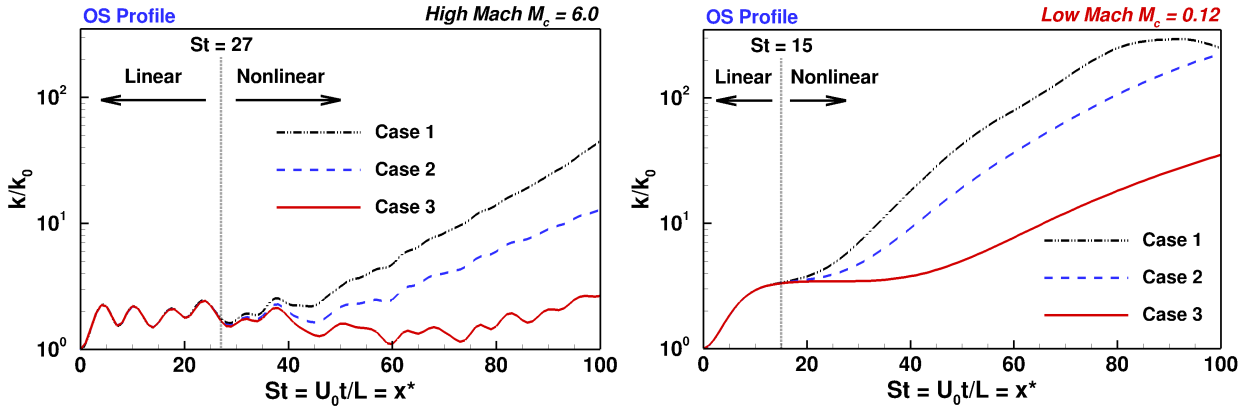

(a) (b)

Figure 4.5: Volume averaged turbulent kinetic energy evolution for different perturbation intensities with OS initial profile at (a) high ($M_c = 6.0$) and, (b) low ($M_c = 0.12$) Mach number. Initial perturbations with $\beta = 0°, \pm 60°$ are equally energized.

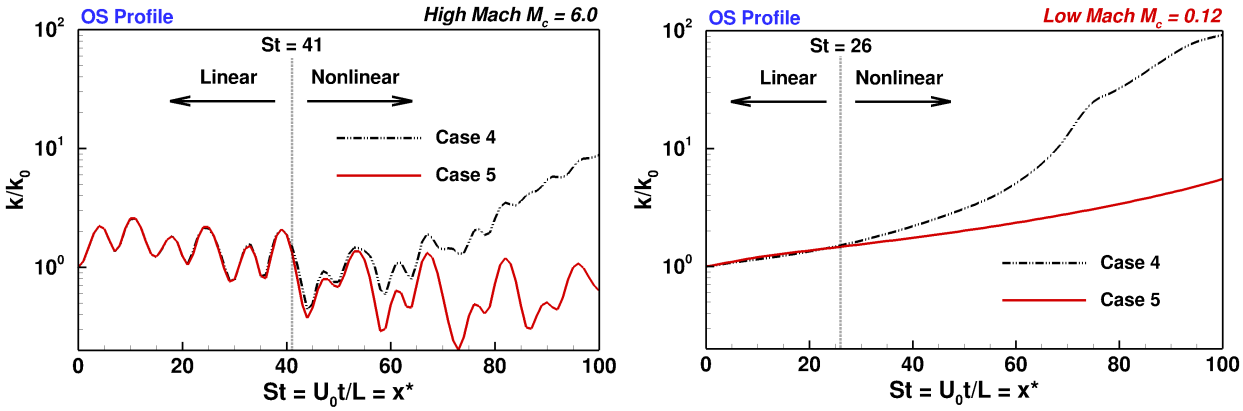

(a) (b)

Figure 4.6: Volume averaged turbulent kinetic energy evolution for different perturbation intensities with OS initial profile at (a) high ($M_c = 6.0$) and, (b) low ($M_c = 0.12$) Mach number. Initial perturbation amplitude of oblique waves ($\beta = \pm 60°$) is maintained at 0.1% each.

nonlinear regimes of perturbation evolution. Toward this end, we perform multiple simulations with different initial perturbation amplitudes (table 4.2) and compare the evolution of volume averaged turbulent kinetic energy ($k(t)$) normalized by its initial value k_0. In the linear regime, the normalized kinetic energy should be independent of the initial perturbation amplitude. Any deviation between different amplitude cases would indicate onset of nonlinearity effects. It is reasonable to infer that the highest amplitude case will exhibit nonlinear behavior earlier than lower amplitude cases. The onset of nonlinearity is, therefore, identified as the time instance at which the evolution of an initial high amplitude case deviates from that of lower initial amplitude cases. It is also verified, by examining the kinetic energy spectrum, that secondary scales are reasonably energized at this instant.

The OS initial profile leads to generation of TS waves which cause flow instability at low Mach numbers. However, as shown by Xie et al. [2017], compressibility suppresses this mode in the linear regime. In figure 4.5 we identify the time of onset of nonlinearity for the high intensity OS initial profile (Case 1). Comparing evolution of k for Cases 1–3 in table 4.2, the onset of nonlinearity for Case 1 can be estimated at $St \sim 27$ for the high Mach simulation. On the other hand, in the low Mach simulation nonlinearity is onset at $St \sim 15$. Two other qualitative differences in the overall magnitude and manner of k-evolution between high and low Mach cases can be inferred. The first difference is the oscillatory evolution of k for high Mach number case as opposed to monotonic growth in the low Mach number case. The second observation is the significant suppression in the growth rate of k for all compressible cases in the nonlinear regime. Thus, the flow stabilization due to compressibility not only leads to a prolonged linear regime but also reduces the turbulent kinetic energy growth rate in the linear and nonlinear regimes.

To establish the influence of other parameters on the onset of nonlinearity, further simulations as listed in table 4.2 are performed (Cases 4–6). Figure 4.6 compares the k evolution for cases with different energy distribution among the initial perturbation modes (Cases 4–5). For these cases, the amplitude of oblique waves ($\beta = \pm 60^\circ$) is low (0.1% of mean velocity) while the amplitude of the streamwise mode ($\beta = 0^\circ$) is considerably higher. A relatively longer linear regime is observed

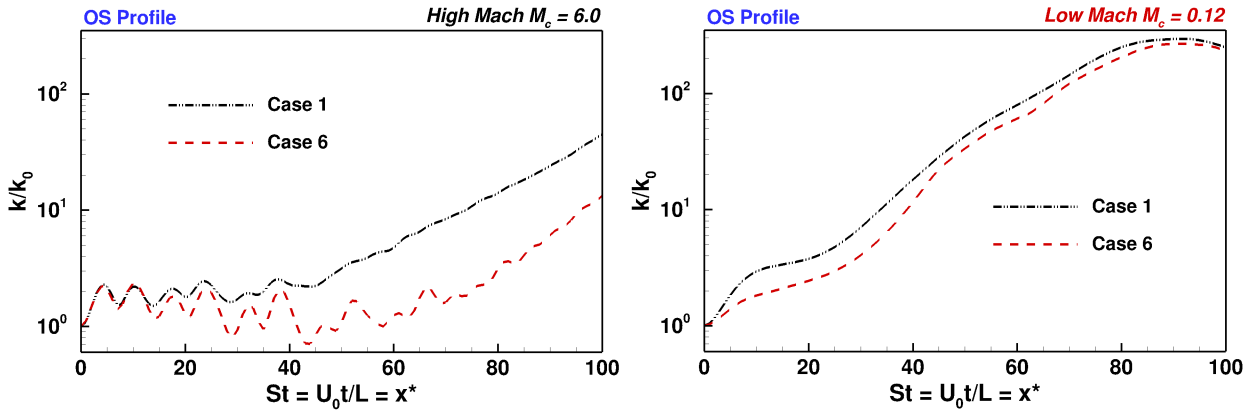

(a) (b)

Figure 4.7: Volume averaged turbulent kinetic energy evolution comparison with change in perturbation wave angle for OS initial profile at (a) high ($M_c = 6.0$) and, (b) low ($M_c = 0.12$) Mach number. Initial perturbations with $\beta = 0°, \pm 60°$ and $\beta = 0°, \pm 45°$ are equally energized.

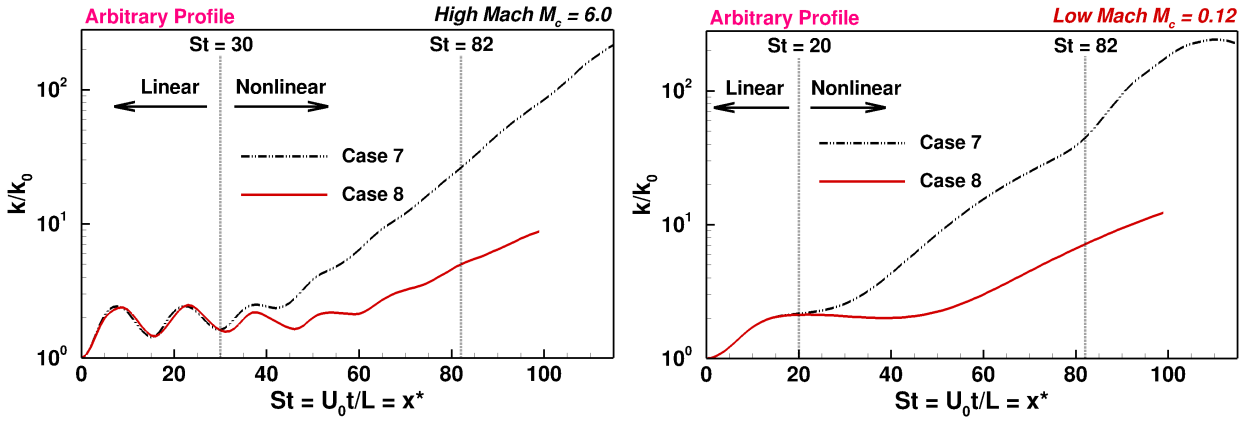

(a) (b)

Figure 4.8: Volume averaged turbulent kinetic energy evolution for different perturbation intensities with arbitrary initial profile at (a) high ($M_c = 6.0$) and, (b) low ($M_c = 0.12$) Mach number. Initial perturbations with $\beta = 0°, \pm 60°$ are equally energized.

at both Mach numbers. This is due to the fact that the strongly energized streamwise perturbation modes are most influenced by compressibility. Yet the main observations from the previous case, oscillatory evolution and suppressed growth rate at the high speed flows, are still evident. In figure 4.7 the simulations with $\beta = \pm 45^{\circ}$ initial obliqueness (Case 6) is compared with results from Case 1. Figure 4.7 reveals that change in the initial perturbation obliqueness does not affect kinetic energy evolution at low Mach numbers. However, at high Mach numbers there is a considerable change. Low β perturbations are more suppressed than higher β case. This is again due to the fact that compressibility effects diminish with increasing β [Xie et al., 2017].

We now investigate the growth of turbulent kinetic energy (k) for the so-called arbitrary initial profile at high and low Mach numbers starting from two different perturbation amplitudes - Cases 7 and 8. The results are shown in figure 4.8. Two key inferences can be drawn from the figure. In contrast to the OS-profile, in this arbitrary profile case the growth rate of turbulent kinetic energy at low and high Mach numbers are comparable. Thus compressibility does not appear to significantly suppress kinetic energy in the early nonlinear regime. Yet, there is a distinct delay in the onset of nonlinearity effects in the high Mach case – the high Mach case exhibits nonlinearity effects starting at $St \sim 30$ whereas in the low Mach case it first occurs at $St \sim 20$. Although the suppression effect due to compressibility increases after $St \sim 82$, the focus of this study is on early nonlinear regime ($St \in [30, 80]$).

We now examine the reasons for the differences in compressibility effects for different initial perturbation profiles by performing detailed analysis of Case 1 (OS initial profile) and Case 7 (arbitrary initial profile).

4.3.2 Kinetic-internal energy exchange

As mentioned in §4.1.2.1, flow-thermodynamic interactions due to pressure-dilatation mechanism leads to energy exchange between dilatational (wall-normal) velocity component ($k_{(2)} = \overline{\rho u_2'' u_2''}/2 = \overline{w_2 w_2}/2$) and the normalized pressure variance ($\overline{p'p'}/2\gamma\overline{p}$). We will examine the energy exchange at three different levels – volume-averaged, plane-averaged and at individual wavenumbers. We will then proceed to examine the pressure-dilatation to production ratio.

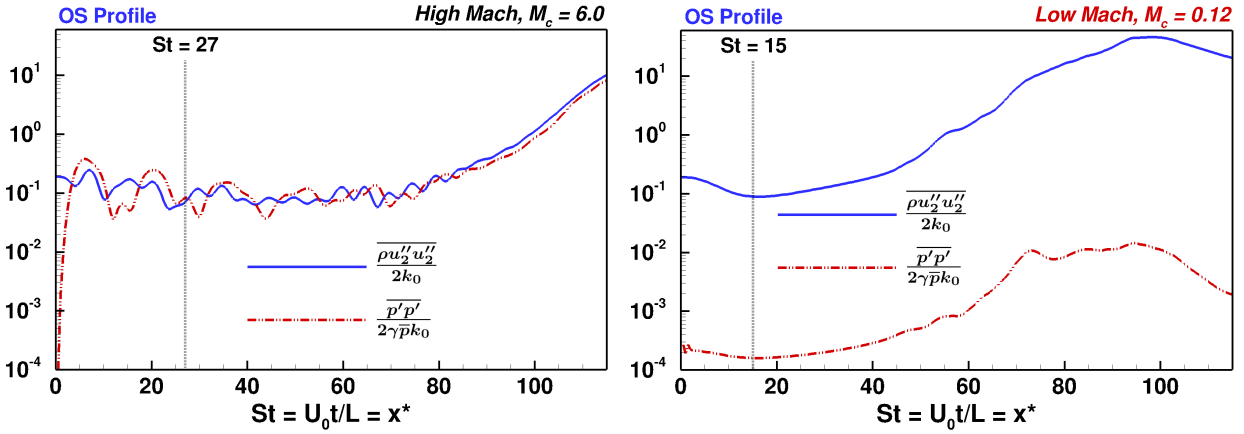

(a) (b)

Figure 4.9: Evolution of volume averaged $\overline{\rho u_2'' u_2''}$ and $\overline{p'p'}/\gamma\overline{p}$ for OS initial profile at (a) high ($M_c = 6.0$) and, (b) low ($M_c = 0.12$) Mach number.

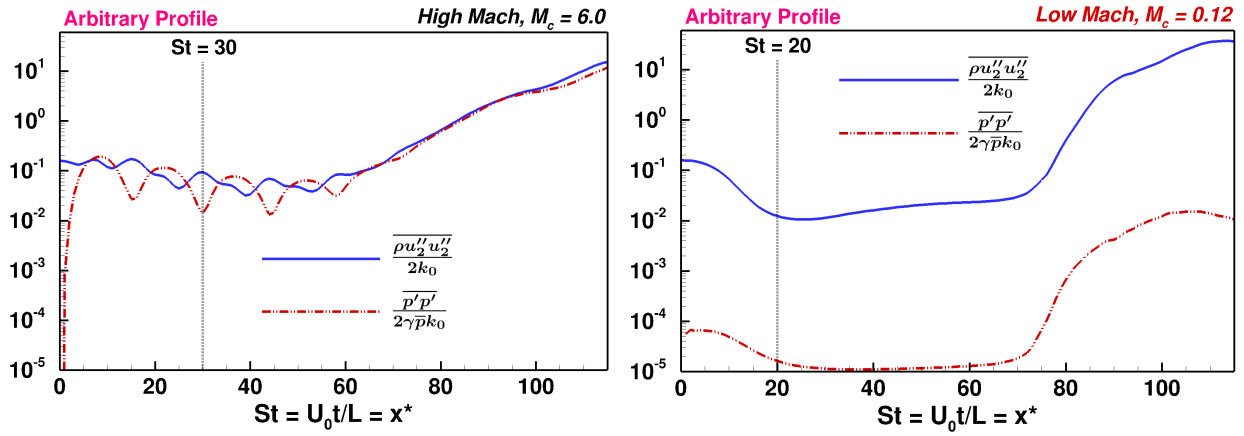

(a) (b)

Figure 4.10: Evolution of volume averaged $\overline{\rho u_2'' u_2''}$ and $\overline{p'p'}/\gamma\overline{p}$ for arbitrary initial profile at (a) high ($M_c = 6.0$) and, (b) low ($M_c = 0.12$) Mach number.

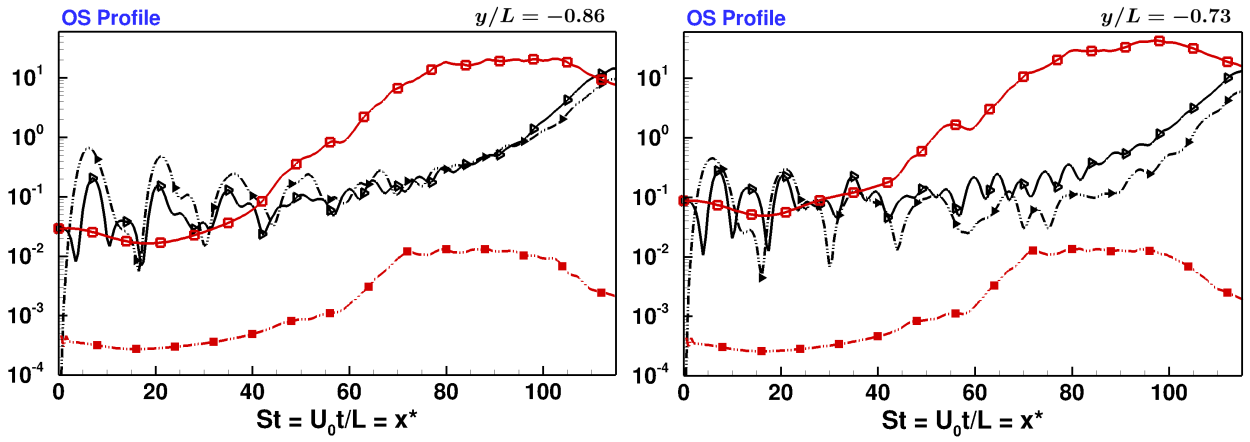

(a) (b)

Figure 4.11: Evolution of plane averaged $\overline{\rho u_2'' u_2''}$ and $\overline{p'p'}/\gamma\overline{p}$ for OS initial profile at (a) near-wall and, (b) intermediate planes. Here, squares represent $M_c = 0.12$ and triangles represent $M_c = 6.0$ cases. Solid lines present evolution of $\overline{\rho u_2'' u_2''}$ while dashed lines are evolution of $\overline{p'p'}/\gamma\overline{p}$.

We first compare the evolution of volume averaged $k_{(2)}$ and $\overline{p'p'}/2\gamma\overline{p}$. In figures 4.9 and 4.10 the evolution of these energy components are compared for the high and low Mach number cases for different initial profiles. As expected the low Mach number simulation shows no exchange between these energies for both initial profiles as the velocity field is exclusively solenoidal in nature. For the high Mach number simulation, $k_{(2)}$ remains nearly at the same order of magnitude as the low Mach number case. However, the energy associated with pressure-variance undergoes a significant change. It exhibits rapid growth initially attaining a value close to that of wall-normal kinetic energy. At subsequent times $k_{(2)}$ and $\overline{p'p'}/2\gamma\overline{p}$ exhibit nearly harmonic oscillations about the same time-averaged value. The results suggest energy equipartition (on an average) between wall-normal velocity fluctuations and pressure fluctuations in the linear and nonlinear regimes. This finding also confirms that the dilatational component of the velocity is almost exclusively in the wall-normal component of velocity. It is important to note that the $w_2 - p'$ interactions lead to equipartition for both the OS and arbitrary initial profiles at high Mach numbers as exhibited in figures 4.9(a) and 4.10(a). It can therefore be inferred that the pressure-dilatation ($\overline{p'd''}$) in both cases acts to impose equipartition of energy between w_2 and p'.

Since the flow is inhomogeneous in the wall-normal direction, we compare the $w_2 - p'$ inter-

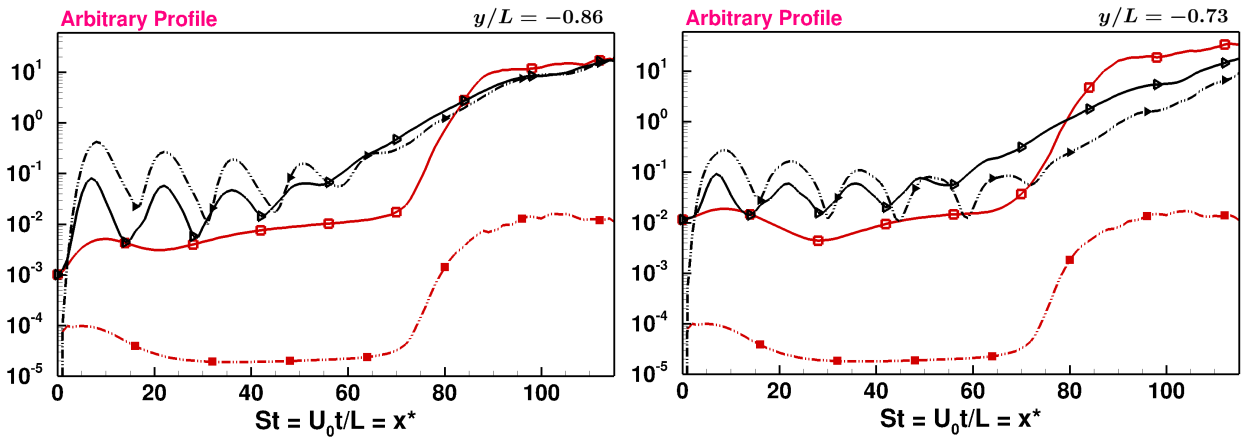

(a) (b)

Figure 4.12: Evolution of plane averaged $\overline{\rho u_2'' u_2''}$ and $\overline{p'p'}/\gamma\overline{p}$ for arbitrary initial profile at (a) near-wall and, (b) intermediate planes. Legend same as figure 4.11.

actions on several $x-z$ planes at different $y-$locations to investigate the degree of equipartition at each plane. In figure 4.11, evolution of $k_{(2)}$ and $\overline{p'p'}/2\gamma\overline{p}$ are compared for high and low Mach cases with the OS initial profile at a near-wall plane, $y/L = -0.86$ and at an intermediate plane, $y/L = -0.73$. At both locations reasonable degree of equipartition is seen in the high Mach case. Similar behavior can be observed for the arbitrary initial profile at the same planes as shown in figure 4.12. Thus, equipartition between $k_{(2)}$ and $\overline{p'p'}/2\gamma\overline{p}$ is achieved not only in the volume averaged statistics but also nearly at each y-plane of the flow (other planes not shown). The level of equipartition between $k_{(2)}$ and $\overline{p'p'}/2\gamma\overline{p}$ is observed to reduce away from the wall. This is because the mean shear (and effective gradient Mach number) decreases away from the wall causing an increase in the solenoidal component of wall-normal fluctuations.

The contrasting behaviour of volume averaged and plane averaged equipartition can be explained by examining eqs. (4.16) and (4.17). When $k_{(2)}$ and $\overline{p'p'}/(2\gamma\overline{p})$ are volume-averaged, the transport term vanishes and the two quantities interact in a harmonic fashion. Thus, the comparison of volume averaged quantities in figures 4.9(a) and 4.10(a) show nearly harmonic (out of phase) evolution. On the other hand, the plan-averaged $k_{(2)}$ and $\overline{p'p'}/(2\gamma\overline{p})$ exchange also involves turbulent transport in the wall normal direction. This transport term can modify the precise harmonic

nature, and yet lead to equipartition. Thus the plane-averaged quantities in figures 4.11(a) and 4.12(a) are not harmonic although the energy levels are nearly equal.

We now investigate $w_2 - p'$ interaction at each wave-vector (κ_x, κ_z) on a given $y-$plane. We examine the evolution of the two-dimensional (2D) spectra of the w_2 and normalized-p' and on the plane at $y/L = -0.73$ in figure 4.13 for Case 1. Contour plots of the 2D $(\kappa_x - \kappa_z)$ spectrum are shown at different times during the evolution. We first consider the exchange in high Mach number case - figure 4.13(a). Initially energy is present only in the w_2-component. In the linear regime, at $St = 10$ the entire energy from the w_2-component is transferred to pressure-variance at the same wavenumbers. However, by $St = 15$, all the energy is transferred back to w_2 into the same initialized wavenumbers. In the nonlinear regime, similar exchange can be seen at $St = 67$ and $St = 75$. Thus the harmonic exchange is observed at each scale in linear and nonlinear regimes. In the nonlinear regime, the residual energy increases nearly monotonically over time as the flow evolves towards breakdown. In the low Mach number counterpart (figure 4.13(b)), the pressure fluctuations are not very energetic throughout the simulation. The wall-normal component of turbulent kinetic energy grows steadily and rapidly cascades to higher wavenumbers.

In summary pressure-dilatation leads to equipartition of dilatational turbulent kinetic energy and pressure-variance at each wavenumber and nearly throughout the flow irrespective of the initial profile of perturbations.

4.3.2.1 Pressure-dilatation to production ratio

We now examine the cause for the difference in the degree of compressibility-initiated effects on OS and arbitrary initial profiles. As suggested in the analysis section, degree of compressibility effects on kinetic energy evolution is governed by the ratio of pressure-dilatation to production. We, therefore, compare the evolution of the plane averaged pressure-dilatation to average production ratio for Cases 1 and 7 in figure 4.14. The results are presented for the two representative planes considered earlier. On both planes, $|\overline{p'd''}/P_k|$ is much higher for Case 1 relative to Case 7 in the early nonlinear regime ($St \in [30, 80]$). In fact, $|\overline{p'd''}/P_k|$ is nearly zero in Case 7 for majority of the early nonlinear regime causing negligible suppression of turbulent kinetic energy. On the other

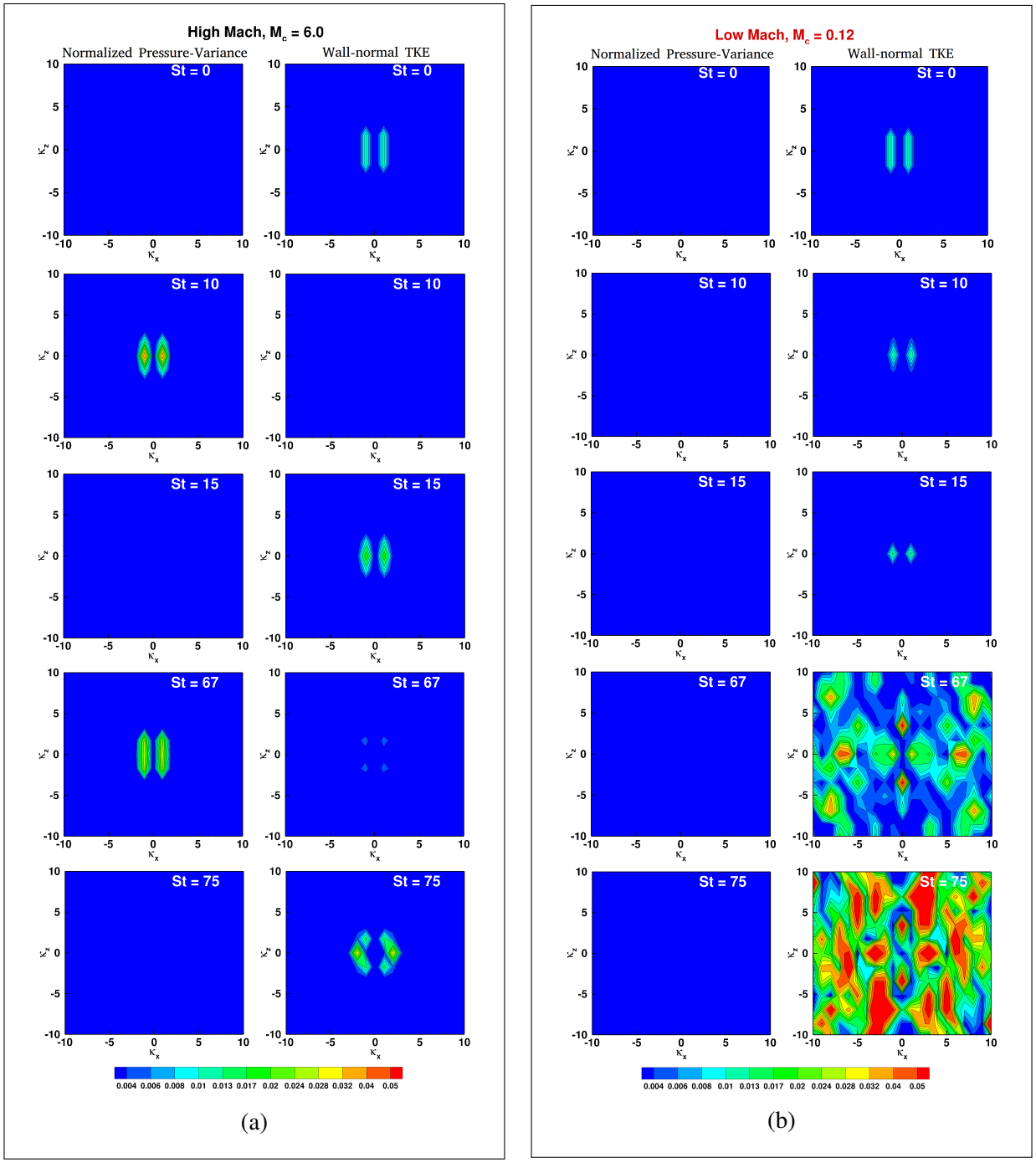

Figure 4.13: Evolution of the 2D spectra of $\overline{p'p'}/\gamma\overline{p}$ and $\overline{\rho u_2'' u_2''}$ for OS (Case 1) initial profile at intermediate plane ($y/L = -0.73$) for (a) high ($M_c = 6.0$) and, (b) low ($M_c = 0.12$) Mach number.

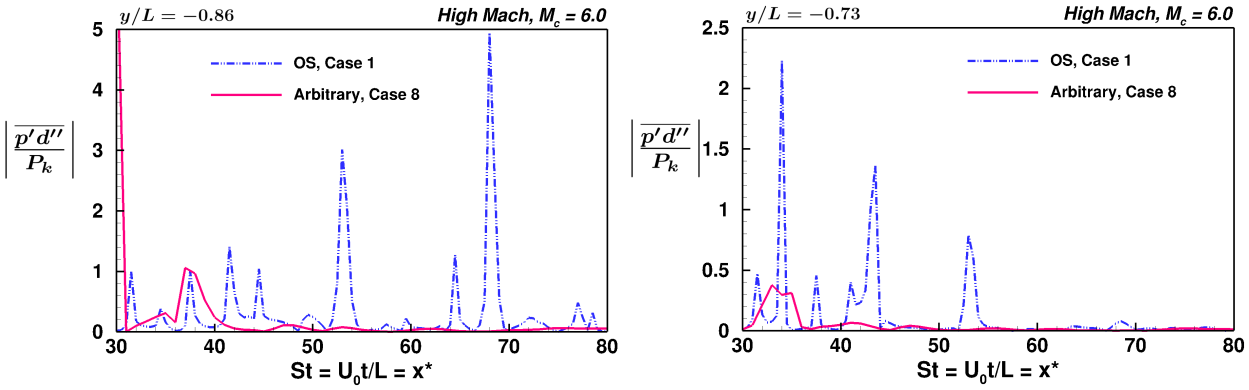

(a) (b)

Figure 4.14: Pressure-dilatation ($\overline{p'd''}$) to production (P_k) ratio for $M_c = 6.0$ initialized with OS and arbitrary initial profiles at (a) near-wall and, (b) intermediate planes.

hand, significant suppression is observed in Case 1 due to much higher magnitude of pressure-dilatation relative to production. This result clearly establishes $|\overline{p'd''}/P_k|$ ratio as the important non-dimensional parameter which governs the degree of k suppression due to compressibility effects. Figure 4.14 also shows that $|\overline{p'd''}/P_k|$ ratio reduces away from the wall for both initial profiles. This behavior can be attributed to the decreasing mean shear in the flow ($S = \partial\overline{U}/\partial y$) away from the wall leading to a low gradient Mach number (refer to eq. (4.8)).

4.3.3 Spectral growth

One of the key objectives of this study is to contrast the spectral energy transfer and the rate of spectral growth in incompressible and compressible flows. We examine the evolution of turbulent kinetic energy spectrum at different $y-$planes. Spectral evolution is presented only on the intermediate plane as other planes show similar behavior. The development of the spectrum in the high and low Mach number cases of each initial profile (Cases 1 and 7) is contrasted at different instances of shear time ($St = 0,\ 15,\ 50,\ 80$). The initial shear time instances are shown to establish that almost equal energy is present in initialized wavenumbers for high and low Mach cases.

In figure 4.15, we consider the evolution of energy content in various scales of motion (κ) at the intermediate plane at $y/L = -0.73$ for the OS initial profile (Case 1). As established in §4.3.2.1, the pressure-dilatation to production ratio is relatively high for this case signifying a high degree

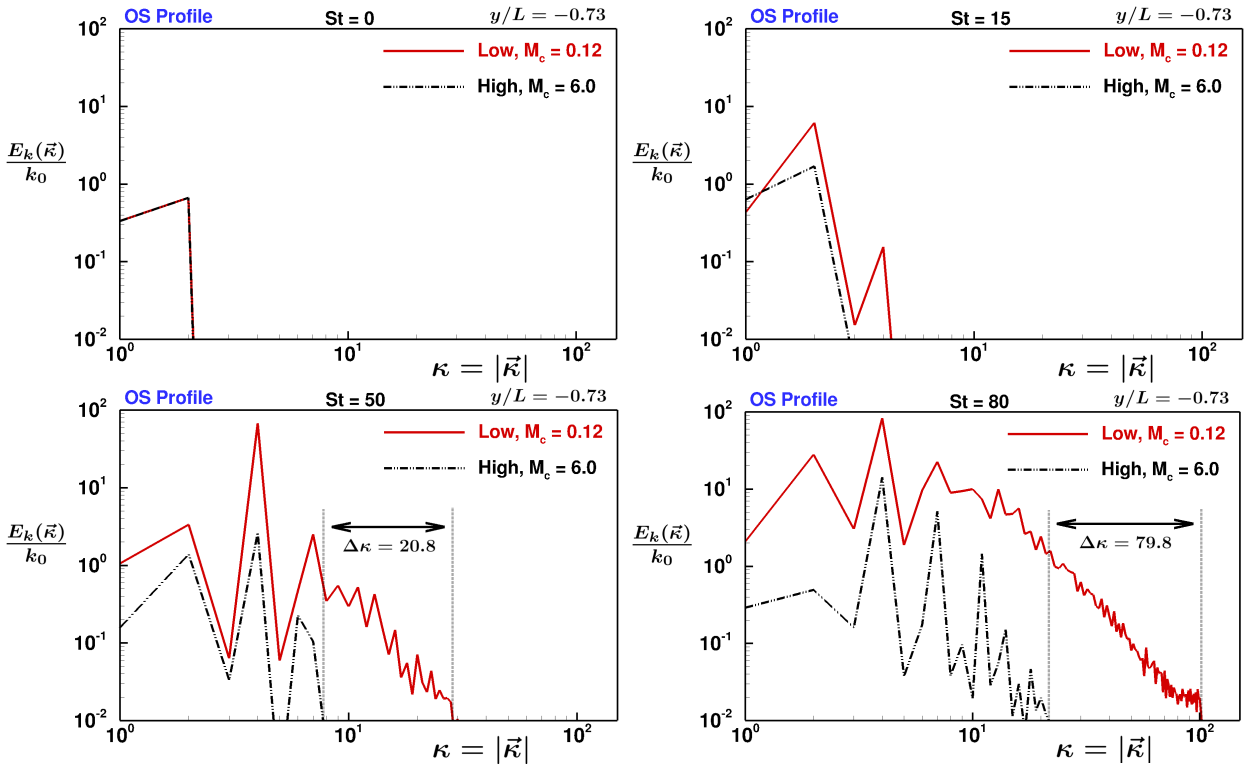

Figure 4.15: Evolution of turbulent kinetic energy line spectra for high and low Mach number with OS initial profile at intermediate plane.

of suppression due to compressibility. The figure shows that the formation of secondary scales of motion is clearly inhibited in the high Mach case relative to the low Mach counterpart. For the high Mach case, the energy in all wavenumbers remains significantly low with many higher wavenumbers completely suppressed. We propose $E(\kappa)/k_0 \sim 10^{-2}$ as the threshold value for determining the emergence of secondary scales of motion. At $St = 50$, the difference in the number of energized scales between the high and low Mach cases is about $\Delta\kappa \approx 21$ which increases to $\Delta\kappa \approx 80$ at $St = 80$. Therefore, the number of suppressed scales between the two Mach cases increases with time. This behavior delays the formation of fully developed spectrum and breakdown toward turbulence in compressible flows.

In figure 4.16, we examine the spectral evolution for the arbitrary initial profile (Case 7). Recall that Case 7 experiences much lower pressure-dilatation compared to production. The low degree of compressibility effect is evident in the development of the turbulent kinetic energy spectrum as

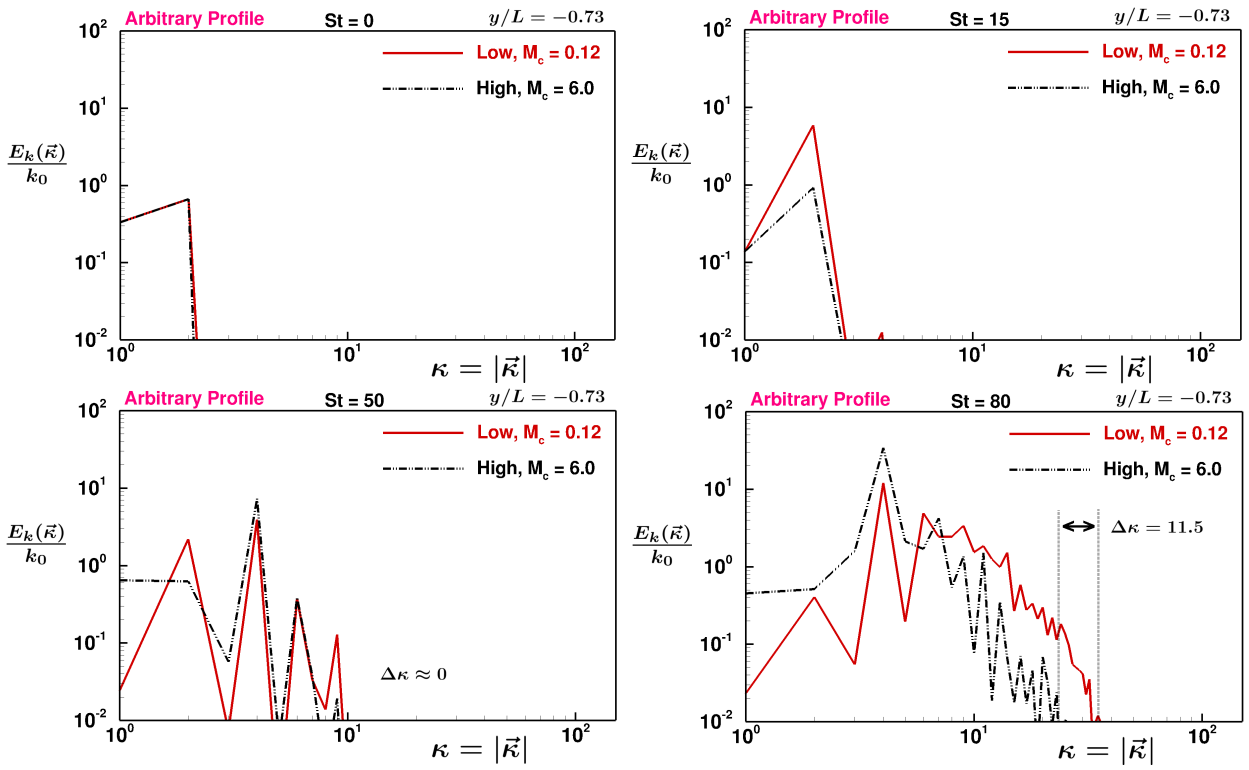

Figure 4.16: Evolution of turbulent kinetic energy line spectra for high and low Mach number with arbitrary initial profile at intermediate plane.

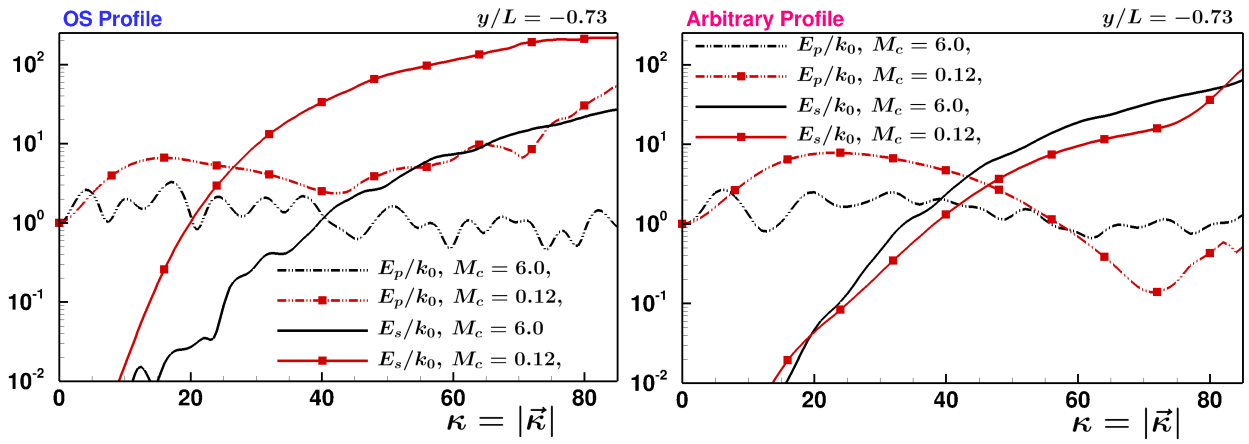

(a) (b)

Figure 4.17: Turbulent kinetic energy evolution for initialized and newly generated modes in high and low Mach number simulations for (a) OS and, (b) arbitrary initial profiles.

well - figure 4.16. At $St = 50$, no differences in the energized scales is observed for the high and low Mach number cases. At $St = 80$ also only marginal differences in the spectrum can be observed with the number of suppressed scales of about $\Delta\kappa \approx 12$.

In summary, high degree of compressibility suppression, characterized by the $|\overline{p'd''}/P_k|$ ratio, leads to an extended transition regime and can potentially delay the breakdown toward turbulence. On the other hand, very little compressibility effect on kinetic energy and spectral growth is observed when the ratio is small.

The spectral plots above show the effect of compressibility on the spectral transfer of turbulent kinetic energy at few instances in time. To completely establish the suppression effect at all times we compare the evolution of energy in initialized wavenumbers or primary modes (E_p) and the energy in newly generated wavenumbers or secondary modes (E_s) in the intermediate plane for both initial profiles. E_p and E_s are defined as,

$$E_p = \sum_{\kappa\in[1,2]} E(\kappa) \quad \text{and} \quad E_s = \sum_{\kappa\geq 3} E(\kappa). \tag{4.25}$$

Figure 4.17(a) compares the evolution of normalized energy in primary modes (E_p/k_0) and that in

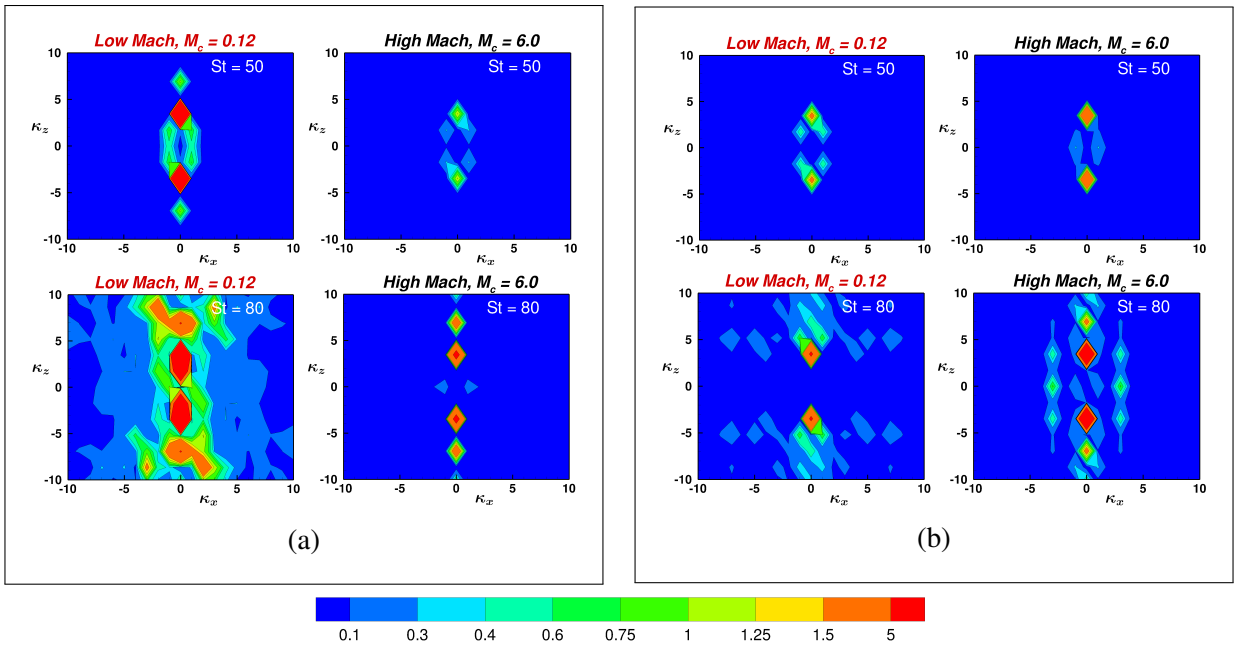

Figure 4.18: Turbulent kinetic energy spectral spread comparison at intermediate plane ($y/L = -0.73$) for (a) OS and, (b) arbitrary initial profiles.

secondary modes (E_s/k_0) for the high and low Mach simulations of Case 1. The figure shows that the energy in the secondary scales (E_s) remains significantly low in the high Mach case relative to the equivalent low Mach case throughout the early nonlinear regime. The evolution of E_p is oscillatory and does not grow from its initial value. This is because the initialized modes are low wavenumbers ($\kappa \in [1, 2]$) which experience the highest effective gradient Mach number (M_g^e). Eq. (4.7) shows that the effective gradient Mach number M_g^e is inversely proportional to κ causing high suppression due to compressibility of low wavenumbers. Contrary to Case 1, the evolution of E_s for the high and low Mach cases of Case 7 is not very different - figure 4.17(b). As expected, no suppression in the magnitude and growth rate of energy in secondary modes is observed throughout the early nonlinear regime. Although, the evolution of E_p in Case 7 is similar to that in Case 1 for the high Mach case, the energy suppression in these scales relative to the low Mach case is small. The nonlinear processes in the low Mach simulation for Case 7 do not produce energy in the low wavenumbers leading to no observable compressibility effects in the high Mach simulation of this case.

4.3.3.1 Effect of wave-vector obliqueness

The effect of compressibility on each mode is governed by wavenumber magnitude (κ) and the obliqueness angle (β) of the mode as characterized by M_g^e defined in eq. (4.7). To establish the effect of obliqueness angle we compare the 2D spectrum for turbulent kinetic energy in the intermediate plane in figure 4.18 for both initial profiles. The low speed Case 1 simulation shows a high level of energy in streamwise modes at $St = 50$ which is absent in the high speed counterpart since these modes experience highest M_g^e and are suppressed (figure 4.18(a)). At $St = 80$, the large difference in the spectral spread of high and low Mach cases is visible with only the spanwise modes energized in the high Mach case. The effective Mach number M_g^e experienced by these modes is zero and therefore, these modes are not suppressed (preserving the lift-up mechanism). For Case 7, we observe that streamwise modes are less dominant in the low Mach number case (figure 4.18(b)). The nonlinear processes in both Mach number simulations of Case 7 develop most energy in the spanwise modes causing no difference in the spectral distribution. At $St = 80$, significant energy can be seen in few streamwise modes for the high Mach case. Although the obliqueness of these modes is low, the wavenumber is high leading to a small effective gradient Mach number.

4.3.4 Mack mode

The objective of this subsection is to perform a quantitative comparison of kinetic energy spectral evolution between low and high Mach number cases. The comparison of OS mode evolution at low and high Mach numbers (shown earlier) presents useful insight. However, that comparison does not account for the fact that OS mode is not the most unstable perturbation at high speeds. We propose that a meaningful comparison should examine the evolution of most unstable mode specific to each Mach number. Therefore, in this subsection, we will compare and contrast the spectral evolution of the perturbation field initialized with OS mode for low Mach number and the Mack mode for high Mach number. The most unstable Mack mode is determined from linear stability theory as explained in chapter 3. In each simulation, a triad (one streamwise and two oblique) of

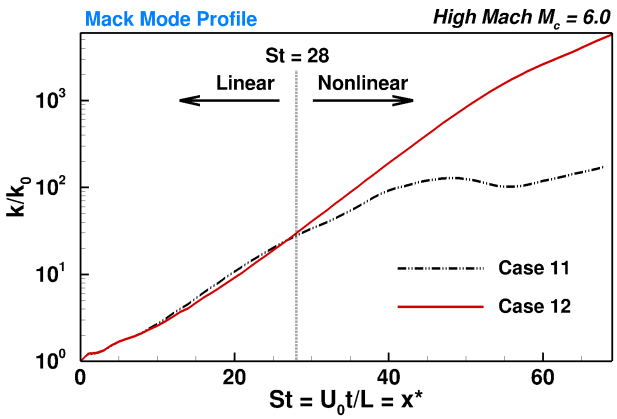

Figure 4.19: Volume averaged turbulent kinetic energy evolution for different perturbation intensities with Mack mode profile. Initial perturbations with $\beta = 0°, \pm 60°$ are equally energized.

the appropriate perturbation modes are superposed on the background field at the initial time – see table 4.2. Then the evolution of various flow quantities are examined.

As in previous subsections, we first examine the kinetic energy evolution in the two high Mach number simulations (Cases 11 and 12) in Figure 4.19. The kinetic energy of the higher initial perturbation intensity simulation (Case 11) deviates from that of the lower perturbation intensity case at about $St \sim 28$. Recall that the onset of nonlinearity of the low Mach number case with OS initial profile (Case 1) happens around $St \sim 15$ (figure 4.5b). This reiterates that compressibility leads to an extended linear regime. Interestingly, upon the onset of nonlinearity, the growth rate of turbulent kinetic energy of the initial high intensity simulation (Case 11) is lower than that of the low intensity case (Case 12). This suggests that the new scales of motion produced by nonlinear spectral transfer may be more stable than the initial Mack mode.

We also investigate the volume-averaged wall-normal component of turbulent kinetic energy ($k_{(2)}$) and the normalized pressure variance ($\overline{p'p'}/2\gamma\overline{p}$) for Case 11. Figure 4.20 shows the two energies to be nearly equal. This reaffirms the fact that pressure-dilatation continues to enforce energy equipartition.

As previously established, pressure-dilatation to production ratio is a key feature that influences spectral evolution in compressible turbulence. As we expect the compressibility effect to depend on

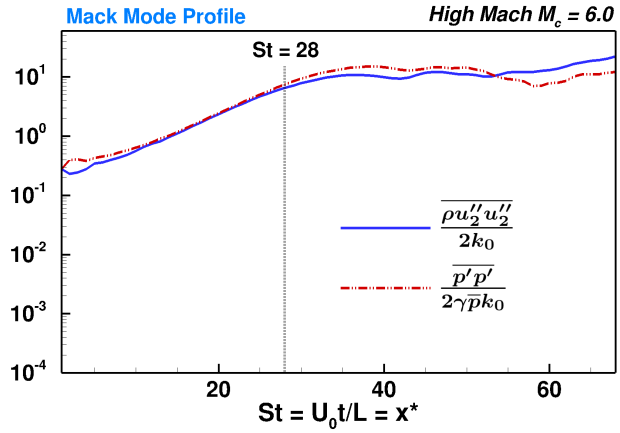

Figure 4.20: Evolution of volume averaged $\overline{\rho u_2'' u_2''}$ and $\overline{p'p'}/\gamma\overline{p}$ for Mack mode profile.

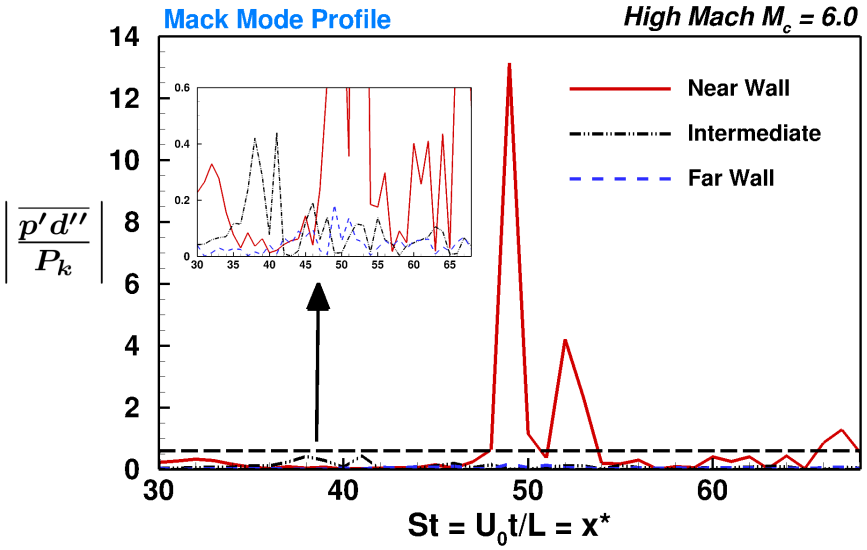

Figure 4.21: Comparison of pressure-dilatation ($\overline{p'd''}$) to production (P_k) ratio at different $y-$planes for $M_c = 6.0$ initialized with Mack mode profile.

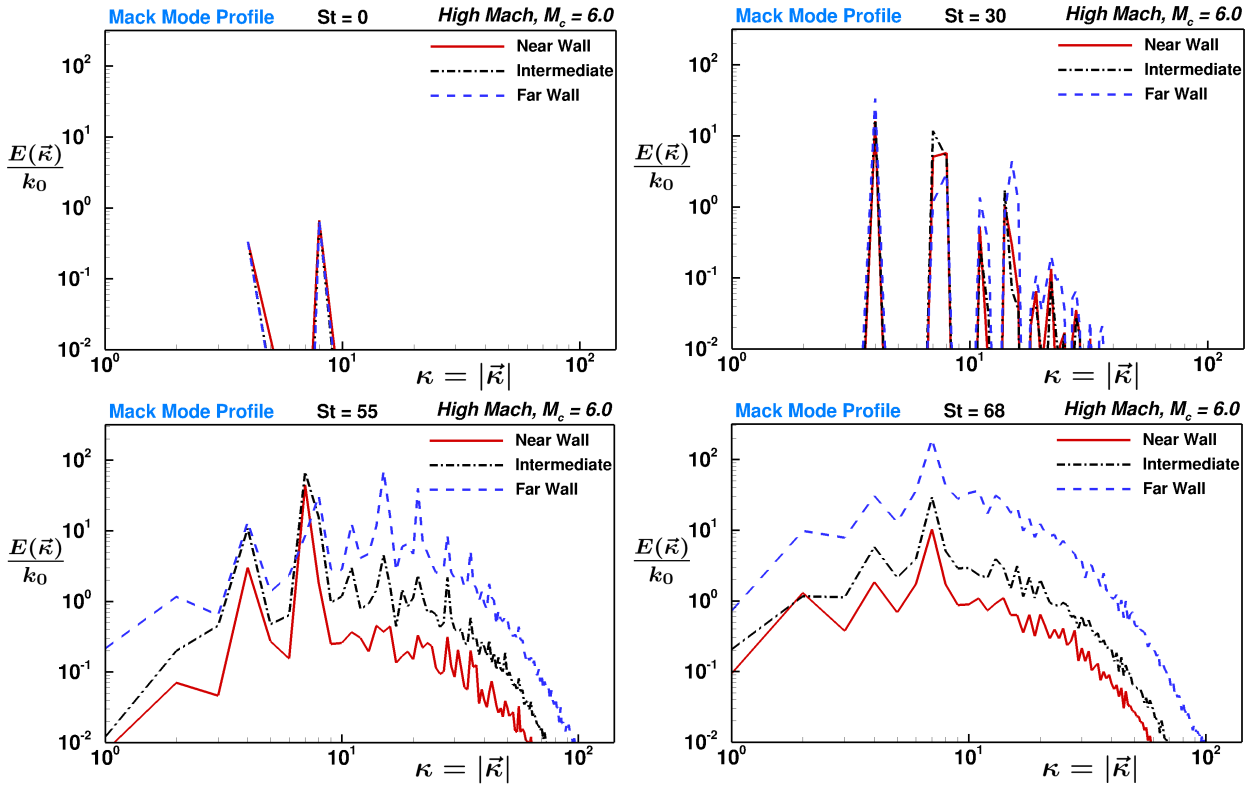

Figure 4.22: Evolution of turbulent kinetic energy line spectra for high Mach number flow initialized with Mack mode profile at near-wall ($y/L = -0.86$), intermediate ($y/L = -0.73$) and far-wall ($y/L = -0.5$) planes.

distance from the wall, we examine pressure-dilatation levels at different wall-normal planes. The three planes considered are - near wall plane ($y/L = -0.86$), intermediate plane ($y/L = -0.73$) and a far-wall plane ($y/L = -0.5$). Figure 4.21 shows the temporal evolution of $|\overline{p'd''}/P_k|$ at each of these planes. It can be inferred from the figure that (i) the near wall plane experiences the highest levels of $|\overline{p'd''}/P_k|$ ratio and (ii) the relative importance of pressure-dilatation decreases with increasing wall distance. The near and intermediate locations experience moderate levels of dilatation effects within $St \in [30, 48]$ and at later times ($St > 48$), the near-wall plane experiences very high levels of pressure-dilatation.

We now proceed to compare the spectral evolution at different wall-normal distances in high (Case 11) and low (Case 1) Mach number Poiseuille flows. It must be noted that the wavenumber values and mode profiles are very different for the two cases. The normalized (by streamwise

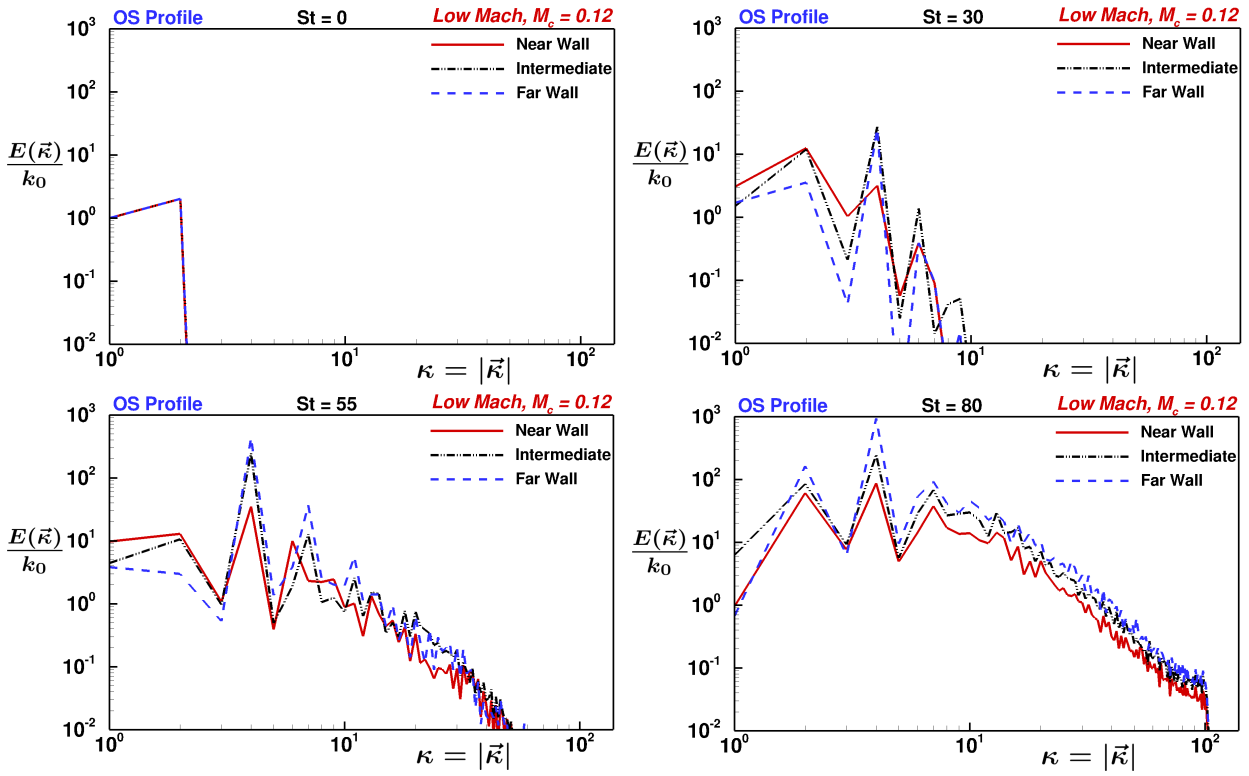

Figure 4.23: Evolution of turbulent kinetic energy line spectra for low Mach number flow initialized with OS profile at near-wall ($y/L = -0.86$), intermediate ($y/L = -0.73$) and far-wall ($y/L = -0.5$) planes.

length, L_x) wavenumber of the most unstable mode is unity at low Mach number and four at high Mach number. The wavenumbers associated with the oblique modes are a little higher than the streamwise ones due to the nature of initialization. Figures 4.22 and 4.23 compare the spectral evolution of high and low Mach number cases at different times. The initial spectra at all wall-normal distances are identical. For the low Mach number case with OS initial profile (figure 4.23) the spectra continue to be nearly identical for all three planes throughout the period of time considered. The high Mach number Poiseuille flow presents a completely different scenario (figure 4.22). The spectra on the three planes are reasonably similar until about $St \sim 50$. At later stages, however, vast differences in the spectra are evident. The differences between the spectra arise at about the time when the pressure-dilatation to production ratio grows to large values. The near-wall plane, with the highest values of $|\overline{p'd''}/P_k|$, clearly exhibits the least amount of kinetic energy and the narrowest spectrum. The kinetic energy level and spectral width of the intermediate plane are both larger than than those of near-wall plane. As was shown earlier, the intermediate plane experiences moderate levels of pressure-dilatation. The far-wall plane, with little or no pressure-dilatation, exhibits the largest value of kinetic energy and the widest spectrum. These findings clearly imply that in high-speed Poiseuille flow, the nonlinear effects are onset at different rates at different wall-normal locations. Specifically, the spectral growth is slowest near the wall and is progressively faster away from the wall. On the contrary, the onset nonlinear processes are reasonably independent of wall-normal distance at low speeds.

4.4 Conclusions

Compressibility profoundly affects the nonlinear evolution of the perturbation field in high Mach number flows. Emergence of dilatational fluctuations leads to the onset of kinetic–internal energy exchange via pressure-dilatation mechanism. This study contrasts the nonlinear stages of turbulent kinetic energy growth, flow-thermodynamic interactions and spectral growth in compressible and incompressible wall-bounded shear flows. The key inferences from this study are summarized below.

1. The wall-normal component of the perturbation field is shown to be dominantly dilatational

in nature. The turbulent kinetic energy of wall-normal fluctuations is nearly equipartitioned with normalized pressure-variance in the linear and nonlinear regimes in the overall flow field (volume-averaged sense), at each $y-$plane and even at each wavenumber. In high speed flows, equipartition is achieved regardless of the initial profile of perturbations.

2. Pressure-dilatation to production ($|\overline{p'd''}/P_k|$) ratio is identified as the important non-dimensional parameter which characterizes the degree of compressibility effects on turbulent kinetic energy evolution.

3. When $|\overline{p'd''}| > |P_k|$:

   (a) The growth rate of turbulent kinetic energy is highly suppressed relative to a similar low Mach case.

   (b) The spectral transfer rate is significantly reduced leading to slow down in spectrum growth at high speeds.

4. When $|\overline{p'd''}| < |P_k|$, effect of compressibility on turbulent kinetic energy growth and spectral transfer of energy remains insignificant. The flow field evolves similar to a comparable low speed flow.

The above inferences are important for understanding and modeling the laminar-turbulent boundary layer transition process for high-speed flows. The slowdown in spectral energy transfer may cause an extended linear and nonlinear phase of the perturbation field evolution. The rate of spectral growth can also be reduced and breakdown to turbulence maybe delayed for compressible flows.

5. PARAMETERIZATION OF NONLINEAR EFFECTS OF COMPRESSIBILITY

The most widely used transition prediction tool is the e^N method or the linear $N-$factor approach. In this approach, linearized equations are used to calculate growth rates of all perturbation modes. Transition is estimated to be the earliest location where the growth rate becomes greater than e^N where N is the amplification factor and is determined empirically. Although this approach is fairly reasonable in predicting the laminar-turbulent transition for low Mach number boundary layer flows, it fails for hypersonic flows. In the previous chapter, we have established that dominant compressibility effects lead to oscillatory growth of turbulent kinetic energy and also causes significant reduction in the rate of spectral transfer of energy. The delay in the formation of secondary scales of motion shifts the location of the laminar-turbulent boundary layer transition further downstream. Dominant compressibility effects can also lead to an extension of the transition regime causing a delay in formation of a full spectrum or breakdown towards turbulence even after the onset of transition. The $N-$factor approach of transition prediction fails in accounting for these mechanisms, therefore, there is a need to develop physics based prediction models.

The focus of this chapter is on the parameters that correlate to the degree of compressibility and therefore affect the degree of suppression due to compressibility in the nonlinear regime. In the previous chapter, we have identified pressure-dilatation to be one of the key mechanisms for enforcing compressibility effects on different flow processes. It is also shown that the degree of compressibility effects on turbulent kinetic energy evolution can be characterized using pressure-dilatation to production ratio ($\overline{p'd''}/P_k$). Modeling pressure-dilatation can be challenging, hence the objective of this chapter is to identify important parameters that correlate to $\overline{p'd''}/P_k$ ratio. We utilize the concepts of componentality and dimensionality as put forward by Kassinos et al. [2001] along with the previously gained insight of compressibility effects to identify these parameters. Toward that end we undertake the following tasks:

1. Identify important componentality and dimensionality components based on previously gained

insight of compressible flows.

2. Establish the relevance of these parameters through DNS results.

The chapter is organized as follows. A brief discussion of the important parameters which influence compressibility effects is presented in §5.1. Verification of the identified parameters using the DNS results is presented in §5.2 along with a concise summary in §5.3.

5.1 Important parameters characterizing compressibility effects

The linear regime analysis performed by Xie et al. [2017] for perturbation development in a compressible Poiseuille flow provides important insights into the level of compressibility effects on different components and modes in the flow. These inferences are shown to be relevant in the early nonlinear regime as well in the previous chapter. It is also shown that compressibility effects vary depending on the component or the mode of turbulent kinetic energy. Quantifying the compressibility effects can be difficult in the nonlinear regime due to the production of various modes via the nonlinear interactions. Therefore, we utilize the concept of componentality and dimensionality as developed by Kassinos et al. [2001]. Componentality is generally defined as the relative strength of different velocity components while dimensionality is the relative uniformity of structure in different directions. Although these structure functions were first utilized in improving our understanding of the dynamics of turbulence evolution, behavior of these quantities can be important in the early nonlinear stages of perturbation development as well. We now discuss the componentality and dimensionality concepts individually in relation to the previously developed inferences for perturbation development in compressible Poiseuille flows.

5.1.1 Componentality

As mentioned before, componentality is the relative strength of different velocity components in the flow field. Most common parameters used to study componentality in the flow is the normalized Reynolds stresses (r_{ij}) defined as:

$$r_{ij} = \frac{\overline{\rho u_i'' u_j''}}{\overline{\rho u_k'' u_k''}} = \frac{\overline{\rho u_i'' u_j''}}{2k}, \tag{5.1}$$

where k is the instantaneous volume averaged turbulent kinetic energy. A higher order measure for the preferred velocity component can be defined as:

$$C_{ij} = \overline{\left[\frac{\partial u_i''}{\partial x_k}\frac{\partial u_j''}{\partial x_k}\right]}. \tag{5.2}$$

Using the above measure, the componentality (c_{ij}) of the flow is described as:

$$c_{ij} = \frac{C_{ij}}{C_{rr}}. \tag{5.3}$$

In previous studies of shear flows, the wall-normal component of velocity perturbations (u_2'') is shown to be most dilatational in nature (Livescu and Madnia [2004] and Xie et al. [2017]). In Poiseuille flow, linear analysis performed by Xie et al. [2017] shows equipartition of energy within wall-normal turbulent kinetic energy ($k_{(2)}$) and pressure-variance ($\overline{p'p'}/\gamma\overline{p}$) which is a measure of turbulent internal energy (Mittal and Girimaji [2019]). In the last chapter, we established that equipartition exists within these energy forms even in the early nonlinear stage. Since equipartition is a consequence of compressibility in the flow, the wall-normal component plays an important role in compressible flow dynamics. Therefore, the important componentality measures for characterizing compressibility effects are the wall-normal normalized Reynolds stress and the wall-normal componentality which are defined as:

$$r_{22} = \frac{\overline{\rho u_2'' u_2''}}{2k} \quad \text{and} \quad c_{22} = \frac{C_{22}}{C_{rr}}. \tag{5.4}$$

A relatively high level magnitude of the wall normal componentality would indicate higher energy in the u_2'' component of velocity fluctuations. Since u_2'' is the most dilatational in nature, a higher energy in these fluctuations which cause higher velocity-pressure interactions due to pressure-dilatation.

5.1.2 Dimensionality

Dimensionality is a measure of the relative directional preference of velocity fluctuations. In wavenumber space, dimensionality can provide insight into the dominant mode directions such as streamwise (κ_x) or spanwise (κ_z). Similar to the higher order measure for the preferred velocity component, a measure for directional mode preference can be defined as:

$$D_{ij} = \overline{\frac{\partial u_k''}{\partial x_i}\frac{\partial u_k''}{\partial x_j}}. \tag{5.5}$$

Using this measure, the dimensionality in the flow becomes:

$$d_{ij} = \frac{D_{ij}}{D_{rr}}. \tag{5.6}$$

The linear analysis performed by Xie et al. [2017] establishes the effect of mode obliqueness on compressibility suppression. It is observed that streamwise modes are most affected by compressibility and therefore, most stabilized. On the other hand spanwise modes are unaffected. The compressibility effects are shown to reduce as the obliqueness angle (β) increases. An effective gradient Mach number, M_g^e (defined in eq. 4.7), is introduced which characterizes the degree of suppression due to compressibility effects. Due to the presence of only initialized modes in the linear regime, it is simpler to characterize the effect using the obliqueness angle (β). However, onset of nonlinearity leads to transfer of energy to small scales of motion and formation of new scales in the flow. As we know that streamwise component is most stabilized by compressibility, the streamwise dimensionality can be an important parameter for analysis in the nonlinear regime. The streamwise dimensionality or d_{11} is defined as:

$$d_{11} = \frac{D_{11}}{D_{rr}}, \tag{5.7}$$

and it describes the relative average distribution of energy in the streamwise component of all modes. Higher energy in streamwise components would increase the stabilization effect of com-

pressibility. Dimensionality as defined here does not include the effect of wavenumber but just the wavenumber orientation. A high streamwise wavenumber would show higher d_{11} although the effect of compressibility would be small due to low M_g^e because of high wavenumber.

The wall-normal componentality and streamwise dimensionality defined above are studied to characterize the effect of compressibility in the nonlinear regime. These components incorporate key linear regime mechanisms that occur in high speed flows in contrast to low speed flows. We now proceed to show the relevance of these parameters using DNS results for same cases considered in chapter 4.

5.2 Results

In the previous chapter, we examined the effect of compressibility for cases with many initial profiles namely: OS, arbitrary, combined and Mack mode (table 4.2). Similar to the previous chapter we will perform direct comparisons of these component for low and high Mach number flows. Due to this direct comparison, both high and low Mach simulations need to be initialized the same. Therefore, only OS (Case 1) and arbitrary profile (Case 7) cases are considered in this chapter. Now we examine the evolution of the above discussed parameters for these two profiles. Since the focus is on the evolution in the nonlinear regime, results are compared only for $St \in [30, 80]$ which is the nonlinear regime in both cases. The OS initial profile shows much higher suppression due to compressibility compared to the arbitrary profile. Similar behaviour was observed in pressure-dilatation to production ratio as well.

5.2.1 Componentality

It is established that equipartition of energy between ($k_{(2)}$) and pressure-variance is achieved as a consequence of compressibility regardless of the initial profile. The wall-normal componentality, which captures the level of equipartition, is an important parameter towards characterizing the effect of compressibility in the nonlinear regime. We will first compare the volume averaged normalized wall-normal Reynolds stress (r_{22}) for the arbitrary and OS initial profiles at both Mach numbers in figure 5.1. The figure shows comparable levels of r_{22} for OS and arbitrary profiles

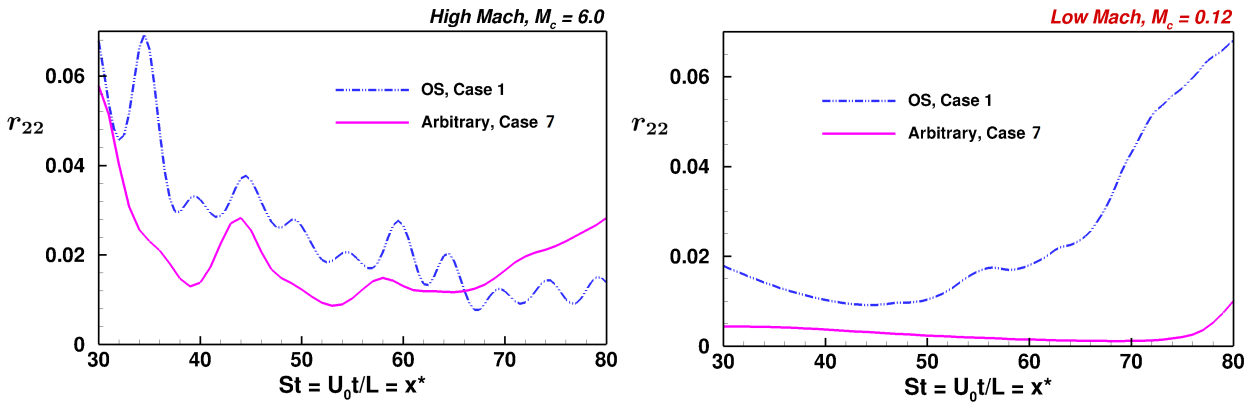

(a) (b)

Figure 5.1: Comparison of normalized wall-normal Reynolds stress (r_{22}) at (a) $M_c = 6.0$ and (b) $M_c = 0.12$ for OS and arbitrary initial profiles.

in the high Mach case emphasizing equipartition for both cases. However, comparison of r_{22} for low Mach case clearly shows much higher levels of r_{22} for the OS profile compared to Arbitrary. This further establishes that volume averaged r_{22} directly correlates to compressibility effects in nonlinear regime.

We now compare the wall normal componentality, c_{22} for the two cases. The figure 5.2 shows similar behavior as r_{22}. Comparing the trends in r_{22} and c_{22}, it is observed that c_{22} is more robust for characterizing compressibility effects. The wall-normal componentality (c_{22}) is almost overlapping for the two cases in the early nonlinear regime for the high Mach case while distinctly different behavior can be observed for the two cases in the low Mach case. From these results, it can be established that equipartition of energy between pressure-variance and wall-normal turbulent kinetic energy restricts the growth of the wall-normal component of velocity fluctuations to a certain level. The level of wall-normal componentality remains independent of the initial profile. Therefore, a low Mach simulation with higher c_{22} would incur higher compressibility suppression in the equivalent high Mach simulation.

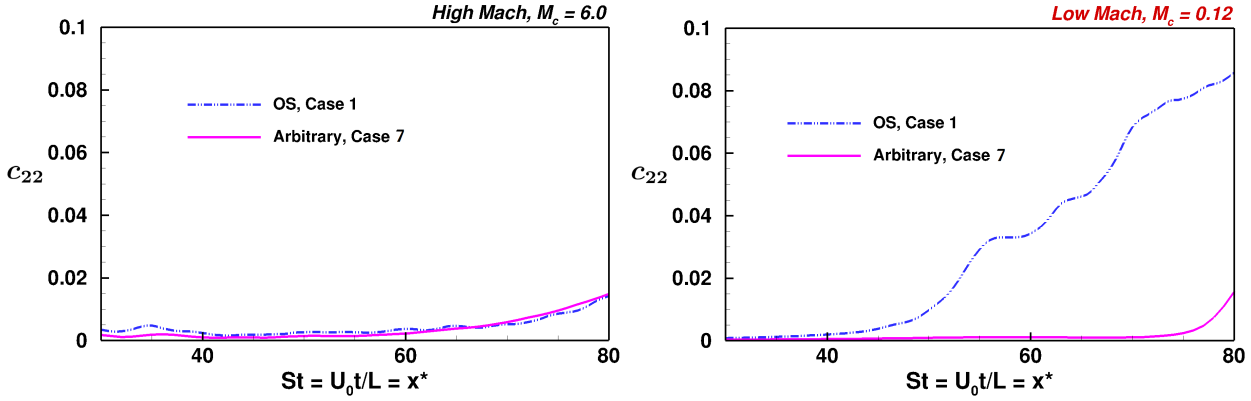

(a) (b)

Figure 5.2: Comparison of wall-normal componentality (c_{22}) at (a) $M_c = 6.0$ and (b) $M_c = 0.12$ for OS and arbitrary initial profiles.

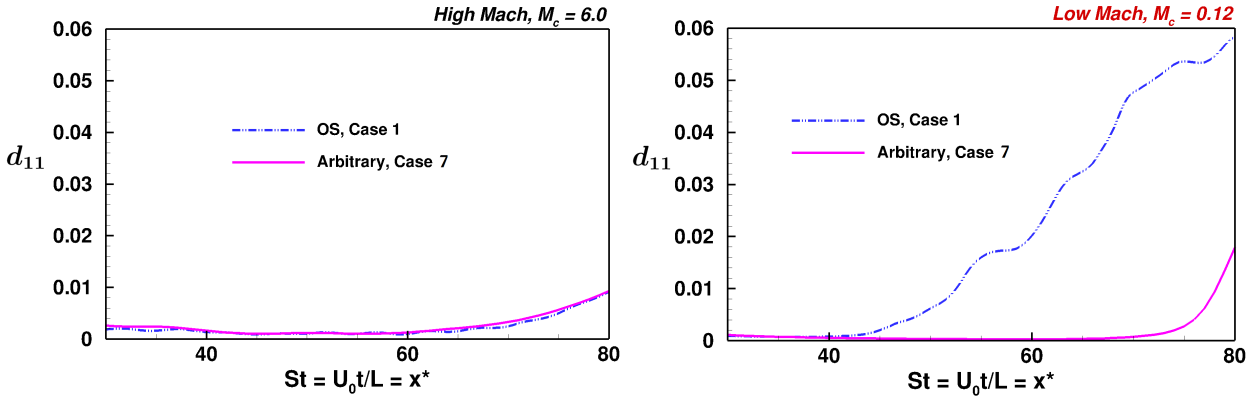

(a) (b)

Figure 5.3: Comparison of streamwise dimensionality (d_{11}) at (a) $M_c = 6.0$ and (b) $M_c = 0.12$ for OS and arbitrary initial profiles.

5.2.2 Dimensionality

Similar to componentality, we now compare the volume averaged streamwise dimensionality, d_{11} for the two cases. The figure 5.3 shows that streamwise dimensionality is also restricted in compressible simulations and the level of dimensionality is similar regardless the initial profile. Observing the evolution trends in the low Mach case reveals if dominant compressibility suppression will be observed. Recall that the low Mach OS profile initial condition case developed high energy in low wavenumber streamwise modes leading to a high d_{11} compared to negligible d_{11} in the equivalent arbitrary case. These modes are stabilized when compressibility is acting, thereby restricting the streamwise modes and reducing d_{11} for high Mach cases. Since the arbitrary profile does not produce many streamwise modes, the low Mach case d_{11} is low causing negligible compressibility suppression in the equivalent high Mach case.

5.3 Conclusions

In this chapter we have discussed key factors which relate to pressure-dilatation to production ratio and thereby, characterize the effect of compressibility in the nonlinear regime. The specific componentality and dimensionality factors are identified using the inferences developed in the linear regime for compressibility effects. Equipartition among wall normal fluctuations and pressure field is the main result of internal-kinetic energy exchange due to pressure-dilatation. Also the effect of compressibility varies with the level of obliqueness of perturbations. The suppression effect is identified to reduce as the obliqueness increases causing streamwise perturbations to be most suppressed. Considering these factors, wall normal componentality and streamwise dimensionality are identified as the relevant parameters. Both parameters are shown to affect the pressure-dilatation to production ratio which characterizes the effect of compressibility in the nonlinear regime. These parameters can be insightful in the future works aiming at modeling hypersonic flow evolution.

6. SUMMARY AND DISCUSSION

Compressibility affects all stages of perturbation evolution in high Mach number flows due to the fundamental change in the nature of pressure leading to emergence of dilatational component of the velocity field. Unlike incompressible flow, the pressure field in high-speed compressible flow is completely determined by the state equation. These changes lead to two important effects: (i) modification of the linear stability characteristics of the flow field; and (ii) onset of kinetic–internal energy exchange via the pressure-dilatation mechanism. High speed compressible flows have been reasonably studied in literature with major focus in the linear and fully developed turbulence regimes. Examination of the nonlinear stages of transitioning hypersonic flows are much less investigated. Specifically, the effect of compressibility the key nonlinear cascade process is not well understood. In this thesis, we address the important issues pertaining to simulation and understanding of hypersonic flows simulations in the nonlinear regime.

In the first study, we establish a framework for examining internal energy of compressible flow in a manner similar to kinetic energy analysis. A suitable thermodynamic variable, proportional to density-weighted acoustic speed $\phi \sim \sqrt{p}$, is identified for internal energy. This allows for partitioning of the total internal energy into the mean field and perturbation field contributions. The spectral behavior of turbulent internal energy can also be examined using the newly defined variable. The developed framework includes governing equations for mean field and perturbation field energy contributions and key energy interactions are identified among all internal and kinetic energy components.

In the second study, a through validation of the gas kinetic method (GKM), based on kinetic theory, is performed. The GKM simulation results are compared against compressible linear stability theory (LST) in benchmark wall-bounded Poiseuille flow. A parameter sweep for Mach number in $[2.5, 9.5]$ using LST analysis provides insight into the effect of Mach number on the most unstable modes. For all high speed cases, the low wavenumbers are observed to stabilize affirming the relevance of the gradient Mach number, M_g as an important parameter. Five representative

Mach numbers are chosen for the validation study. It is demonstrated that GKM simulations accurately capture the switch from dominant first mode to Mack mode as a function of Mach number. Two types of initialization are simulated for validation purposes: (i) single mode perturbations and (ii) random inflow pressure fluctuations. For each case the mode, its shape and growth rate are compared with LST. The inferences from this study are:

(i) Single mode simulations establish the ability of GKM to effectively retain the most unstable mode, its shape and growth rate for all Mach numbers considered.

(ii) Random inflow pressure perturbations lead to the following outcomes:

- GKM accurately captures the most unstable mode and its shape after passage of initial transience for all Mach numbers.
- The internal–kinetic interactions are accurately captured in the GKM algorithm as random acoustic perturbations lead to formation of velocity field instabilities.
- The asymptotic growth rate of average turbulent kinetic energy is observed to be reduced compared to most unstable mode in LST due to the presence of multiple instabilities with lower growth rates. Also, nonlinear interactions can lead further reduction in the overall growth rate.

In the third study, we contrast the evolution of turbulent kinetic energy, flow-thermodynamic interactions and spectral growth between compressible and incompressible wall-bounded shear flows for various initial profiles. Two types of contrasts are performed: (i) both Mach number flows initialized with the same perturbation and, (ii) each Mach case initialized with the corresponding most unstable profile calculated using linear stability analysis. The first contrast enables a direct comparison of perturbation development highlighting the effect of compressibility and relevant important parameters. On the other hand, the second provides a more realistic qualitative contrast where the previously identified important parameters can be tested. This study provides the following key inferences:

(i) Wall-normal component of the perturbation field is dominantly dilatational in nature and equipartition of turbulent kinetic energy in wall-normal fluctuations and normalized pressure-variance is observed for all of initial perturbation profiles considered.

(ii) The degree of compressibility effects on turbulent kinetic energy evolution can be characterized by pressure-dilatation to production ($|\overline{p'd''}/P_k|$) ratio. Cases with $|\overline{p'd''} > P_k|$ lead to high degree of suppression of turbulent kinetic energy and spectral energy transfer rate is significantly reduced. Cases with $|\overline{p'd''} < P_k|$ exhibit little or no effect of compressibility.

(iii) $|\overline{p'd''}/P_k|$ is also observed to reduce with wall normal distance reducing the suppression effect of compressibility away from the wall.

The findings of this thesis provide improved insights into the effect of compressibility on the nonlinear evolution of perturbations in a compressible wall-bounded flow. Such understanding is useful for developing physics-based models for laminar to turbulent transition in high speed boundary layers. It is anticipated that the developed framework for internal energy will be important for future analysis and modeling of energy dynamics in high-speed compressible transition and turbulent flows. Also, the slowdown in spectral energy transfer due to significant compressibility effects may cause an extended linear and nonlinear phase of the perturbation field evolution leading to a reduced rate of spectral growth and delay in the breakdown toward turbulence.

6.1 Role of pressure-dilatation

The three studies performed as part of this thesis clearly establish pressure-dilatation as an important mechanism in enforcing compressibility effects on different flow processes. Therefore, in this section, we provide a brief discussion on the important phenomenon that relate specifically to pressure-dilatation and its effect on the overall perturbation development. The effect of the pressure-dilatation mechanism can be summarized into six major inferences which are discussed here in detail. Some key results presented in this thesis are referenced as evidence for each inference. A few new results are also provided to complete the discussion on the role of pressure-dilatation in perturbation development of high speed flows. The six key inferences are:

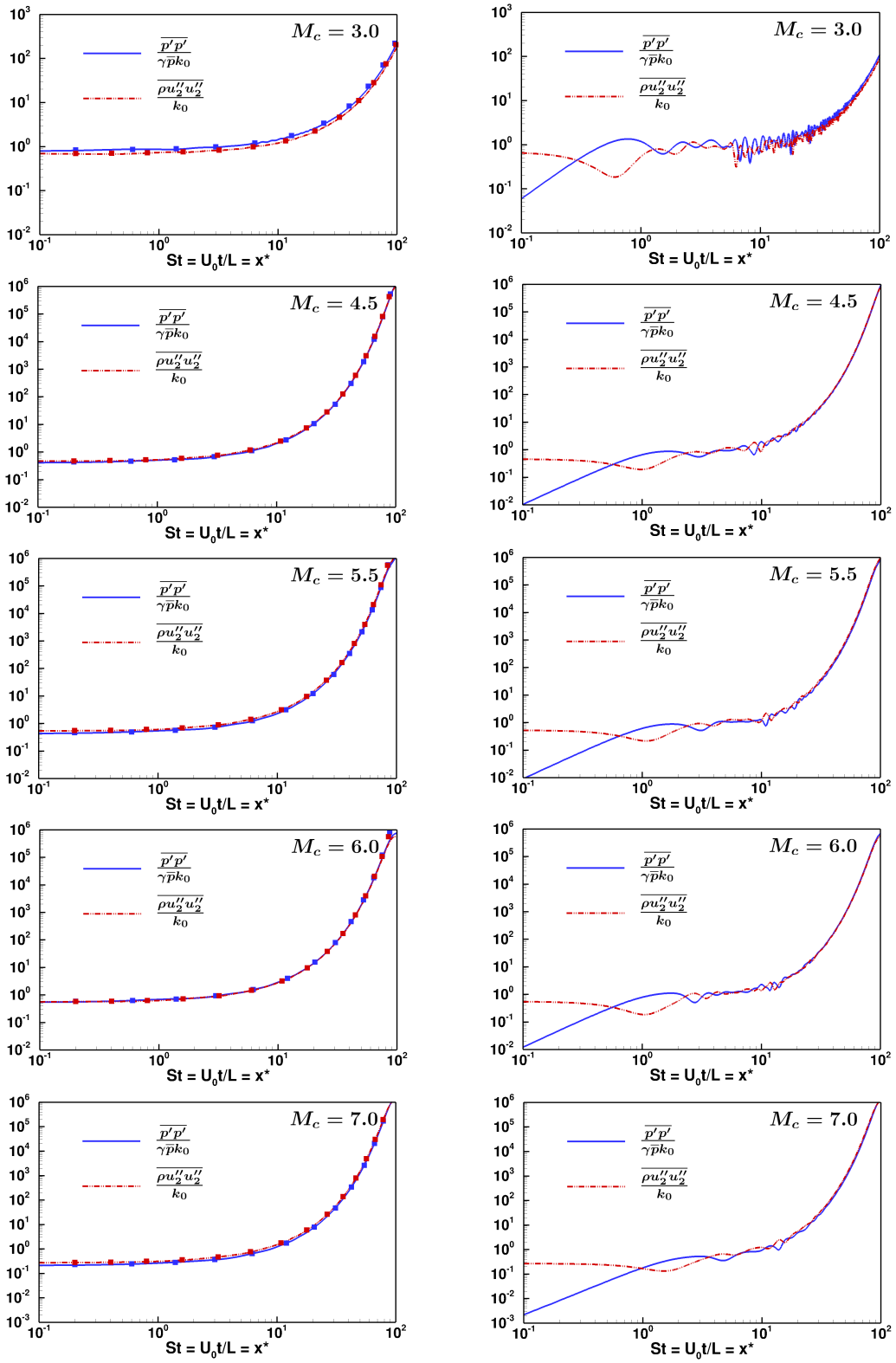

Figure 6.1: Equipartition of energy when (a) full LST mode and, (b) only velocity field of LST mode is initialized in single mode 2D simulations. Symbols represent linear theory results.

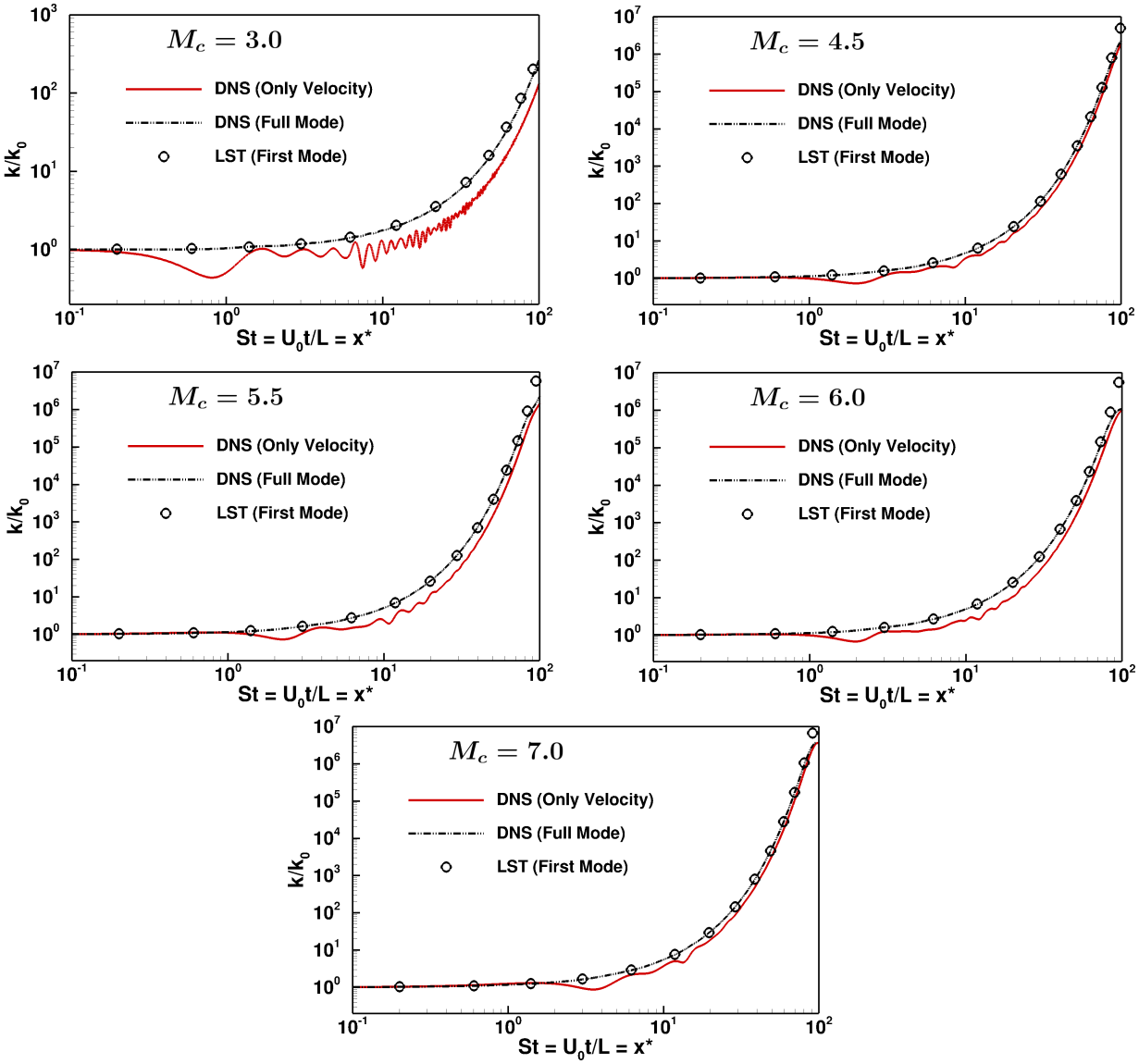

Figure 6.2: Turbulent kinetic energy evolution comparison of full LST mode and only velocity field of LST mode initialization in single mode 2D simulations. Symbols represent linear theory results.

(i) Pressure-dilatation mechanism leads to internal–kinetic energy exchange in compressible flows. A theoretical analysis of the full governing equations presented in Chapter 2 establishes exchange of energy between turbulent internal and kinetic energy via pressure-dilatation mechanism (figure 2.1). This energy exchange is absent for incompressible flows causing the mechanism to play an important role in establishing compressibility effects.

(ii) Energy exchange via pressure-dilatation occurs in all regimes and at every scale. The analysis preformed in Chapter 2 establishes nearly harmonic exchange in Reynolds averaged quantities. However, using DNS, we establish that nearly harmonic exchange occurs at every scale of motion as well (figure 4.13). Since the wall-normal velocity component is most dilatational in nature, established in previous shear flow studies, the scale to scale exchange of energy is presented between pressure-variance and wall-normal component of kinetic energy in figure 4.13.

(iii) The nearly harmonic exchange leads to equipartition of energy between normalized pressure variance and wall normal component of kinetic energy. Equipartition among these energies is established in all high speed cases irrespective of initial condition as evident from figures 4.9(a), 4.10(a) and 4.20 where three different initial profiles are considered namely OS, arbitrary and Mack mode profile respectively. The first two cases exhibit an oscillatory evolution whereas the Mack mode case evolves monotonically. Similar behavior is observed in the overall turbulent kinetic energy evolution as well (figures 4.5(a), 4.8(a) and 4.19).

(iv) Oscillatory evolution occurs if $\overline{p'p'}$ and $\overline{\rho u_2'' u_2''}$ energies are not in equilibrium initially. For the OS and arbitrary profiles oscillatory evolution is observed until these energies equilibrate as observed in figures 4.9(a) and 4.10(a). On the other hand, Mack mode profile is a solution to the linearized compressible equations causing these energies to be in equilibrium initially. Monotonic but equipartitioned behaviour is therefore, observed for this case as evident in figure 4.20. To further investigate this observation we consider two sets of single mode 2D simulations for various Mach numbers given as:

- First set of simulations considered are the single mode simulations presented in Chapter 3 where each case is initialized with low intensity of the full corresponding most unstable mode as computed using LST.
- Second set is similar to the first set, however, only the velocity perturbations are initialized with the corresponding most unstable mode as computed using LST. The pressure fluctuations are ignored for this set of simulations.

The evolution of $\overline{p'p'}$ and $\overline{\rho u_2'' u_2''}$ is now compared for the two sets in figure 6.1 along with the linear stability results shown using symbols. For all the Mach numbers considered, the first set exhibits monotonic exponential growth whereas the second set shows oscillatory growth until the energies equilibrate. As a result evolution of turbulent kinetic energy is also oscillatory causing delayed growth as shown in figure 6.2.

(v) Pressure-dilatation competes with turbulent kinetic energy production to affect key nonlinear process of spectral energy transfer. As a result, the pressure-dilatation to production ratio is identified as an important parameter for characterization of compressibility effects (details in Chapter 4). In figure 4.14, the $|\overline{p'd''}/P_k|$ ratio is compared for OS and arbitrary profile initialization at various wall-normal locations. The OS profile exhibits high levels of pressure-dilatation to production ratio establishing dominant compressibility suppression while negligible compressibility effects can be expected for the arbitrary profile.

(vi) Finally, the spectral energy transfer maybe inefficient due to compressibility. In cases with high $|\overline{p'd''}/P_k|$ ratio such as the OS profile, efficiency of spectral transfer of energy is greatly reduced relative to an equivalent low Mach number simulation (figure 4.15). On the other hand, cases with negligible $|\overline{p'd''}/P_k|$ ratio such as the arbitrary profile exhibit only marginal difference in the spectral spread of perturbations (figure 4.16).

The above inferences clearly establish the role and effect of pressure-dilatation on perturbation evolution in compressible flows. These insights into the pressure-dilatation mechanism will particularly prove useful for development of efficient predictive models for compressible flows.

REFERENCES

J. D. Anderson Jr. *Hypersonic and high-temperature gas dynamics*. American Institute of Aeronautics and Astronautics, 2006.

Y. Andreopoulos, J. H. Agui, and G. Briassulis. Shock wave-turbulence interactions. *Annual Review of Fluid Mechanics*, 32(1):309–345, 2000.

S. A. Berry and T. J. Horvath. Discrete-roughness transition for hypersonic flight vehicles. *Journal of Spacecraft and Rockets*, 45(2):216–227, 2008.

J. J. Bertin and R. M. Cummings. Fifty years of hypersonics: Where we've been, where we're going. *Progress in Aerospace Sciences*, 39(6):511–536, 2003. ISSN 0376–0421.

F. P. Bertolotti and Th. Herbert. Analysis of the linear stability of compressible boundary layers using the PSE. *Theoretical and Comp. Fluid Dynamics*, 3(2):117–124, 1991.

R. L. Bertsch, S. Suman, and S. S. Girimaji. Rapid distortion analysis of high Mach number homogeneous shear flows: Characterization of flow-thermodynamics interaction regimes. *Physics of Fluids*, 24(12):125106, 2012.

W. Blumen. Shear layer instability of an inviscid compressible fluid. *Journal of Fluid Mechanics*, 40(4):769–781, 1970.

D. Bountin, A. Maslov, and Y. Gromyko. Analysis of disturbances in a hypersonic boundary layer on a cone with heating/cooling of the nose tip. *Physics of Fluids*, 30(5):054103, 2018.

K. M. Butler and B. F. Farrell. Three-dimensional optimal perturbations in viscous shear flow. *Physics of Fluids A: Fluid Dynamics*, 4(8):1637–1650, 1992.

P. Chassaing, R. A. Antonia, F. Anselmet, L. Joly, and S. Sarkar. *Variable density fluid turbulence*. Fluid Mechanics and Its Applications. Springer, Dordrecht, 2002.

H. K. Cheng. Perspectives on hypersonic viscous flow research. *Annual Review of Fluid Mechanics*, 25(1):455–484, 1993.

B. C. Chynoweth, S. P. Schneider, C. Hader, H. Fasel, A. Batista, J. Kuehl, T. J. Juliano, and B. M. Wheaton. History and progress of boundary-layer transition on a Mach-6 flared cone. *Journal*

of Spacecraft and Rockets, 56(2):333–346, 2019.

N. T. Clemens and V. Narayanaswamy. Low-frequency unsteadiness of shock wave/turbulent boundary layer interactions. *Annual Review of Fluid Mechanics*, 46:469–492, 2014.

A. W. Cook and Y. Zhou. Energy transfer in Rayleigh-Taylor instability. *Physical Review E*, 66: 026312, Aug 2002.

T. Ellingsen and E. Palm. Stability of linear flow. *Physics of Fluids*, 18(4):487–488, 1975.

A. Favre. Turbulence: Space-time statistical properties and behavior in supersonic flows. *Physics of Fluids*, 26(10):2851–2863, 1983.

A. Fedorov. Transition and stability of high-speed boundary layers. *Annual Review of Fluid Mechanics*, 43(1):79–95, 2011.

K. J. Franko and S. K. Lele. Breakdown mechanisms and heat transfer overshoot in hypersonic zero pressure gradient boundary layers. *Journal of Fluid Mechanics*, 730:491–532, 2013.

T. B. Gatski and J. Bonnet. *Compressibility, turbulence and high speed flow*. Academic Press, 2013.

S. Ghosh, H. Foysi, and R. Friedrich. Compressible turbulent channel and pipe flow: Similarities and differences. *Journal of Fluid Mechanics*, 648:155–181, 2010.

C. A. Gomez and S. S. Girimaji. Toward second-moment closure modelling of compressible shear flows. *Journal of Fluid Mechanics*, 733:325–369, 2013.

C. A. Gomez and S. S. Girimaji. Explicit algebraic Reynolds stress model (EARSM) for compressible shear flows. *Theoretical and Computational Fluid Dynamics*, 28(2):171–196, Apr 2014. ISSN 1432-2250.

P. Grete, B. W. O'Shea, K. Beckwith, W. Schmidt, and A. Christlieb. Energy transfer in compressible magnetohydrodynamic turbulence. *Physics of Plasmas*, 24(9):092311, 2017.

C. Hader and H. F. Fasel. Towards simulating natural transition in hypersonic boundary layers via random inflow disturbances. *Journal of Fluid Mechanics*, 847:R3, 2018.

C. Hader and H. F. Fasel. Direct numerical simulations of hypersonic boundary-layer transition for a flared cone: Fundamental breakdown. *Journal of Fluid Mechanics*, 869:341384, 2019.

F. Hamba. Effects of pressure fluctuations on turbulence growth in compressible homogeneous shear flow. *Physics of Fluids*, 11(6):1623–1635, 1999.

J. W. Haney Jr. Orbiter entry heating lessons learned from development flight test program. 1983.

A. Hanifi and D. S. Henningson. The compressible inviscid algebraic instability for streamwise independent disturbances. *Physics of Fluids*, 10(8):1784–1786, 1998.

W. H. Heiser and D. T. Pratt. *Hypersonic airbreathing propulsion*. AIAA, 1994.

Th. Herbert. Parabolized stability equations. *Annual Review of Fluid Mechanics*, 29(1):245–283, 1997.

L. Hillberg. Influence of material properties on re-entry vehicle heat shield design. In *8th Structural Dynamics and Materials Conference*, 1967.

P. G. Huang, G. N. Coleman, and P. Bradshaw. Compressible turbulent channel flows: DNS results and modelling. *Journal of Fluid Mechanics*, 305:185–218, 1995.

T. L. Jackson and C. E. Grosch. Inviscid spatial stability of a compressible mixing layer. *Journal of Fluid Mechanics*, 208:609–637, 1989.

R. Jahanbakhshi and T. A. Zaki. Nonlinearly most dangerous disturbance for high-speed boundary-layer transition. *Journal of Fluid Mechanics*, 876:87–121, 2019.

M. Karimi and S. S. Girimaji. Suppression mechanism of Kelvin-Helmholtz instability in compressible fluid flows. *Physical Review E*, 93:041102, Apr 2016.

M. Karimi and S. S. Girimaji. Influence of orientation on the evolution of small perturbations in compressible shear layers with inflection points. *Physical Review E*, 95:033112, Mar 2017.

S. C. Kassinos, W. C. Reynolds, and M. M. Rogers. One-point turbulence structure tensors. *Journal of Fluid Mechanics*, 428:213–248, 2001.

S. Kida and S. A. Orszag. Energy and spectral dynamics in decaying compressible turbulence. *Journal of Scientific Computing*, 7(1):1–34, March 1992. ISSN 1573-7691.

A. N. Kolmogorov. The local structure of turbulence in incompressible viscous fluid for very large Reynolds numbers. In *Doklady Akademii Nauk SSSR*, volume 30, pages 299–303, 1941.

R. H. Kraichnan. Decay of isotropic turbulence in the direct-interaction approximation. *Physics of*

Fluids, 7(7):1030–1048, 1964.

G. Kumar, S. S. Girimaji, and J. Kerimo. WENO-enhanced gas-kinetic scheme for direct simulations of compressible transition and turbulence. *Journal of Computational Physics*, 234: 499–523, 2013. ISSN 0021-9991.

G. Kumar, R. L. Bertsch, and S. S. Girimaji. Stabilizing action of pressure in homogeneous compressible shear flows: Effect of Mach number and perturbation obliqueness. *Journal of Fluid Mechanics*, 760:540–566, 2014.

M. T. Landahl. A note on an algebraic instability of inviscid parallel shear flows. *Journal of Fluid Mechanics*, 98(2):243–251, 1980.

J. Larsson, I. Bermejo-Moreno, and S. K. Lele. Reynolds- and Mach-number effects in canonical shock-turbulence interaction. *Journal of Fluid Mechanics*, 717:293–321, 2013.

K. Lee, V. Venugopal, and S. S. Girimaji. Pressure-strain energy redistribution in compressible turbulence: Return-to-isotropy versus kinetic-potential energy equipartition. *Physica Scripta*, 91(8):084006, 2016.

S. K. Lele. Compressibility effects on turbulence. *Annual Review of Fluid Mechanics*, 26(1): 211–254, 1994.

M. Lessen, J. A. Fox, and H. M. Zien. On the inviscid stability of the laminar mixing of two parallel streams of a compressible fluid. *Journal of Fluid Mechanics*, 23(2):355–367, 1965.

Q. Li, S. Fu, and K. Xu. Application of gas-kinetic scheme with kinetic boundary conditions in hypersonic flow. *AIAA Journal*, 43(10):2170–2176, 2005.

W. Liao, Y. Peng, and L.-S. Luo. Gas-kinetic schemes for direct numerical simulations of compressible homogeneous turbulence. *Physical Review E*, 80(4):046702, 2009.

D. Livescu and C. K. Madnia. Small scale structure of homogeneous turbulent shear flow. *Physics of Fluids*, 16(8):2864–2876, 2004.

L. M. Mack. Linear stability theory and the problem of supersonic boundary-layer transition. *AIAA Journal*, 13(3):278–289, 1975.

L. M. Mack. Boundary-layer linear stability theory. *AGARD Rep.*, 709, 1984.

M. R. Malik. Prediction and control of transition in supersonic and hypersonic boundary layers. *AIAA Journal*, 27(11):1487–1493, 1989.

M. R. Malik. Numerical methods for hypersonic boundary layer stability. *Journal of Computational Physics*, 86(2):376 – 413, 1990. ISSN 0021-9991.

G. May, B. Srinivasan, and A. Jameson. An improved gas-kinetic BGK finite-volume method for three-dimensional transonic flow. *Journal of Computational Physics*, 220(2):856–878, 2007.

J. A Meersman, C. Hader, and H. F Fasel. Hypersonic boundary-layer transition: Comparison of the fundamental resonance breakdown for a flared and straight cone at Mach 6. In *2018 Fluid Dynamics Conference*, page 3851, 2018.

F. Miró Miró and F. Pinna. Effect of uneven wall blowing on hypersonic boundary-layer stability and transition. *Physics of Fluids*, 30(8):084106, 2018.

A. Mittal and S. S. Girimaji. Mathematical framework for analysis of internal energy dynamics and spectral distribution in compressible turbulent flows. *Physical Review Fluids*, 4:042601, Apr 2019.

A. Mittal and S. S. Girimaji. Nonlinear evolution of perturbations in high Mach number wall-bounded flow: Pressure–dilatation effects. *Physics of Fluids*, 32(3):036101, 2020.

H. Miura and S. Kida. Acoustic energy exchange in compressible turbulence. *Physics of Fluids*, 7 (7):1732–1742, 1995.

S. B. Pope. *Turbulent flows*. Cambridge University Press, 2000.

D. Praturi and S. S. Girimaji. Effect of pressure-dilatation on energy spectrum evolution in compressible turbulence. *Physics of Fluids*, 31(5):055114, 2019.

A. Ramachandran, B. Saikia, K. Sinha, and R. Govindarajan. Effect of prandtl number on the linear stability of compressible couette flow. *International Journal of Heat and Fluid Flow*, 61: 553 – 561, 2016. ISSN 0142-727X.

H. Reed, R. Kimmel, S. Schneider, and D. Arnal. Drag prediction and transition in hypersonic flow. In *28th Fluid Dynamics Conference*, 1997.

H. L. Reed, W. S. Saric, and D. Arnal. Linear stability theory applied to boundary layers. *Annual*

Review of Fluid Mechanics, 28:389–428, 1996.

D. Rempfer. Low-dimensional modeling and numerical simulation of transition in simple shear flows. *Annual Review of Fluid Mechanics*, 35(1):229–265, 2003.

S. Sarkar. The stabilizing effect of compressibility in turbulent shear flow. *Journal of Fluid Mechanics*, 282:163–186, 1995.

S. Sarkar, G. Erlebacher, M. Y. Hussaini, and H. O. Kreiss. The analysis and modelling of dilatational terms in compressible turbulence. *Journal of Fluid Mechanics*, 227:473–493, 1991.

S. P. Schneider. Flight data for boundary-layer transition at hypersonic and supersonic speeds. *Journal of Spacecraft and Rockets*, 36(1):8–20, 1999.

M. T. Semper and R. DW Bowersox. Tripping of a hypersonic low-Reynolds-number boundary layer. *AIAA Journal*, 55(3):808–817, 2017.

A. Simone, G. N. Coleman, and C. Cambon. The effect of compressibility on turbulent shear flow: A rapid-distortion-theory and direct-numerical-simulation study. *Journal of Fluid Mechanics*, 330:307–338, 1997.

J. Sivasubramanian and H. F. Fasel. Numerical investigation of the development of three-dimensional wavepackets in a sharp cone boundary layer at Mach 6. *Journal of Fluid Mechanics*, 756:600–649, 2014.

J. Sivasubramanian and H. F. Fasel. Direct numerical simulation of transition in a sharp cone boundary layer at Mach 6: Fundamental breakdown. *Journal of Fluid Mechanics*, 768:175–218, 2015.

K. F. Stetson. Comments on hypersonic boundary-layer transition. Technical report, Wright Research and Development Center Wright-Patterson AFB OH, 1990.

V. Venugopal, D. Praturi, and S. S. Girimaji. Non-equilibrium thermal transport and entropy analyses in rarefied cavity flows. *Journal of Fluid Mechanics*, 864:995–1025, 2019.

A. W. Vreman, N. D. Sandham, and K. H. Luo. Compressible mixing layer growth rate and turbulence characteristics. *Journal of Fluid Mechanics*, 320:235–258, 1996.

J. Wang, Y. Yang, Y. Shi, Z. Xiao, X. T. He, and S. Chen. Cascade of kinetic energy in three-

dimensional compressible turbulence. *Physical Review Letters*, 110:214505, May 2013.

Z. Xie and S. S. Girimaji. Instability of Poiseuille flow at extreme Mach numbers: Linear analysis and simulations. *Physical Review E*, 89:043001, Apr 2014.

Z. Xie, M. Karimi, and S. S. Girimaji. Small perturbation evolution in compressible Poiseuille flow: Pressure-velocity interactions and obliqueness effects. *Journal of Fluid Mechanics*, 814: 249–276, 2017.

K. Xu. A gas-kinetic BGK scheme for the navier-stokes equations and its connection with artificial dissipation and Godunov method. *Journal of Computational Physics*, 171(1):289–335, 2001. ISSN 0021-9991.

K. Xu and Meiliang Mao. Gas-kinetic BGK scheme for hypersonic viscous flow. In Clinton Groth and David W. Zingg, editors, *Computational Fluid Dynamics 2004*, pages 183–188, Berlin, Heidelberg, 2006. Springer Berlin Heidelberg. ISBN 978-3-540-31801-9.

P. K. Yeung, J. G. Brasseur, and Q. Wang. Dynamics of direct large-small scale couplings in coherently forced turbulence: Concurrent physical- and Fourier-space views. *Journal of Fluid Mechanics*, 283:43–95, 1995.

C. Zhang, Y. Zhu, X. Chen, H. Yuan, J. Wu, S. Chen, C. Lee, and M. Gad-el Hak. Transition in hypersonic boundary layers. *AIP Advances*, 5(10):107137, 2015.

W. Zhu, M. Shi, Y. Zhu, and C. Lee. Experimental study of hypersonic boundary layer transition on a permeable wall of a flared cone. *Physics of Fluids*, 32(1):011701, 2020.

Y. Zhu, X. Chen, J. Wu, S. Chen, C. Lee, and M. Gad-el Hak. Aerodynamic heating in transitional hypersonic boundary layers: Role of second-mode instability. *Physics of Fluids*, 30(1):011701, 2018.